Improving characterization of fractured rock using 3D cross-borehole electrical resistivity tomography (ERT)

By

Judith L. Robinson

A Dissertation submitted to the

Graduate-School Newark

Rutgers, The State University of New Jersey

in partial fulfillment of the requirements

for the degree of

Doctor of Philosophy

Graduate Program in

Environmental Sciences

written under the direction of

Professor Lee D. Slater

and approved by

_____

Dr. Lee D. Slater

_____

Dr. Timothy Johnson

_____

Dr. Dimitrios Ntarlagiannis

_____

Dr. Kristina Keating

Newark, New Jersey

May 2015

Copyright page:

ABSTRACT OF THE DISSERTATION

Improving characterization of fractured rock using 3D cross-borehole electrical resistivity tomography (ERT)

By Judith L. Robinson
Dissertation Director: Professor Lee D. Slater

There is a growing need to understand the hydraulic properties of fractured rock for the development and extraction of natural resources and also to engineer remediation strategies at contaminated sites. The characterization of fractured rock is inherently complex due to the multifaceted interrelationships between stress, temperature, roughness and fracture geometry that affect hydraulic conductivity and flow paths that have hydraulic properties varying over orders of magnitude. Often, sparse data points are interpolated from borehole locations to infer the spatial distribution of flow and transport within fractures. However, these fracture distributions are often poorly resolved due to the heterogeneity of these networks between the borehole locations. Electrical resistivity tomography (ERT) is a viable technology to characterize fractured rock as the electrical pathways mimic hydraulic pathways in fractured rock, assuming surface conduction is small. Previous work using ERT in fractured rock gave limited hydrogeological information due to finite element modeling techniques which were not physically appropriate for fractured rock and lack of instrumentation to permit imaging of isolated fracture zones. Synthetic and field datasets were used to incorporate field information to yield an improved hydrogeological interpretation. Specifically, model constraints were incorporated in the inversion modeling and borehole deviations defining these boundaries were

explicitly defined in the discretization. Where this information was incorporated, ERT time-lapse changes in conductivity were more focused surrounding fracture locations and borehole effects were minimized. A rigorous examination of localized effects of de-regularization was undertaken and it was found that uncertainty in these boundaries can lead to spurious inversion artifacts. Electrode arrays within seven boreholes were designed, which included isolation bladders and a water sample/injection line. This design facilitated multiple tracer tests in a fractured mudstone to be conducted. The spatial scale of this experiment was such that the primary hydrogeological heterogeneity controlling flow and transport was captured, providing unique information relative to that acquired from borehole logging methods alone. The modeling techniques and instrumentation advancements detailed in this dissertation demonstrates the potential of ERT at fractured rock sites to work towards creating comprehensive flow and transport models.

Acknowledgements

First and foremost, I would like to thank Lee Slater, whom I cannot thank enough for always being gracious, challenging me with interesting opportunities and taking the time to provide an insightful review of my work. I have learned how to be a better researcher and writer through his example and I am grateful for his time and effort in my research. I would like to thank Dimitris Ntlargiannis for often coming to my rescue in the lab and field and being the ultimate optimistic regardless of the situation. My understanding of resistivity inversion analysis was brought to a new level thanks to Timothy Johnson, who answered countless emails and phone questions and was extremely supportive in my research efforts. I would also like to thank Kristina Keating who was willing to answer any question, help out or be supportive in any way I needed. I owe my thanks to Alexander Gates, for offering initial opportunities and support that enabled me to remain within graduate school.

My appreciation and utmost thanks goes to Liz Morrin, who competently took care of all my orders, reimbursements and class registrations and provided me with sound advice and a listening ear when I needed it most.

This doctoral degree is presented to me, but would not have been possible without the help and support of so many of the graduate students in the Department of Earth and Environmental Sciences and USGS staff members. In particular, David Grunat, Sundeep Sharma, Jay Nolan and Jeffrey Heenan were extremely helpful and innovative to my benefit in either in the lab or field. Thomas Imbrigiotta, Pierre Lacombe and Alex Fiore were always willing to lend me a hand in the field, staying until after hours or weekends if necessary. I have

come to appreciate and respect so many of my peers (Chi Zhang, Kisa Mwakanyamale, Andy Parsekian, Gordon Ostermann, Neil Terry, Xi Chen, Jung Yun, Ashley Samuel, Sam Falzone, Sam Wallace, Mike Kalczynski, Joshua Lefkowitz) during my time here.

I would like to thank my parents, Sheldon and Susan Robinson, who passed on to me all the qualities I needed to earn this degree. I learned through their life stories and I hope I have made them proud. I am forever grateful to my sister, Karen von Stappenbeck, who helped put me back on track during my degree when I veered off it, and who candidly accepts and deals with any situation. I would like to thank an amazing friend, Yolanda Adragna, who was there for me with perspective, caring and understanding.

I dedicate this degree to my children, Jesica and Marco Porcelli. I hope as they grow, they look upon my accomplishment with pride and know I was thinking of them with love every day, in every place.

Table of Contents

List of Illustrations

Chapter 1

Chapter 2

Chapter 3

Chapter 4

Chapter 5

List of Tables

Chapter 3

Chapter 4

Chapter 5

CHAPTER 1: INTRODUCTION

1.1 Fractured rock hydrogeology

Fractured rock environments are abundant worldwide and characterization is imperative when considering: aquifer and petroleum reservoir development; contaminant storage, migration, delineation and remediation; and in developing structurally-sound infrastructure. Flow and transport is poorly understood due to the complex interrelationships between stress, temperature, roughness and fracture geometry affecting hydraulic conductivities (Singhal & Gupta, 1999). Dominant flow pathways in fractured rock are controlled by joints, fractures, shear zones, faults and other discontinuities; fracture zones of highly crushed units can also dominate flow pathways (Figure 1.1). Characterization of these pathways, which have hydraulic conductivities that can vary by orders of magnitude from the matrix porosity, is critical to extract resources and remediate these sites.

Figure 1.1: Shale mudstone fractured rock where fracture zones are darker units consisting of highly crushed 'coal' units within the sequence. (Photo credit: Pierre Lacombe, USGS)

Fractured rock environments are typically characterized through information acquired in boreholes. Hydrogeologists typically use single and cross-borehole hydraulic testing, and pumping and tracer injection testing to estimate hydraulic conductivities and determine flow mechanisms (Singhal & Gupta, 1999). Sealing off borehole intervals using packers during hydraulic testing allows transmissivities to be calculated within these isolated intervals (Neuman, 2005). The interpretations of hydrogeological tests are non-unique (i.e. more than one type of model can be fit to field measurements) such that hydrogeophysical methods can provide information to constrain interpretations.

1.2 Fractured rock hydrogeophysics

Geophysical methods are acknowledged to yield valuable spatially extensive information in hydrogeological studies (Berkowitz, 2002; Neuman, 2005) (Figure 1.2). Borehole geophysical profiling has become commonplace in industry with research support from government agencies (e.g. http://water.usgs.gov/ogw/bgas/methods.html). The data collected from each log is commonly dependent on different physical properties, thus correlation between logs can aid in identifying fracture locations and flow characteristics. The highly spatially-accurate information from borehole logs has, for example, been used to vertically delineate landfill leachate plumes in a glacial aquifer (Mack, 1993). Advances in temperature profiling with improved sensors and the ability to seal cross connections has allowed improved delineation of flow directions and fracture transmissivities (Pehme et al., 2013).

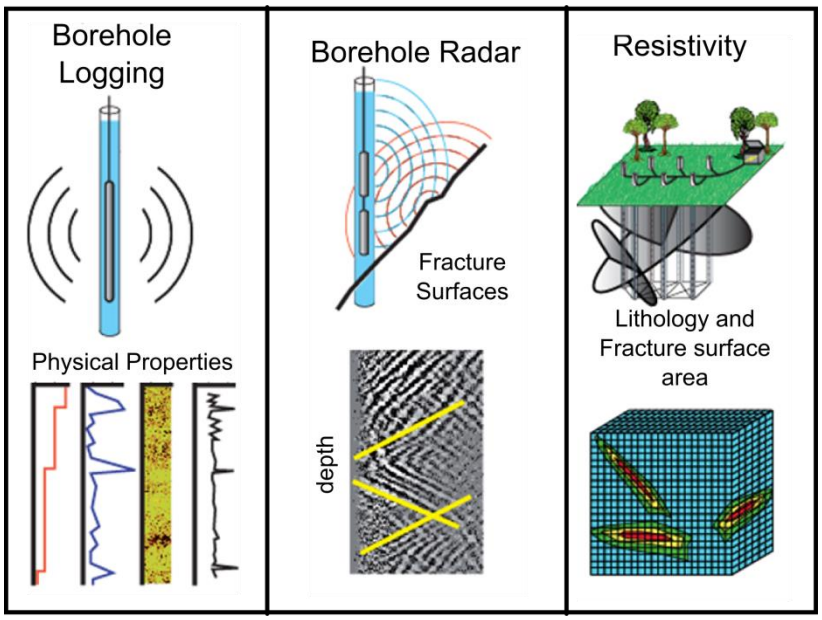

Figure 1.2: A sample of geophysical technologies available to characterize fractured rock (Image credit: Fred Day-Lewis, USGS)

Ground penetrating radar (GPR) is another geophysical technology that has been used in surface and borehole studies within fractured rock during tracer studies. Day-Lewis et al., (2003) used 2D cross-borehole GPR to identify transmissive fractures to infer tracer arrival times. Electrical conductivity logs combined with single-hole GPR datasets were used to identify transmissive fractures and estimate the velocity and mass of tracer within each flow pathway (Dorn et al., 2012). Surface GPR signals were calibrated to tracer concentrations and used to estimate dispersivity and effective fracture aperture (Becker & Tsoflias, 2010). These studies provide promising results in identifying flow and transport properties in fractured rock; however, GPR is limited to resistive environments where attenuation of electromagnetic (EM) waves is low.

There is a need for additional methods to interpret processes occurring away from the vicinity of boreholes. The near-surface geophysical method, electrical resistivity tomography (ERT) can provide information in between discrete borehole locations and

can provide an additional constraint on the overall interpretation of fractures in fractured rock environments. ERT is potentially well-suited for imaging fracture zones since electrical current flow in fractured rock is primarily electrolytic via the secondary porosity associated with the fractures, i.e. the electrical current flow paths are (to first order) the same as the fluid flow paths (assuming surface conduction is small). ERT surveys can be inexpensive to conduct; surface surveys are non-invasive while borehole surveys can use existing wells. Furthermore, data collection can often be automated, permitting large spatial and temporal datasets to be acquired.

In hydrogeological and geophysical studies, we do not have the ability to measure fractures directly and each measurement has intrinsic uncertainty. The interpretation of measurements often becomes model dependent (Berkowitz , 2002) and consistency across models can validate and strengthen our interpretations. ERT can potentially provide key supporting information in between wells for a more spatially extensive hydrogeological interpretation.

1.3 Objectives and Thesis Organization

This thesis explores imaging fractured rock aquifers and monitoring tracers/remedial amendments to improve understanding of flow and transport. In doing so, novel advancements in ERT data processing and modeling were explored. Through the research presented in the three main chapters of this thesis, I will demonstrate:

1. Inverse modeling of synthetic 3D ERT datasets can successfully extract information to characterize fracture zones (Chapter 3).

2. Inverse modeling of pseudo-3D field datasets can successfully extract information to characterize fracture locations and infer transient subsurface processes occurring (Chapter 4).
3. Migration of an injected tracer can be successfully imaged using 3D cross borehole ERT (Chapter 5).

The research presented here is the first critical step towards developing ERT as a viable tool for the static and transient characterization of fractured rock environments. The advancements presented in this dissertation pave the way for more effective ERT data processing, and will ultimately allow ERT data to be combined with hydrogeologic data to create comprehensive flow and transport models.

CHAPTER 2: METHODS

2.1 Basic principles of electrical resistivity tomography (ERT)

Electrical resistance (R) is defined as the opposition of material to the flow of an electric current and is specific to a measurement configuration. Measurements of R are calculated from potential measurements ΔV of a known current injection I (i.e. $R = \Delta V / I$) into the subsurface. The general approach involves injecting a current between two electrodes followed by measuring the transfer resistance between two other electrodes. Current injection electrodes in four-point measurements are commonly referred to with the acronyms A and B; potential electrodes in four-point measurements are commonly referred to as M and N (Figure 2.1).

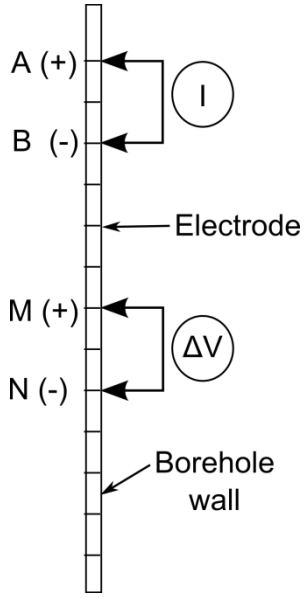

Figure 2.1: Schematic of four electrode measurement where current electrodes are designated as A and B and potential electrodes are designated as M and N.

Electrical resistivity (ρ) is an intrinsic physical property of the subsurface and is a measure of a material's ability to conduct an electric current. The potential **V** at any point for current strength I injected at a source **r** for a given ρ is described by the Poisson equation:

$$\nabla \cdot \left(\frac{1}{\rho} \nabla \mathbf{V}\right) = -I\delta(\mathbf{r}) \quad (2.1)$$

where δ signifies the Dirac delta function. Equation 2.1 is subject to either Neumann (i.e. no current flow) or mixed-type source-dependent boundary conditions.

For a single current electrode in a homogeneous half-space, Equation 2.1 simplifies to:

$$V(r) = \frac{\rho I}{2\pi r} \quad (2.2)$$

which defines the potential *V* as a function of a radial distance *r* from the current electrode. The potential difference between electrodes M and N where current injection is at A is then given by:

$$V_M = \frac{\rho I}{2\pi}\left(\frac{1}{\mathrm{AM}} - \frac{1}{\mathrm{AN}}\right) \quad (2.3)$$

where AM and AN are the distances between current electrode A and potential electrode M (+) and N (-) respectively. For a four electrode measurement, using superposition the total potential (V_{MN}) at MN equates to:

$$V_{MN} = \frac{\rho I}{2\pi}\left[\left(\frac{1}{\mathrm{AM}} - \frac{1}{\mathrm{BM}}\right) - \left(\frac{1}{\mathrm{AN}} - \frac{1}{\mathrm{BN}}\right)\right] \quad (2.4)$$

which rearranges to:

$$\rho = 2\pi \frac{V_{MN}}{I} k \quad (2.5)$$

$$k = \left(\frac{1}{\mathrm{AM}} - \frac{1}{\mathrm{BM}}\right) - \left(\frac{1}{\mathrm{AN}} - \frac{1}{\mathrm{BN}}\right) \quad (2.6)$$

For a heterogeneous earth, the electrical resistivity calculated in Equation 2.5 is defined as the apparent resistivity, ρ_{app}, since this assumes a homogenous earth. When considering electrodes below the surface (i.e. in a borehole), a factor of 4π is used instead

of 2π in Equations 2.2 through 2.5 to account for a surface boundary (at z=0). To account for this surface boundary, it is common to use the method of images, and define image lengths A_i and B_i for current electrodes. In Equation 2.6, k is modified as:

$$k = \left(\frac{1}{A_iM} + \frac{1}{AM}\right) - \left(\frac{1}{B_iM} + \frac{1}{BM}\right) - \left(\frac{1}{A_iN} + \frac{1}{AN}\right) + \left(\frac{1}{B_iN} + \frac{1}{BN}\right) \quad (2.7)$$

In a DC (direct current) resistivity survey, the configuration of the electrodes can be optimized to minimize the data acquisition time while maximizing the measurement resolution. For *n* electrodes, a total of $n(n-1)(n-2)(n-3)/8$ four-point electrode configurations exist. Collection of this comprehensive measurement sequence is impractical especially when attempting to capture time-lapse processes. An optimized measurement sequence will depend on site requirements (e.g. measurement errors and resistivity structure) and specific project demands (e.g. resolution and data acquisition speed). Commonly used four-electrode configurations are nested arrays such as Wenner and Schlumberger or dipole-dipole schemes; the advantages and disadvantages of these configurations in resolving horizontal and vertical subsurface features are well documented (for example, Binley & Kemna, 2005). Recognizing a need for optimized measurement sequences, a number of researchers (Blome et al., 2011; Loke et al., 2010; Stummer et al., 2004; Wilkinson et al., 2012; Wilkinson et al., 2006) have explored incrementally adding measurements to an initial dataset that will improve the resolution of the true (in many cases, assumed) model.

Electrical resistivity or its inverse electrical conductivity is sensitive to subsurface variations in moisture content, temperature, lithology, porosity, groundwater composition and clay content (Binley & Kemna, 2005). In this thesis, the investigated fractured rock environments are below the water table and at depths unaffected by diurnal temperature

fluctuations. In this setting, lithological porosity changes due to the presence of fractures and groundwater composition are expected to dominate the electrical measurement response assuming low surface conduction.

2.1.1 Induced Polarization

This thesis considers that electrolytic pathways are expected to dominate the electrical response for a DC resistivity survey. However, this assumes that the rock surface is non-conducting and ignores the electro-migration of charge carriers at the pore-fluid/mineral interface. Surface conduction is sensitive to lithological parameters such as grain size, surface area and dependent on pore fluid conductivity (Revil & Skold, 2011) and saturation in vadose zone studies (Ulrich & Slater, 2004). Where it is expected that surface conduction effects are high, as for the case where high clay content exists, information on surface conduction effects can aid in the interpretation of ERT data. An extension of an ERT survey that measures these effects is an induced polarization (IP) survey. Induced polarization (IP) can constrain the lithological interpretation of ERT data particularly in environments where fine-grained material is present. Much of the work presented here is within a fractured mudstone, which may contain a considerable amount fine-grained material. It is mentioned here for completeness such that the reader may refer back to this section when IP is further discussed in Chapter 6.

2.2 Finite element mesh (FEM) generation

Electrical resistance measurements are commonly modeled through finite element methods, which necessitates the generation of a finite element mesh (FEM). In 2D, rectangular or triangular shaped elements are common in ERT modeling; in 3D, cuboids,

triangular prisms or tetrahedrons are common. This research used tetrahedral mesh elements to allow for flexibility in terms of mesh refinement around small scale features (i.e. fractures, boreholes and electrodes) and incorporation of topography (Rücker et al., 2006) (Figure 2.2). Several robust mesh generators are available; TetGen was used since it is integrated with the ERT modeling software, E4D, (discussed below) which was used in this study.

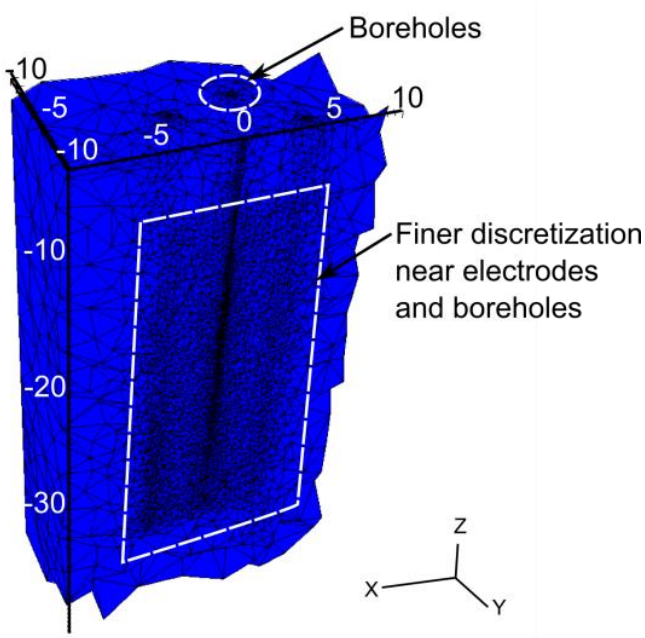

Figure 2.2: Example 3D tetrahedral mesh showing finer discretization near boreholes and electrode locations

2.3 Electrical resistivity tomography modeling

Below is a general overview of the ERT modeling equations and theory as related to this dissertation. The modeling of ERT measurements in this thesis was achieved using a modified version of the open source parallel code, E4D (https://e4d.pnnl.gov/) described in Johnson et al., (2010). E4D is a 3D deterministic modeling and inversion code for ERT data. The code is specifically designed to work on parallel, high-

performance computing systems. Parallelized code allows for computational efficiency such that larger inverse problems with millions of parameters, which are used to define small scale features such as boreholes, can be solved.

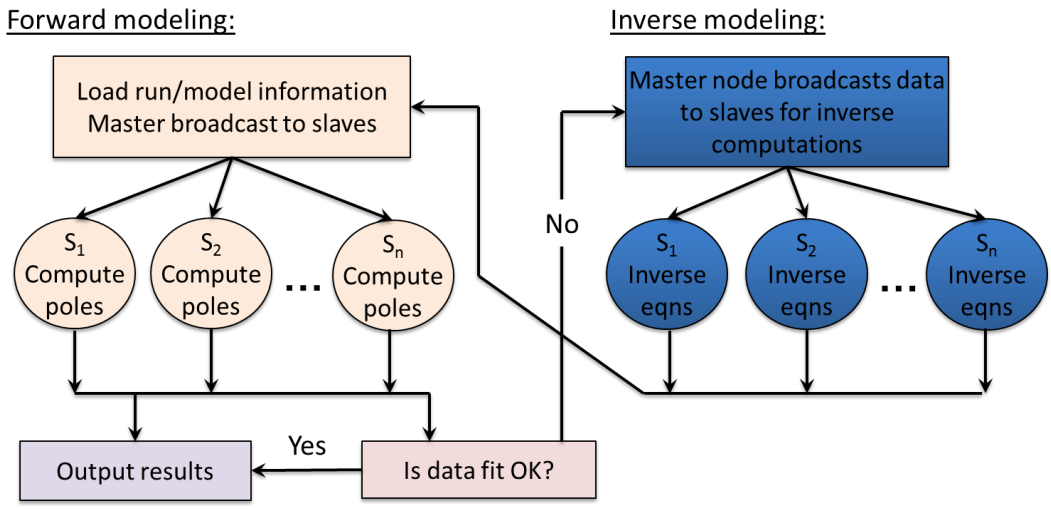

Figure 2.3: ERT modeling code schematic adapted from Johnson et al., 2010.

2.3.1 Forward Modeling

Forward modeling of an ERT conductivity structure yields a potential at each mesh node in the FEM. To speed computational efficiency parallel modeling of pole solutions can be done (Figure 2.3) from which dipole-dipole measurement solutions can be derived. The delta function (which goes to infinity) is used to describe the introduction of current at a point (Equation 2.1). This can introduce a numerical error near the current source due to inaccurate representation in discrete space of a discontinuous (i.e. the delta) function. Numerical errors are also higher near electrode locations due to high potential gradients. Singularity removal can be used to reduce these numerical modeling errors. In this technique, the potential is split into singular and non-singular components. With the analytical solution for the singular component known, the forward finite element problem reduces to finding the non-singular potential (Lowry et

al., 1989; Rücker et al., 2006). Once the non-singular potential is solved, the singular component can be added to obtain the total potential (Blome et al., 2009). Numerical modeling errors associated with large potential gradients can be reduced by using finer elements surrounding electrode locations.

2.3.2 Inverse Modeling

Inversion of ERT data is inherently underdetermined (i.e. non-unique), such that the inverse problem is typically formulated as a regularized optimization problem where model constraints are imposed to limit the number of possible solutions. The objective function shown below seeks to optimize the tradeoff between the data misfit and model constraints (Binley & Kemna, 2005; Sasaki, 1994),

$$\Psi(\mathbf{m}) = \Psi_{\mathrm{d}}(\mathbf{m}) + \alpha\Psi_{\mathrm{m}}, \quad (2.8)$$

where,

$$\Psi_{\mathrm{d}}(\mathbf{m}) = \left\|\mathbf{W_d}\left(\mathbf{d} - \mathrm{f}(\mathbf{m})\right)\right\|, \quad (2.9)$$

$$\Psi_{\mathrm{m}}(\mathbf{m}) = \|\mathbf{W_m}(\mathbf{m} - \mathbf{m_0})\|. \quad (2.10)$$

In equations 2.9 and 2.10, $\|\ \ \|$ signifies the norm of order 2 although other norm measures can be implemented (Farquharson, 2008). The variable Ψ_{d} is a measure of the difference, between the measured ($\mathbf{d}$) and calculated data ($\mathrm{f}(\mathbf{m})$) from the estimated log conductivity distribution ($\mathbf{m}$); Ψ_{m} is a measure of the complexity in $\mathbf{m}$ or a measure of the difference between $\mathbf{m}$ and some preferred reference model, $\mathbf{m_0}$. With an appropriately constructed model weighting matrix ($\mathbf{W_m}$), the reference model $\mathbf{m_0}$ may be non-existent (e.g. ($\mathbf{0}$)), may be a homogeneous medium, or it may contain expected conductivity values used to implement known conductivity constraints. The parameter α optimizes the trade-off between model misfit and data misfit. $\mathbf{W_d}$ is a diagonal data-

weighting matrix, where each data weight is equal to the reciprocal of the individual standard deviations defined by a data error model discussed below. The model-weighting matrix ($\mathbf{W_m}$) contains the model constraints and is also known as the regularization matrix. Minimization of Equations 2.9 and 2.10 assuming data errors are normally distributed leads to a linear system of equations (Binley & Kemna, 2005; Backus & Gilbert, 1968; Farquharson, 2008):

$$(\mathbf{J_k^T W_d^T W_d J_k} + \propto \mathbf{W_m^T R_m W_m})\Delta\mathbf{m_k} = \mathbf{J_k^T W_d^T W_d}[\mathbf{d} - \mathrm{f}(\mathbf{m_k})] - \propto \mathbf{W_m^T R_m W_m}(\mathbf{m_k} - \mathbf{m_0}). \quad (2.11)$$

$\mathbf{R_m}$ always depends on the value of $\mathbf{m}$, requiring an iterative solution (iteratively reweighted least squares or IRLS).

At each iteration *k* the model update vector $\Delta\mathbf{m_k}$ can be solved e.g. by a conjugate gradient least squares algorithm (Johnson et al., 2010; Zhang, 1995). After the first iteration, the reference model, $\mathbf{m_0}$, is assigned the value from model iteration, $\mathbf{m_{k-1}}$, or an already-specified expected conductivity value. $\mathbf{J_k}$ is the Jacobian matrix at iteration *k*, where each member $J_{ij} = \partial \mathrm{f_i}(\mathbf{m_k})/\partial \mathrm{m_j}$ for model $\mathbf{m_k}$. The normalized χ^2 misfit error is used as the convergence criteria which is given by

$$\chi^2 = \frac{1}{n-1}\sum_{\mathrm{i}=1}^{n}\frac{(d_{\mathrm{obs,i}} - \mathrm{f_i}(\mathbf{m}))^2}{SD_{\mathrm{i}}^2}, \quad (2.12)$$

where n is the number of observations and SD_i is the standard deviation for measurement i. When measurement errors are correctly quantified, independent and normally distributed, the data are appropriately fit when χ^2=1, which is the typical value used for the convergence criteria.

Time-lapse ERT datasets can be collected to monitor or delineate conductivity changes due to hydrological processes such as the introduction of a contaminant/tracer, salt-water intrusion, and/or porosity changes. In E4D, model parameters can be regularized to background conductivities or to a previous time-step inverse solution. The minimization of the objective function remains the same as in Equation 2.11 with the normalized χ^2 misfit error (defined in Equation 2.12) used as convergence criteria.

Assessment of measurement errors for $\mathbf{W_d}$ is critical for ensuring high quality ERT images. It has been shown that underestimation of measurement errors can result in overly rough 'noisy' images and overestimation can result in overly smooth images (LaBrecque et al., 1996). Data measurement errors are often assessed with reciprocal measurements (Slater et al., 2000). These measurements are collected by interchanging the current injection electrodes (A and B) with the potential electrodes (M and N). In theory, the resistances should be equal. Measurements with a high reciprocal error can be filtered from the dataset and a functional relationship between measured resistances and data error can be developed and applied to all measurements (Koestel et al., 2008; Slater et al., 2000). In some cases, good data quality results in low reciprocal errors such that forward numerical modeling errors can dominate. This thesis uses two ways to account for overall data errors where reciprocity errors are low: (1) scaling the data errors to maintain relative weighting of measurements (Chapter 4) and (2) estimating the maximum numerical error while accounting for small resistance measurements in the form of an absolute error (Chapter 5).

2.3.3 Regularization and known conductivity constraints

Nearest neighbor smoothing as described in deGroot-Hedlin & Constable (1990) is typically used in $\mathbf{W_m}$ in the absence of a priori information as it conservatively solves for a resistivity distribution with the least amount of structure. In porous media where sharp geological conductivity contrasts are less pronounced than in fractured rock, this approach sets a lower bounds on the amount of electrical conductivity structure within true Earth. To implement smoothness constraints, a similarity constraint equation is included between adjacent elements in the formulation of $\mathbf{W_m}$ (Figure 2.4), as shown between elements 1 and 2; and relative weighting between elements can be adjusted as shown between elements 1 and 7 (Figure 2.4).

Where available field information is provided from borehole testing, additional regularization (i.e. model) constraints can be added to limit the number of non-unique solutions resulting in a more realistic inverse model. Smoothness constraints between different regions in the discretization can be relaxed or 'disconnected' (Figure 2.4) by removing a constraint equation between elements in the formulation of $\mathbf{W_m}$. For example, in Figure 2.4, a constraint equation is omitted between elements 2 and 3. Such a regularization disconnect (RD) enables the inversion to place a sharp conductivity contrast across a boundary, if supported by the data, without penalty. If the conductivity is known within particular elements in the model space (e.g. from a borehole conductivity probe), the conductivity within these elements can be constrained to this value, and relative weighting can also be adjusted, as shown in the last three constraint equations (Figure 2.4).

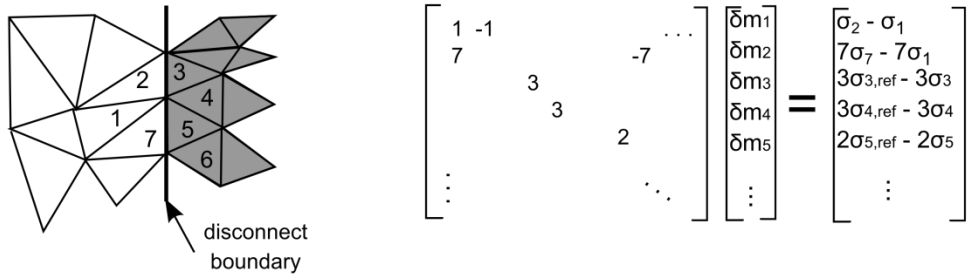

Figure 2.4: Regularization matrix formulation for FEM elements showing different constraint functions.

The functional form of $\mathbf{R_m}$ (Equation 2.11) is a physical representation of constraints to be considered in the model structure. Where no structure is to be applied $\mathbf{R_m}$ is set equal to the identity matrix. Originally described as compactness constraints (Farquharson, 2008; Last & Kubik, 1983), E4D designates functional forms as *reweighting functions*. Reweighting functions are evaluated for a defined *structural metric code*, which defines a relationship between a target element in the FEM and an adjacent element or a reference value. This representation of model constraints allows for ultimate flexibility when inputting available field data and parameters. Model constraints allow a user to add reliable information to the inverse problem, of which the solution is non-unique. This limits the possible number of solutions; however any model constraint must be supported by the data. An inversion model will only converge if the desired data misfit criteria are met In fractured rock, the inverted cumulative distribution function (CDF) can be used to favor a blocky structure (Figure 2.5A) or encourage lower and/or upper bound conductivity limits (Figures 2.5B and C). . For complete information a user manual for E4D is available for download at https://e4d.pnnl.gov/ (T. Johnson, 2014).

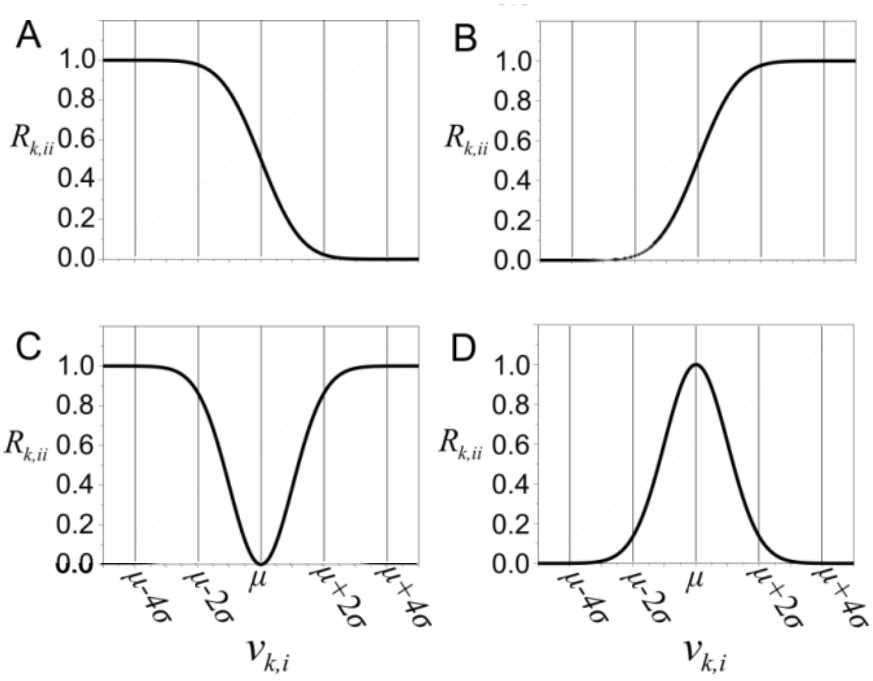

Figure 2.5: Reweighting functions in E4D (https://e4d.pnnl.gov/) A) The weighting of $v_{k,i}$ begins to minimize if the value of $v_{k,i}$ drops below $\mu+2\sigma$, reaching the full weight if $v_{k,i}$ drops below $\mu-2\sigma$. B) The weighting of $v_{k,i}$ begins to minimize if the value of $v_{k,i}$ rises above $\mu-2\sigma$, reaching the full weight if $v_{k,i}$ rises above $\mu+2\sigma$. C) The weighting of $v_{k,i}$ begins to minimize if the value of $v_{k,i}$ deviates from μ, reaching the full weight if $v_{k,i}$ deviates from μ more than (approximately) 2σ. D) The weighting of $v_{k,i}$ begins to minimize as the value of $v_{k,i}$ approaches μ, reaching the full weight when $v_{k,i}$ is equal to μ. Different values of $v_{k,I}$ are referred to as a structural metric codes.

In fractured rock, sharp boundaries are conceptually appropriate at boreholes edges and are possible at discrete fracture boundaries, assuming the locations of both are accurately known. While several field studies examine the merit of using regularization disconnects from supporting data (Bazin & Pfaffhuber, 2013; Doetsch et al., 2012; Orlando, 2013; Wallin et al., 2013), none have focused on the opportunities for improving fractured rock imaging.

This dissertation uses the model regularization techniques presented here coupled with the advantages of an unstructured mesh discretization to extract information from ERT datasets in fractured rock settings. This is covered in more detail in Chapters 3, 4 and 5.

CHAPTER 3: Evaluation of known-boundary and resistivity constraints for improving cross borehole DC electrical resistivity imaging of discrete fractures[1]

ABSTRACT

There is a need to better characterize discrete fractures in contaminated hard rock aquifers to determine the fate of remediation injections away from boreholes and also to evaluate hydraulic fracturing performance. A synthetic cross borehole electrical resistivity study was conducted assuming a discrete fracture model of an existing contaminated site with known fracture locations. Four boreholes and two discrete fracture zones, assumed to be the dominant electrical and hydraulically conductive pathways, were explicitly modeled within an unstructured tetrahedral mesh. We first evaluated different regularization constraints starting with an uninformed smoothness-constrained inversion, to which *a priori* information was incrementally added. We found major improvements when (1) smoothness regularization constraints were relaxed (or disconnected) along boreholes and fractures, (2) a homogeneous conductivity was assumed along boreholes, and (3) borehole conductivity constraints that could be determined from a specific conductance log were applied. We also evaluated the effect of including borehole packers on fracture zone model recovery. We found the fracture zone conductivities with the inclusion of packers were comparable to similar trials excluding the use of packers regardless of electrical potential changes. The misplacement of

[1]This chapter is published as: Robinson, J., Johnson, T., & Slater, L. (2013). Evaluation of known-boundary and resistivity constraints for improving cross-borehole DC electrical resistivity imaging of discrete fractures. *Geophysics*, *78*(3), D115–D127.

fracture regularization disconnects (FRDs) can easily be misinterpreted as actual fracture locations. Conductivities within these misplaced disconnects were near the starting model value and removing smoothing between boreholes and assumed fracture locations helped in identifying incorrectly located FRDs. Our findings demonstrate that structural constraints used after careful evaluation of *a priori* information are critical to improve imaging of fracture electrical conductivities, locations and orientations.

INTRODUCTION

Delineation of discrete fracture networks using a discrete fracture model can improve characterization and monitoring of amendment treatments into contaminated fractured rock aquifers, and provide performance assessment of hydraulic fracturing. Borehole logging and point sampling can provide information near the borehole. However, information between these point sample locations is limited and spatial interpolation of such data is highly uncertain. Determining fracture orientation is particularly important in remediation efforts to ensure amendments injections are treating targeted areas; and in hydraulic fracturing to ensure increases in porosity and permeability are in desired locations. Thus, there is a need for techniques to image discrete fracture zones and monitor transient processes occurring within these zones. Geophysical methods, in particular electrical resistivity, when constrained by appropriate supporting information (e.g. borehole geophysical logging and hydraulic testing) may potentially provide spatially continuous information at a reduced cost (Haimson and Cornet, 2003).

In fractured rock the primary fluid and electrical current pathways may be through discrete fractures. Many standard resistivity inversion packages impose a smoothness

regularization constraint to minimize model structure (deGroot-Hedlin & Constable, 1990) that is not an appropriate physical representation for this scenario. As a result, previous work in delineating fractures with electrical resistivity imaging has not extracted the maximum possible structural information from the geophysical survey. For example, Nimmer et al. (2007) used 3D surface resistance measurements in fractured basalt to monitor dilution and displacement of a conductive plume. They found that surface 3D electrical resistivity tomography (ERT) was able to define general flow patterns by imaging areas of increased and decreased resistivities, but was incapable of imaging water movement in discrete fractures. Robert et al. (2012) used 2D surface ERT in an attempt to determine preferential flow paths during a tracer study. While flow paths could be inferred from surface ERT images, the authors noted that the actual shape of the preferential path could not be determined due to the smoothness regularization in the inversion modeling. Surface electrical resistivity surveys offer limited resolution at depth due to the decreasing sensitivity with increasing distance away from the electrodes.

There have been limited cross borehole studies in fractured rock using electrical resistivity. Slater et al. (1997) used a natural tracer to image discrete fractures with cross borehole ERT supported by borehole televiewer (BHTV) observations in a fractured limestone. Although ERT inversions correlated well with the BHTV images, sensitivity was limited away from the boreholes and the features reconstructed in the resistivity image were much larger than reality because of the smoothness regularization constraint. Additionally, inversion artifacts due to a highly conductive open borehole are evident in ERT images from this study (Daily et al., 2005). A subsequent study at the same site included double packer pumping tests focused around fracture locations determined from

ERT inversion and BHTV images (Brown and Slater, 1999). Predicted fracture locations were proven to be hydraulically conductive; however differentiation of closely spaced fractures was not possible when using ERT alone due to the smoothing effects of the regularization constraints. Nimmer et al. (2007) performed a 2D cross borehole ERT study in fractured rock but boreholes were too-widely spaced, resulting in poor resolution between the boreholes.

Since a fluid-filled borehole is typically conductive compared to the surrounding host rock, the injected current at borehole electrodes is focused along the borehole, reducing current penetration into the rock (Sugimoto, 1999). This focusing causes significant modeling artifacts (Doetsch et al., 2010, Nimmer et al., 2008). When using 2D inversion codes, Nimmer et al. (2008) found that this borehole effect increases when the contrast between the fluid-filled borehole and the host rock increases. They also found this effect is magnified as the borehole diameter increases. Doetsch et al. (2010) showed that, by explicitly including the borehole in an unstructured finite element mesh, the borehole effect can be modeled, thereby minimizing such inversion artifacts. By creating independent regions for each borehole, Doetsch et al. (2010) applied a smoothness regularization within the borehole five times greater than in other regions of the mesh. They suggested that for large meshes, borehole parameters could be combined into one parameter to reduce computation time. Coscia et al. (2011) compared ERT results from field data that (1) explicitly included the borehole and (2) did not include the borehole in the mesh. They did not find a significant improvement when including the boreholes, attributing this to their unconventional measurement configuration, the small

diameter borehole (5 cm) and the low conductivity contrast (8:1) between the borehole and the surrounding formation.

Several ERT studies have recognized that the widely adopted smoothness regularization constraint is often not an accurate representation of physical conditions. One obvious situation when smoothness regularization is inappropriate involves engineered structures (Slater and Binley, 2006a). Slater and Binley (2006b) used ERT to study geochemical alteration of a permeable reactive barrier (PRB) installation over time. Since the PRB dimensions were well known, and the granular iron used to construct the PRB provided a sharp electrical conductivity contrast to the surroundings, a regularization disconnect was applied within the finite element mesh (FEM) along these boundaries whereby the electrical distribution was not smoothed during inversion modeling. Similarly, for cross borehole ERT data, Doesch et al. (2010) and Coscia et al. (2011) removed smoothness constraints from a known saturation boundary and clay layer. They found inversions without the regularization disconnect yielded variable and unrealistic resistivities within the area of interest. However, none of these studies considered the consequences for the ERT inversion if the disconnects were incorrectly located.

Recognizing a need to better delineate conductivity variations within discrete fractures away from boreholes in hard rock, this study was initiated to determine the benefits of applying appropriate physical and regularization constraints to overcome the limitations of a smoothness-constrained inversion. In particular, we investigate the utility of incorporating known fracture and borehole boundaries into the inversion mesh, enabling smoothness regularization constraints along those boundaries to be relaxed,

which allows the inversion to place a sharp conductivity contrast along the boundary without penalty. To study whether limiting the borehole conductivity effect was beneficial to recovering fractures, the use of inflatable packers to electrically isolate sections of the borehole and eliminate vertical current channeling was also simulated. Finally, the effect of misplaced regularization disconnects was also critically explored, given that regularization disconnects may be determined from subsurface information containing significant uncertainty. We find that by combining appropriate *a priori* information with measurement data in an informed inversion, resolution of discrete fracture zones can be dramatically improved. We show that regularization disconnects must be used with caution as misplaced disconnects can result in substantial image artifacts and misinterpretation of structure.

Site Model Description

This synthetic study was based on the geological setting of the Naval Air Warfare Center (NAWC) located in West Trenton (NJ), a fractured rock site contaminated with chlorinated solvents, primarily trichloroethylene. The geology and hydrogeology of this site have been extensively studied, being characterized by steeply dipping laminated and massive mudstones (Lacombe and Burton, 2010). The dominant flow pathways are through discrete fracture zones associated with black, carbon-rich intervals. A steeply-dipping mudstone unit with two electrically conductive discrete fracture zones was simulated in this study. Representative host rock conductivity was assigned based on borehole resistivity logs obtained at the site; borehole conductivities were assigned based on fluid specific conductance data available from this site. The mudstone electrical conductivity used was 0.004 S/m, (resistivity=250 Ω-m) in all but two simulations, and

the electrical conductivity of the boreholes was set at 0.05 S/m. All electrodes were below the water table. For simplicity and in the absence of other information, the electrical conductivity of the fractures was set equal to the electrical conductivity of the boreholes in all but two simulations.

METHODS

Mesh generation

An unstructured tetrahedral finite element mesh (FEM) was used to discretize the subsurface geometry. This type of mesh allows for local refinement around areas of interest or small features, such as the discrete fracture zones and boreholes of interest here (Rücker et al, 2006). Tetgen (http://tetgen.berlios.de/) was used for mesh generation. The radius-edge ratio for tetrahedron was set at 1.5 assuring a high quality mesh (i.e. there are no sliver shaped tetrahedron). The geometry of boreholes, electrode locations and fractures were all simulated based on the layout of a field experiment planned at NAWC. Borehole diameters were based on anticipated field dimensions and fracture apertures were averaged from borehole cores. Four boreholes, 9.66 cm in diameter (3.8 inches), and two fracture zones, 20.32 cm (8 inches) thick, were created as independent regions within the mesh. An independent region is defined here as a fully closed, watertight 3D polygon within the FEM. The boreholes were placed 4.5 m apart and the origin was centered on 0, 0 (x, y), resulting in center borehole coordinates which are combinations of ±2.25 m, ±2.25 m (x,y). The fractures in the mesh dip at 30° and extend to ±9 m, ±9 m (x,y). A fine mesh, referred to here as the foreground region, with boundaries ±11 m, ±11 m, -45 m (x,y,z) surrounds the four boreholes. This is encased by a mesh with larger elements, i.e. the background region, expanded to ±100 m, ±100 m, -

150 m (x,y,z) to reduce numerical boundary effects. The entire mesh is shown in Figure 3.1 (left), and a section through the center of two boreholes is shown in Figure 3.1 (right).

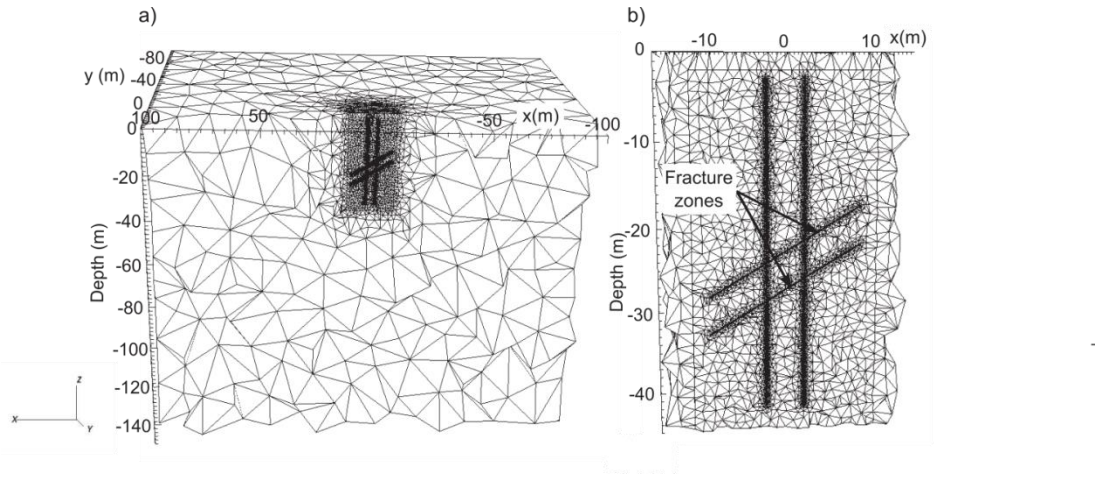

Figure 3.1: The unstructured tetrahedral mesh with 508,924 elements with a) the overall mesh and b) a section through two boreholes showing the borehole and fracture zone discretization.

Eight independent regions are incorporated within the mesh. These are four boreholes (1-4), two fracture zones (5-6), the foreground (7) and the background (8) regions. The packers represent a ninth independent region when included. The relative sizes of the boreholes and fractures are small in comparison to the overall plot dimensions, requiring a large mesh containing 508,924 tetrahedral elements.

Modeling

FERM3D, a 3D ERT resistivity code (Johnson et al., 2010), was used for (1) synthetic data generation via forward modeling, and (2) parameter estimation via inverse modeling. In this code, forward and inverse discretizations are the same and thus the conductivity of each tetrahedral element is estimated in the inversion.

a) Forward Modeling

The electric potential $V(r)$, at a point r, with current source I injected at r_s and electrical conductivity σ is governed by the Poisson equation.

$$\nabla \cdot (\sigma \nabla V) = -I\delta(|r - r_s|) \quad (3.1)$$

Boundary constraints are source-dependent mixed type boundary conditions that reproduce the analytical current flux at the boundaries arising from a homogeneous conductivity, equal to the average model conductivity (Johnson et al, 2010). In addition to refining the mesh around electrodes, singularity removal was used to reduce forward modeling errors associated with large potential gradients near current injection points (Rucker et al., 2006; Lowry et al, 1989).

A four-electrode skip-4 cross borehole sequence was used to generate measurements. In this configuration, both the current and potential electrode pairs are separated by four unused electrodes and current and source pairs do not overlap. This configuration was selected as a circulating dipole scheme with a reasonable signal to noise ratio. Fifteen electrodes in each borehole were spaced 1.1 m apart, beginning at 17 m below grade in order to straddle both fractures. Panel measurements, i.e. borehole to borehole, were created from every possible combination of boreholes, yielding 1140 simulated measurements. Using other measurement configurations (e.g. optimized arrays) (Stummer et al., 2004) and acquiring larger sequences using different electrode configurations (Binley and Kemna, 2005) could significantly improve image resolution. However, the selected measurement sequence was considered adequate for the investigation of regularization benefits of interest here.

Following creation of synthetic data, 5% random Gaussian noise was added to simulate field datasets representative of NAWC. The conductivity distribution was then estimated through inverse modeling using a homogeneous earth starting model. This procedure was followed for all models studied here. For packer models, highly resistive zones (10^{-5} S/m) were used to simulate the inflatable packers (1) in between each electrode and (2) on the exterior of end electrodes, with each borehole containing 16 packers (Figure 3.2). Potential distributions for selected skip-4 measurement configurations were generated for configurations with and without borehole packers.

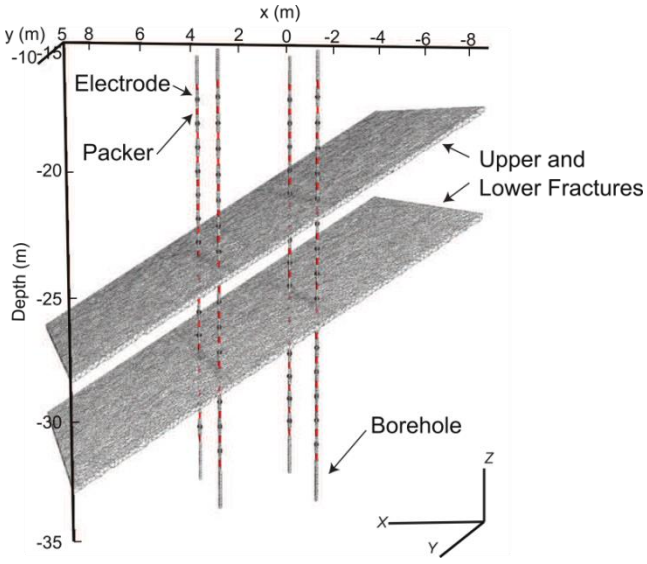

Figure 3.2: Shown is a schematic of the 4 boreholes with 15 electrodes and 16 packers in each borehole used in the packer forward model for data generation. Upper and lower fracture zones with boreholes are displayed with the mesh discretization. The model used for data generation without packers is the same as shown with the omission of borehole packers.

b) Inverse Modeling

The objective of the inversion is to solve for a conductivity distribution which minimizes the following objective function (Farquharson, 2008):

$$\boldsymbol{\Phi} = \boldsymbol{\Phi_d} + \boldsymbol{\beta}\boldsymbol{\Phi_m} \quad (3.2)$$

where:

$$\boldsymbol{\Phi_d} = \left\|\boldsymbol{W_d}\left(\boldsymbol{\phi_{obs}} - \boldsymbol{\phi_{pred}}\right)\right\|^2 \quad (3.3)$$

$$\boldsymbol{\Phi_m} = \left\|\boldsymbol{W_m}(\boldsymbol{\sigma_{est}} - \boldsymbol{\sigma_{ref}})\right\|^2 \quad (3.4)$$

In equations 3.3 and 3.4, $\| \quad \|^2$ signifies the L-2 norm. The variable Φ_d is a measure of the difference between the measured (ϕ_{obs}) and calculated data (ϕ_{pred}) from the estimated log conductivity distribution (σ_{est}) and Φ_m is a measure of the complexity in σ_{est} or a measure of the difference between σ_{est} and some preferred reference model, σ_{ref}. The parameter β optimizes the trade-off between model misfit and data misfit. W_d is a data-weighting matrix, where each data weight is equal to the reciprocal of the standard deviation, or 5% of the simulated resistance values. The model-weighting matrix (W_m) contains the model constraints, i.e. the regularization matrix. Nearest-neighbor smoothing constraints are applied per element in W_m (Constable et al., 1987) whereby the smoothness is independent of the cell aspect ratio due to the high quality mesh. Minimization of equation 3.2 leads to a linear system of equations (Binley and Kemna, 2005):

$$(\boldsymbol{J_k^T W_d^T W_d J_k} + \boldsymbol{\beta W_m^T W_m})\Delta\boldsymbol{\sigma_k} = \boldsymbol{J_k^T W_d^T W_d}[\boldsymbol{d} - f(\boldsymbol{\sigma_k})] - \boldsymbol{\beta W_m^T W_m}\left(\boldsymbol{\sigma_k} - \boldsymbol{\sigma_{ref}}\right) \quad (3.5)$$

At each iteration *k* the model update vector $\Delta\sigma_k$ is solved by a parallel conjugate gradient least squares algorithm. $\boldsymbol{J_k}$ is the Jacobian matrix at iteration *k*, where $\boldsymbol{J_{ij}} = \partial d_i/\partial m_j$ for model σ_k. We used the normalized χ^2 misfit error as the convergence criteria which is given by $\chi^2 = \frac{1}{n-1}\sum_{i=1}^{n}\frac{(d_{obs,i}-d_{pred,i})^2}{\sigma_i^2}$. The data are appropriately fit when χ^2=1. However, when a decrease in the χ^2 was not maintained in consecutive iterations, a model

with the lowest χ^2 (in some cases this value was slightly greater than 1) was chosen to not over-fit the data.

Regularization and external inversion constraints

The construction of independent regions in the mesh parameterization allows incorporation of *a priori* information, in the form of parameter and regularization constraints, i.e. $\mathbf{W_m}$ (to define smoothness constraints) and $\boldsymbol{\sigma_{ref}}$ (to constrain known conductivity values) in equation 4 above. All constraints are subject to a tolerable measurement data fit.

Figure 3.3 summarizes the types of regularization and external conductivity constraints described below in Trials 1 through 5. Our trials began with the least *a priori* information to which constraints were incrementally added. In Trial 1, we employed the nearest-neighbor smoothness regularization most often used in resistivity inversion (e.g. Kemna et al., 2002, Michot et al., 2003, Robert et al, 2012). This regularization imposes smooth model structure by defining $\boldsymbol{W_m}$ such that there is minimum variability between a parameter and its neighbors (Figure 3.3). In field studies we expect the boreholes to have a lower resistivity variation than the formation (a condition where the boreholes are homogenous is considered later). Therefore a relative smoothing weight seven times that of the formation was applied between elements within boreholes.

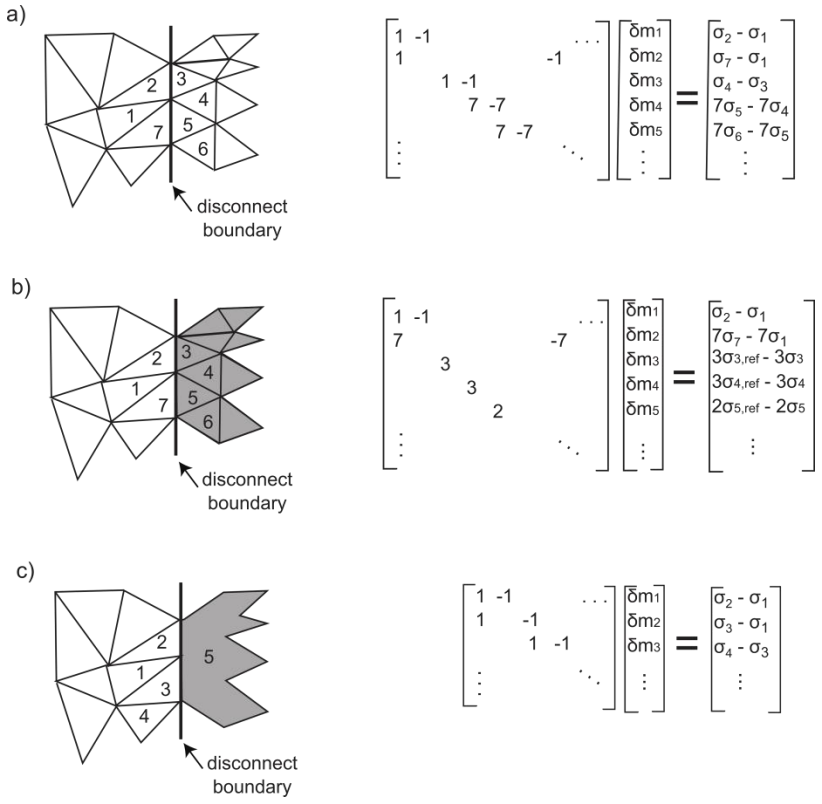

Figure 3.3: A conceptual mesh and associated regularization matrix (W_m) is shown for the constraints applied in this study. In each figure, the element number corresponds to the associated column in the regularization matrix. The left hand side vector represents the inverse solution (i.e. the log conductivity model update). The right hand side vector (also in log conductivity) completes the constraint equations. In all matrices shown a value larger than one indicates a stronger constraint (a) Shown are nearest-neighbor smoothing with a disconnect boundary. Note the constraint expressions between elements 2 and 3, and elements 7 and 5 are not included in the matrix, enabling the inversion to place a sharp contrast between these elements without penalty. (b) Same as (a) but with an external constraint applied to shaded elements. (c) Same as (b) but with a homogeneous constraint applied to all shaded elements. The inversion treats these elements as a single element and therefore solves for one conductivity value.

Trial 2 was set up as per Trial 1 except that it included a regularization disconnect between each borehole and the formation (Figure 3.3a). This constraint allows for a sharp resistivity contrast between each borehole and the formation (assuming such a contrast is supported by the data). The regularization disconnect places no quantitative constraint on the magnitude or distribution of conductivity values within boreholes or formation. In most field surveys, the borehole locations and deviations will be known;

therefore inputting the location of this regularization disconnect is straightforward and the approach is well justified.

Trial 3 was set up as per Trial 2 but also included an additional regularization disconnect between each fracture and the host rock. Anticipating that the locations of fractures could be defined within the boreholes from geophysical logs, we made a continuity assumption between boreholes to define a continuous surface (Figures 3.1 and 3.2). In field investigations, this assumption would be inherently uncertain; the consequences of incorrectly assigning a regularization disconnect are therefore explored in later trials. As per the boreholes, these regularization disconnects must be supported by the data and place no quantitative constraint on the magnitude or distribution of conductivity values within fracture zones.

Trial 4 was set up as per Trial 3, but each borehole was specified as a homogeneous region, defined here as a bounded area that the inversion will consider as one parameter (Figure 3.3c). The inversion therefore solves for a single homogeneous conductivity for each borehole. This constraint would be applicable for a well-mixed borehole in which the fluid specific conductance will not have much variation with depth. Boreholes were input as independent regions and were not constrained to be similar to one another.

Trial 5 was set up as per Trial 3, but also specifies the conductivity of the boreholes as an external constraint (Figure 3.3b). We constrained the conductivity of the boreholes to the true model value of 0.05 S/m. In a field survey, borehole conductivities could easily be estimated from fluid specific conductance logs.

Two synthetic trials were designed with packers simulated in each borehole; packers were simulated between each electrode and at the ends of the electrode array in each

borehole. The purpose of this exercise was to compare results of identical trials with and without the inclusion of packers. Packers were simulated by highly resistive (10^{-5} S/m) zones. Packer Trial 4P was set up as per Trial 4, with an additional regularization disconnect between packers and all other regions. Packer Trial 5P was set up as per Trial 5, with an additional regularization disconnect between packers and all other regions.

We also explored the importance of packers as a function of conductivity contrast between the host rock and a fluid-filled borehole (Coscia et al., 2011, Doetsch et al, 2010, Nimmer et al., 2008). We increased the conductivity contrast from 12.5 (based on the mudstone field site under investigation) to represent a higher contrast more applicable of granitic host rock. Trial 6 was set up as per Trial 5, except that the host rock conductivity was set to 0.0004 S/m i.e. a difference factor of 125 relative to the fracture/borehole conductivity (0.05 S/m). Trial 6P was set up as per Trial 6 but simulated packers (again with conductivity equal to 10^{-5} S/m).

In a field study, the assumption that borehole conductivities are equal to fracture conductivities is likely oversimplified. Therefore, two synthetic trials were designed to test the effect of fractures zones with a different conductivity than the boreholes. Trial 7 was set up as per Trial 5, except that the fracture conductivity was set to 0.25 S/m, being a factor of 5 greater than the borehole conductivity. Trial 8 was set up as per Trial 7, except that fracture conductivity was set equal to 0.01, being a factor of 5 less than the borehole conductivity.

Trials 3-8 assumed *correct* placement of regularization disconnects for the fractures in our synthetic model. Researchers apply regularization disconnects based on *a priori* information (e.g. Coscia et al, 2011) containing uncertainty; thus, these locations are also

inherently uncertain. As such, we extended our synthetic studies to investigate the effect of misplaced regularization disconnects. Trial 9 was set up as per Trial 5, except fracture regularization disconnects (FRDs) were offset from the true fracture locations by ±2 m. With misplacement of the FRDs, nearest-neighbor smoothing between the boreholes and assumed fracture locations does not exist. We examined the effect of removing smoothing between the boreholes and FRDs. Trial 9a was set up as per Trial 9, except a regularization disconnect was applied between the FRDs and boreholes.

In Trials 10 and 10a, FRDs were misplaced to intersect true fracture locations. Otherwise, Trial 10 and Trial 10a were set up as per Trial 9 and 9a respectively. Table 3.1 summarizes the regularization parameters used in the synthetic trials.

TABLE 3.1: Description of trials
BH=borehole; F=fractures; HR=host rock; P=packers;
*misplaced fracture regularization disconnect

Trial	True Model used to generate data	Regularization between independent regions	Borehole Constraints
1	BH/F = 0.05 S/m HR = 0.004 S/m	Standard smoothness regularization	7 times smoother than other regions
2		Regularization disconnect of boreholes to host rock	
3		Regularization disconnect of boreholes and fractures to host rock	
4			Homogeneous
5			External conductivities set equal to true model value
4P	BH/F = 0.05 S/m HR = 0.004 S/m P = 10^{-5} S/m		Homogeneous
5P			External conductivities set equal to true model value
6	BH/F = 0.05 S/m HR = 0.0004 S/m		
6P	BH/F = 0.05 S/m HR = 0.0004 S/m P = 10^{-5} S/m		
7	B = 0.05 S/m F = 0.25 S/m HR = 0.004 S/m		
8	B = 0.05 S/m F = 0.01 S/m HR = 0.004 S/m		
9*	BH/F = 0.05 S/m HR = 0.004 S/m		
10*			
9a*		Regularization disconnect of boreholes and fractures to host rock	
10a*		Regularization disconnect of boreholes to fractures	

RESULTS

Evaluation of the inversion results are based on (1) the recovered conductivity values within the two fracture zones compared to the true model value and (2) the presence of artifacts. Model recovery is of most interest in between and surrounding the electrodes within the boreholes. Thus, this volume is emphasized in the figures (white outline) as a 3D polygon extending 1 m beyond x-y center borehole coordinates (±3.25 m, ±3.25 m) and 1 m above and below end-borehole electrode z coordinates (-16 m to -33.4 m), and defined here as the interior region bounded by the boreholes. In Table 3.2, average upper and lower fracture conductivity and standard deviation is shown within the interior region bounded by the boreholes for each trial. The maximum and minimum standard deviations of the residuals of the logs of the resistance (in Ohms) are 0.1470 and 0.0290, respectively.

TABLE 3.2: Mean and standard deviation results within upper and lower fracture zones in the interior region bounded by the boreholes with packers and without packers

Upper Fracture Zone				
Trial	4	4P*	5	5P*
Mean (S/m)	0.0410	0.0408	0.0415	0.0420
Standard deviation (S/m)	0.0073	0.0076	0.0077	0.0074
Lower Fracture Zone				
Trial	4	4P*	5	5P*
Mean (S/m)	0.0494	0.0502	0.0497	0.0497
Standard deviation (S/m)	0.0054	0.0053	0.0054	0.0051

*Packers within boreholes

Trials 1-5

Figure 3.4 (top) shows the inversion model results for Trials 1-5 as a 2D plane through y = 2.3 m, bounded by the region of interest where x = ±10 m to a depth of 42 m. This slice is slightly off-center of two boreholes centered at (±2.25, 2.25) so that smaller mesh elements surrounding each borehole do not impede center-borehole viewing. The

dashed white outline in the top images represents the interior region bounded by the boreholes. Figure 3.4 (bottom) shows the distribution of conductivities within the two fracture zones. For reference, the true model conductivities are shown in Figure 3.4a. In viewing the progression of the trials, it is evident that as more regularization disconnects and constraints are included in the inversion then (1) the recovered model becomes more representative of the synthetic model, and (2) inversion artifacts are reduced.

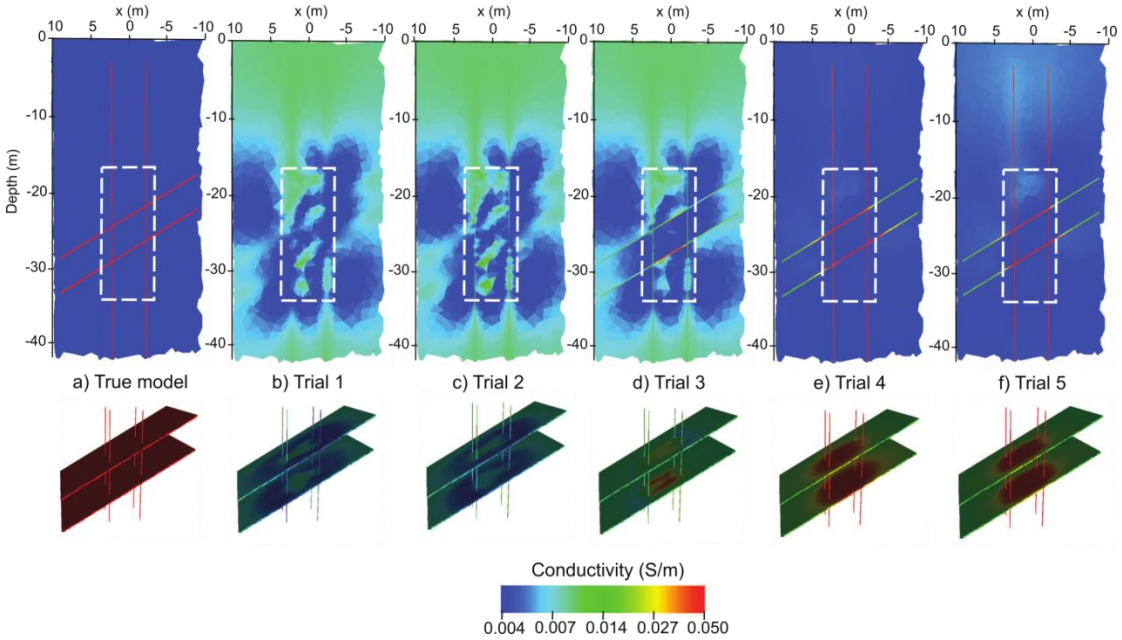

Figure 3.4: Five synthetic trials are shown with section view (top) and fracture zone view (bottom). a) Trial 1: smoothness regularization inversion, b) Trial 2: borehole regularization disconnect, c) Trial 3: borehole and fracture zone regularization disconnect, d) Trial 4: homogeneous borehole constraint with regularization disconnects at boreholes and fracture zones e) Trial 5: borehole parameter constraint with regularization disconnects at boreholes and fracture zones. The color bars on the images have been scaled to range between the true host rock conductivity, 0.004 S/m and the borehole and fracture conductivity, 0.05 S/m. The dashed white outlines in top images are the interior region bounded by the boreholes and where fractures were expected to have the best model recovery.

In Trial 1 (standard smoothness inversion) fracture zones and boreholes are poorly discernible in this image and there are many anomalous conductivity structures resulting from regularization artifacts. Trial 2 (borehole regularization disconnect) shows

no improvement from Trial 1 in recovering the fracture zones. The borehole regions can be identified visually but the image contains many of the same artifacts found in Trial 1. In Trial 3 (borehole and fracture zone regularization disconnects), there is a significant improvement in the fracture zones, and some areas in the lower fracture resolve the true conductivity of 0.05 S/m. The boreholes still contain artificial conductivity structures, especially in their upper parts where there are no electrodes and resolution is lower. Trial 4 (borehole and fracture zone regularization disconnects with a homogeneous borehole constraint) shows a major improvement over Trial 3 in resolving fracture and background conductivity both in terms of estimated fracture location and conductivity magnitude. Trial 5 (borehole and fracture zone regularization disconnects with parameter borehole constraint) is similar in appearance to Trial 4, with slightly lower background conductivities. Within the fracture zones, the model recovery values closest to the true model appear to be tightly bound between the boreholes.

The voxel conductivities in the fracture zones in the interior region bounded by the boreholes were extracted from Figure 3.4 to create the boxplots shown in Figure 3.5. Centered boxplot lines indicate the median, while outlier values (values 1.5 times larger than the difference between the boxed 25^{th} and 75^{th} percentiles) are shown as red dots. In the upper fracture, Trials 1-3 do not have any parameter values that resolve the true model value of 0.05 S/m; in the lower fracture only Trials 4 and 5 have a median value near the target value. The lower fracture meets the target value very well in Trials 4 and 5.

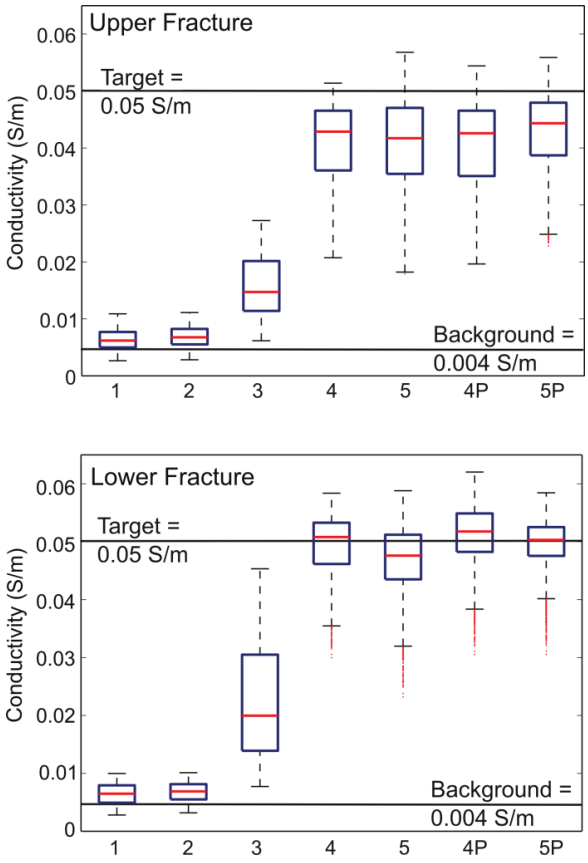

Figure 3.5: Shown are boxplots of inverted conductivity within upper and lower fracture zones of Trials 1-5 in the interior region bounded by the boreholes. As additional regularization disconnects and a priori information is added to constrain the inversion, the resulting conductivity distribution improves. Trials 4P and 5P contained packers within each borehole. No distinct improvement is shown when packers are added to the model.

Trials 4P-5P: Packer model inversion results

Analysis of the difference in the electrical potential distribution resulting from simulating packers is one way to evaluate the likely effectiveness of packers in limiting the borehole effect. A comparison of potentials where packers versus no packers are simulated within boreholes is shown in Figure 3.6 as a contoured percentage change in potential distribution between a packer and non-packer forward model. The example current injection is for two current electrodes in a single borehole (just one configuration in the measurement sequence). The highest changes in potential (i.e. ±5 %) are shown

near the packer locations in the injection borehole, resulting in higher current densities in the host rock, especially near injection electrodes.

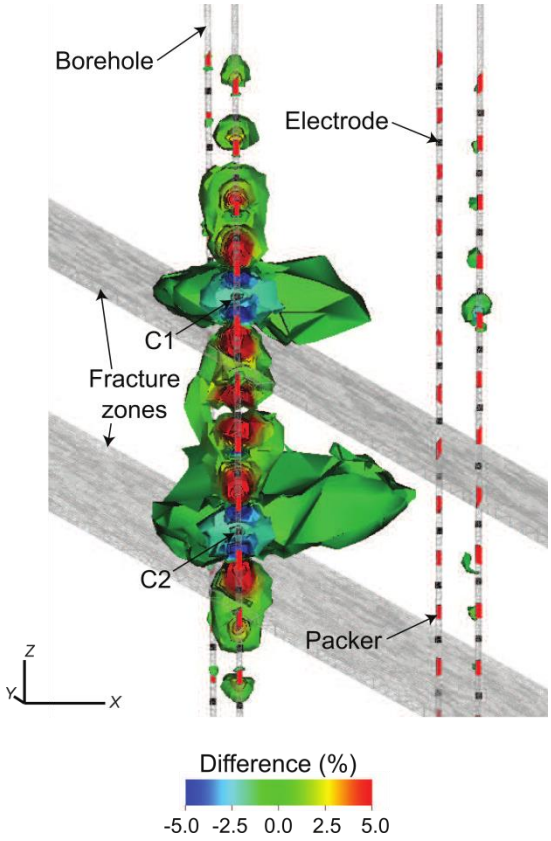

Figure 3.6: Potential differences (%) are displayed between a model with and without packers shown for a single example current injection. The transparent host rock is inclusive of all areas surrounding the boreholes and fracture zones. With the inclusion of packers the equipotential change extends farther into the host rock.

Inversion images from Trials 4P and 5P appear almost identical to Trials 4 and 5 and thus are not shown for brevity. These conductivity distributions show (1) well-resolved boreholes and fracture zones in between boreholes (Figure 3.5, 4P and 5P) and (2) minimal artifacts outside of borehole and fracture zone regions. Table 3.2 is a comparison of the mean and standard deviation within fracture zones for trials that differ only with the addition of packers. As in the boxplots (Figure 3.5), fracture zones in the

interior region bounded by the boreholes were used as boundaries to compile these results. Trials 4 and 4P are very similar to Trials 5 and 5P. Across these trials the ranges in the upper and lower fractures zones are 0.0012 S/m and 0.0008 S/m, respectively.

Trials 6 and 6P: Packer and non-packer models within a more resistive rock

Figure 3.7 shows the inversion images for Trial 6 (no-packer) and Trial 6P (packer simulated) in the same orientation as Figure 3.4. Note the lowest conductivity value in the scale is 0.0004 S/m, such that the locations of borehole packers are shown with the lowest conductivities in each borehole and blend in with the host rock. Both Trial 6 and Trial 6P inversions resolved the true fracture zone conductivity at a distance farther away from the boreholes compared to Trials 1-5. Changes in the potential distribution between packer and non-packer models are significantly greater for this higher resistivity contrast, with percentages greater than 25% surrounding packers near the injection electrodes (not shown). For Trial 6, the mean upper and lower fracture zone conductivity in the interior region bounded by the boreholes was 0.0500 S/m and 0.0511 S/m, respectively. In Trial 6P, these values were 0.0499 S/m and 0.0510 S/m, respectively. Figures 3.7a and 3.7b appear almost identical with the exception of borehole packers in Figure 3.7b.

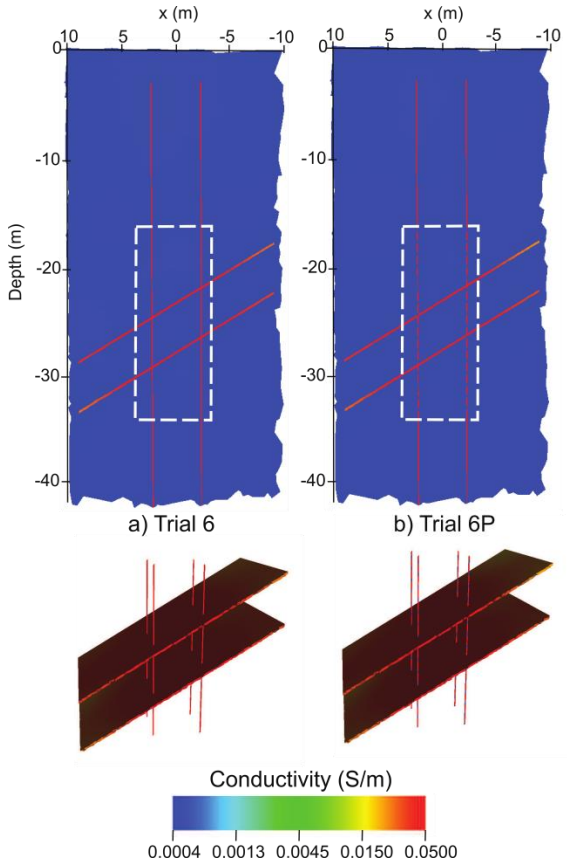

Figure 3.7: Shown are inversion results for two synthetic models with factor of 125 differences between the host rock and the boreholes/fractures showing section view (top) and fracture zone view (bottom). All regularization constraints and a priori information are the same between the two models except Trial 6 (a) does not contains packers while Trial 6P (b) contains packers. The resulting inversion models appear almost identical showing no strong improvement with the addition of borehole packers. The dashed white outline in top images defines the interior region bounded by boreholes.

Trials 7 and 8: Fracture conductivity not equal to borehole conductivity

In Trial 7 (fracture conductivity (0.25 S/m) is 5 times greater than borehole conductivity) the average upper and lower fracture conductivities resolved in the interior region bounded by the boreholes were 0.21 S/m and 0.24 S/m, respectively. The host rock (i.e. foreground region) is well resolved (not shown) with no visible artifacts. The average conductivity within the upper and lower fracture zones for Trial 8 (true model fracture conductivity (0.01 S/m) is 5 times less than borehole conductivity) is 0.0160 S/m and

0.0169 S/m, respectively. The foreground region is again well resolved (not shown). The boxplot in Figure 3.8 shows the fracture zone percentiles and conductivity range for Trials 7 and 8 in the interior region bounded by the boreholes.

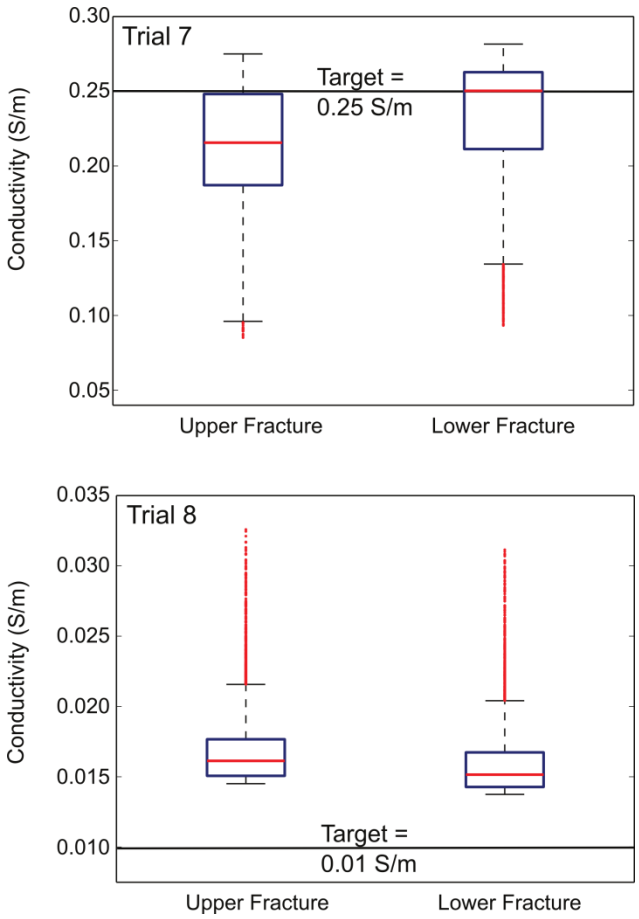

Figure 3.8: Boxplots of inverted conductivity are shown for Trials 7 and 8 within the upper and lower fracture zones in the interior region bounded by the boreholes. The true model fracture conductivities are indicated on each plot.

Trials 9 and 9a: Fracture regularization disconnects offset by ±2 m

Inversion images for Trials 9 and 9a are shown in Figure 3.9a and 3.9b. For comparative purposes, the orientation of Figure 3.9 is identical to Figures 3.4 and 3.7. However, to better focus on results within the depth limits of the electrode array, the depth range was reduced to 20 m (i.e. 13 to 37 m depth). For reference, the actual

fracture locations are annotated and shown as a black outline (Figure 3.9, top). In Trial 9, (smoothness constraint between the boreholes and FRDs) the FRDs have higher conductivities within the interior region bounded by the boreholes. The highest conductivities within these disconnects (shown in yellow and red) are focused along 2D exterior planes connecting the boreholes (Figure 3.9a, bottom). Excluding these higher values, the conductivities within the FRDs are close to the starting inverse model value of 0.010 S/m. There is a noticeable difference in the foreground conductivities above and below the FRDs compared to in between these misplaced regions. The FRDs appear to be bounding these two areas, especially -2.25 m to -10 m (x) in the lower FRD and 2.25 m to 10 m (x) in the upper FRD. In the proximity of the true fractures, there are localized higher conductivities within the interior region bounded by the boreholes.

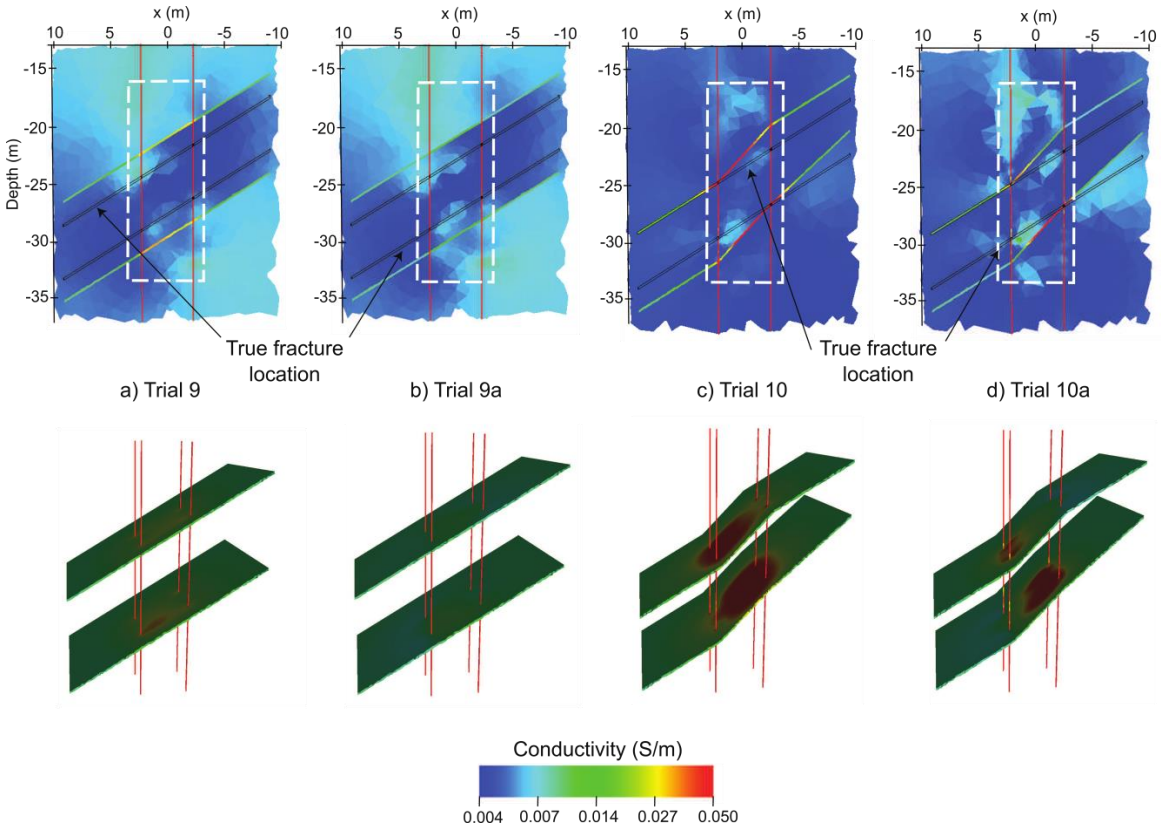

Figure 3.9: Inversion results are displayed where FRDs are applied in an incorrect location. True fracture locations are shown (top). In (a) and (b) the FRD is offset by ±2 m. In (c) and (d) the FRDs intersect the true fracture location. In Trials 9 (a) and 10 (c), a regularization disconnect is defined between the boreholes and host rock. In Trials 9a (b) and 10a (d), there is a smoothness constraint between the boreholes and the host rock. The dashed white outline in top images defines the interior region bounded by the boreholes.

Trial 9a (regularization disconnect between FRDs and each borehole) shows higher conductivities surrounding each borehole, with the majority of the upper and lower FRD parameters having conductivities near the starting inverse model (0.010 S/m). The areas above and below the FRDs appear identical to Trial 9. Near the true fracture locations, areas of higher conductivity are more pronounced compared to Trial 9. Figure 3.10 is a boxplot of parameter conductivities within the upper and lower FRDs in the interior region bounded by the boreholes). This plot shows (1) the range of conductivities for Trial 9 is significantly higher than in Trial 9a and (2) the median conductivity for all parameters in Trial 9a is near the starting homogeneous inverse

model (0.010 S/m). Within the interior region bounded by the boreholes, average conductivities within the upper FRD are 0.0260 S/m and 0.0129 S/m for Trials 9 and 9a, respectively; within the lower FRD, these values are 0.0280 S/m and 0.0124 S/m for Trials 9 and 9a, respectively.

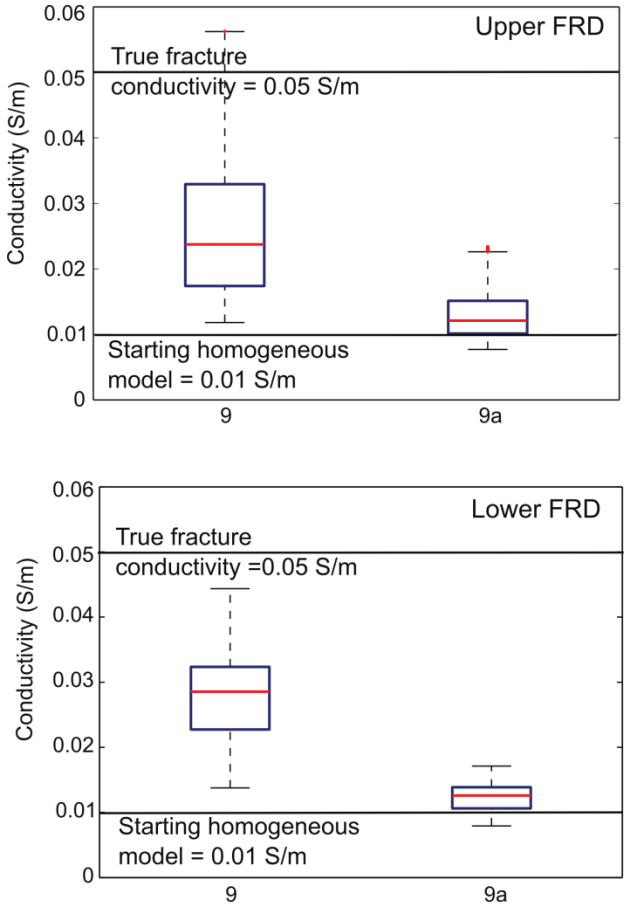

Figure 3.10: Shown are boxplots of inverted conductivities within upper and lower FRDs of Trials 9 and 9a in the interior region bounded by the boreholes. FRDs were offset by ±2 m from actual fracture locations for these trials.

Trials 10 and 10a: Misplaced fracture regularization disconnects that intersect true fractures

Inversion images for Trials 10 and 10a are shown in Figures 3.9c and 3.9d. In Trial 10 (smoothness constraint between the FRDs and the boreholes) many conductivity

values within the FRDs are near the actual fracture conductivity of 0.05 S/m in the interior region bounded by the boreholes. Parameters outside of the interior region bounded by the boreholes have values near the starting homogeneous model value of 0.01 S/m. The foreground conductivities are near the true model conductivity (0.004 S/m) with few artifacts (Figure 3.9c, top). Localized areas of high conductivities are shown in the true fracture positions.

In Trial 10a, (regularization disconnect defined between FRDs and boreholes) high conductivities in the upper and lower FRDs do not extend as far between the boreholes compared to Trial 10. Conductivities within the upper and lower FRDs vary depending on proximity to boreholes and actual fracture locations. Clearly, if the locations of the FRDs are considered correct, the results of Trial 10, not Trial 10a, would be considered plausible and fractures would be interpreted at the misplaced locations.

DISCUSSION

The need to use realistic regularization constraints and *a priori* information to invert electrical resistance measurements for reliable electrical conductivity distributions in a fractured rock setting characterized by discrete fracture networks is clearly evident in this synthetic study. For Trials 1 through 5, as additional regularization constraints were added, the true fracture conductivity was clearly better resolved (Figure 3.4). Trial 1, which represents a standard regularized inversion, yielded the worst recovery of the fracture zones, with fracture conductivity magnitudes well below true-model values (Figure 3.4b). Furthermore, the image is heavily affected by artifacts. The regularization disconnect of the boreholes from the host rock in Trial 2 provided little additional recovery benefit within the fractures (Figure 3.4c) showing that the fine fracture

discretization and/or removing nearest-neighbor smoothing alone will not adequately resolve discrete fractures. An additional regularization disconnect between the boreholes and fracture zones (which could be estimated from borehole logs in a field study) results in better location of discrete features; however, the conductivities were still well-below the true model value (Figure 3.4d).

A major improvement in fracture location and conductivity estimation occurs when additional information on the conductivity within the boreholes is included. Improvements are found when (1) a homogeneous borehole conductivity constraint (Trial 4), or (2) a known borehole conductivity constraint (Trial 5), is added in addition to borehole and fracture zone regularization disconnects. The similarity in results obtained from these two constraints is likely due to the fact that the synthetic model is characterized by homogeneous boreholes with a single conductivity. These findings clearly show that information on the borehole, although representing a small part of the mesh, is critical to reliably characterizing discrete fractures with ERT.

The addition of simulated packers in Trials 4P and 5P results in no clear improvement in the model recovery of conductivities of discrete fractures over Trials 4 and 5 (Table 3.2), although clear differences in the potential distribution during current injection exist with the inclusion of packers (Figure 3.6). Adding packers and increasing the conductivity difference between host rock and borehole from 12.5 to 125 (Trials 6 and 6P) does not significantly improve the recovery of discrete fracture zones, despite a greater difference in potentials between the packer and non-packer models. However, we caution that field studies are needed to further explore whether the inclusion of packers provides any benefit when imaging discrete fractures with cross-borehole ERT.

Conductivities of discrete fracture zones were well resolved when true model fracture conductivities were either greater than (Trial 7) or less than borehole conductivities (Trial 8). For Trial 7, the average fracture conductivity values (0.21 S/m and 0.24 S/m) were below the true model value (0.25 S/m) and in Trial 8, the average fracture conductivity values (0.160 S/m and 0.169 S/m) were above the true model value (0.010 S/m). Figure 4.8 also shows a long tail following this trend for each trial. We attribute this result to the smoothness regularization between the boreholes and fractures causing the parameters near the boreholes to be adjusted (i.e. lowered or raised) to the borehole conductivity constraint of 0.05 S/m. These results are promising in moving to a field study where differences in fracture and borehole conductivities are likely.

When FRDs were misplaced to offset true fracture locations (Trials 9-9a) the parameters in the misplaced region should have been resolved equal to the true model host rock value of 0.004 S/m. However, many of the parameters in the misplaced FRDs were incorrectly estimated to have conductivities close to the starting homogeneous model. When there is nearest-neighbor smoothing between the boreholes and the FRDs (Trial 9), it is likely that a fracture would be interpreted at an incorrect location in the inverted models because of the resolved conductivity contrast (Figure 3.9a). When smoothness constraints are removed between the boreholes and FRDs (Figure 3.9b) the higher conductivities within the misplaced FRDs are less pronounced (Figure 3.10) i.e. without the regularization smoothing from the boreholes, the data does not support higher conductivities in between the boreholes within the misplaced FRD. A problem with the inverse solution for these misplaced FRDs is recognizable because many of the resolved conductivities within these disconnected regions are near the starting homogeneous

model value. Further tests (not shown here for brevity) using a different starting homogeneous model value gave the same results i.e. inverse solution values in the misplaced FRDs were near the starting homogeneous model value. In these cases, we presume that since the misplaced FRDs are small in comparison to the overall dimensions, the numerical modeling was able to fit the data by making small adjustments to the starting model. Within the interior region bounded by the boreholes, we presume larger changes in conductivity at true fracture locations are not evident due to smoothness constraints.

In Trials 10 and 10a (misplaced FRDs intersect the true fracture location) conductivities near the true model value of 0.05 S/m do not appear continuous in between the boreholes. While Trial 10a (Figure 3.9d) is closer to the true conductivity model and the host rock conductivity distribution indicate higher conductivities at true fracture locations, the misplaced FRDs are resolved with a conductivity close to the fracture zone/borehole conductivity. This is clearly a severe artifact of the regularization constraints applied here. Trials 9-9a and 10-10a highlight the fact that (1) incorrect placement of regularization disconnects and (2) applying nearest-neighbor smoothness constraints without a clear understanding of the impact on the inverse solution can have severe interpretive consequences, leading to incorrect conclusions regarding the location of discrete fractures.

If removing nearest-neighbor smoothing between boreholes and misplaced FRDs helps in identifying *incorrectly* placed FRDs (i.e. with these regions remaining near the starting model value), then the validity of applying this information must be considered when the FRDs are *correctly* located. With this is mind, we removed smoothness

constraints between boreholes and fracture zones for Trial 5. Figure 3.11 is a comparison of fracture conductivities in the interior region bounded by the boreholes with and without this smoothness constraint.

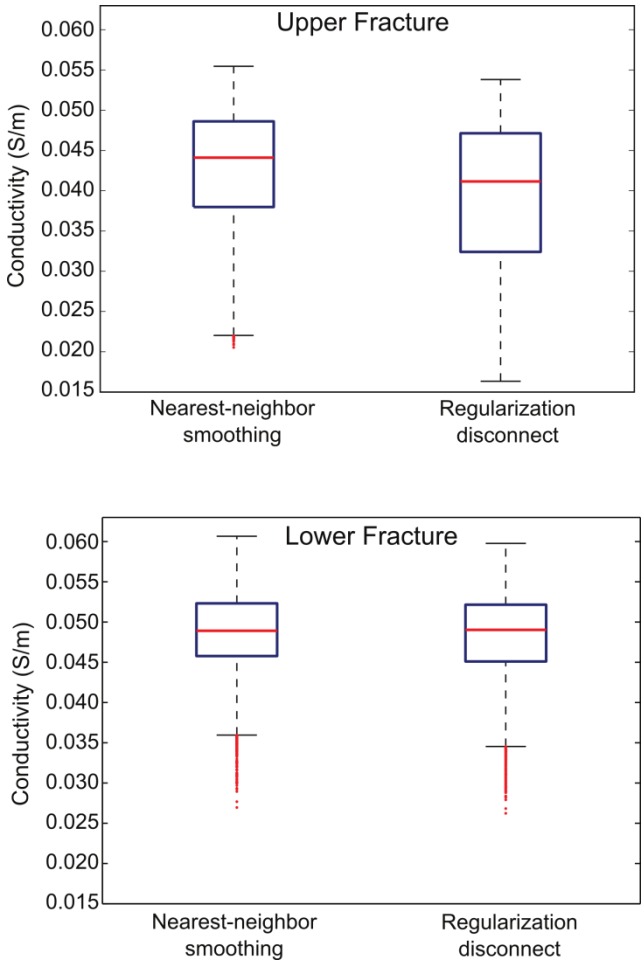

Figure 3.11: Boxplots of inverted conductivity are displayed within upper and lower fracture zones in the interior region bounded by the boreholes of Trials 5 where there is 1) nearest-neighbor smoothing between boreholes and fractures and 2) regularization disconnects between boreholes and fractures.

The conductivities within the upper and lower fractures are very similar because the inversion is subject to a tolerable data fit and the measurement data supports these conductivities. While the range is higher and median values lower with a regularization disconnect between the borehole and fractures, the two solutions yield comparable results.

CONCLUSIONS

This study has shown that in a fractured rock setting, orientation, location, and conductivity magnitudes for discrete fractures can only be recovered using electrical resistivity imaging when supporting data allows for additional modeling parameterization and regularization constraints. Standard smoothness inversions assuming a discrete fracture model in fractured rock are not adequate to resolve fracture zones as was evidenced in the model recovery images as well as sensitivity plots. As additional *a priori* information is added, the recovered model is more representative of the true model. The fracture zones in synthetic models that contained borehole packers were resolved as well as models that did not contain borehole packers; synthetic models where the borehole conductivity was greater than or less than the fracture conductivity were also shown to be well resolved in the fracture zones.

These synthetic trials illustrate the potential benefits of (1) explicitly including boreholes and fracture zones in the mesh, (2) defining regularization disconnects between the boreholes, fractures and host rock, and (3) homogenizing or explicitly including conductivities where appropriate. The conductivity of a borehole can in principle easily be defined from a specific conductance log and inclusion of this information was shown to be critical in reducing foreground artifacts and resolving fractures. FRDs can be defined from borehole logging data if assumptions about fracture continuity are made between boreholes. However, the correct placement of regularization disconnects is critical and misplacement can lead to an incorrect interpretation of data, especially without carefully evaluating the inversion results. The validity of constraints should be

checked with all available data, i.e. for this case, borehole logs, due to the inherent heterogeneity in fractured rock.

This study has provided valuable insights into strategies to improve use of electrical resistivity imaging in fracture rock environments where a discrete fracture model is assumed, including the benefits and consequences of using regularization disconnects combined with *a priori* information. This can be valuable in monitoring amendment treatments in fractured rock aquifers and evaluating hydraulic fracturing performance.

ACKNOWLEDGEMENTS

We are grateful to Dimitrios Ntarlagiannis for computer support. We also thank Pierre Lacombe of USGS for providing field background information used as a basis for this study. Inverse computations were performed on the Pacific Northwest National Laboratory Institutional Computing System (http://pic.pnnl.gov). Funding for this project was provided by the U.S. Department of Defense (DOD) under the Environmental Security Technology Certification Program ER 201118 (L. Slater, PI). The constructive review comments of Colin G. Farquharson and two anonymous reviewers substantially improved this manuscript.

CHAPTER 4: Challenges and Opportunities for Fractured Rock Imaging Using 3D Cross Borehole Electrical Resistivity[2]

ABSTRACT

There is an increasing need to characterize discrete fractures away from boreholes to better define fracture distributions and monitor solute transport. We performed a 3D evaluation of static and time-lapse cross-borehole electrical resistivity tomography (ERT) datasets from a limestone quarry where flow and transport is controlled by a bedding-plane feature. Ten boreholes were discretized using an unstructured tetrahedral mesh and 2D panel measurements were inverted for a 3D distribution of conductivity. We evaluate the benefits of 3D versus 2.5D inversion of ERT data in fractured rock while including the use of borehole regularization disconnects (BRD) and borehole conductivity constraints. High conductivity halos (inversion artifacts) surrounding boreholes were removed in static images when BRDs and borehole conductivity constraints were implemented. Furthermore, applying these constraints focused transient changes in conductivity resulting from solute transport on the bedding plane, providing a more physically reasonable model for conductivity changes associated with solute transport at this fractured rock site. Assuming bedding plane continuity between fractures identified in borehole televiewer (BHTV) data, we discretized a planar region between six boreholes and applied a fracture regularization disconnect (FRD). Although the FRD appropriately focused conductivity changes on the bedding plane, the conductivity

---

[2] This chapter will be published as: Robinson, J., Johnson, T., & Slater, L. (2015). Challenges and Opportunities for Fractured Rock Imaging Using 3D Cross Borehole Electrical Resistivity. *Geophysics*, *80*(2), 1–13.

distribution within the discretized fracture was non-unique and dependent on the starting homogeneous model conductivity. Synthetic studies performed to better explain field observations showed that inaccurate electrode locations in boreholes resulted in low conductivity halos surrounding borehole locations. These synthetic studies also show the recovery of the true conductivity within an FRD depends on the conductivity contrast between the host rock and fractures. Our findings show the potential exists to improve imaging of fractured rock through 3D inversion and accurate modeling of boreholes. However, de-regularization of localized features can result in significant electrical conductivity artifacts, especially when representing features with a high degree of spatial uncertainty.

INTRODUCTION

Groundwater flow through fractured rock is primarily focused within the secondary porosity provided by discrete fractures. While this secondary porosity is typically small relative to the primary porosity in fractured rock, it determines hydraulic connectivity. Discrete fractures therefore exert a strong control over the transport of groundwater and contaminants. Information from boreholes such as geophysical logs, groundwater samples and hydraulic tests can provide fine detail at discrete locations. However, it is usually impractical, cost prohibitive and too invasive to drill enough boreholes to accurately interpolate parameters determining flow and transport properties within discrete fractures. Yet, there is an increasing need to characterize permeable features in fractured rock beyond the vicinity of well locations in order to monitor remediation, contaminant transport and hydrofracturing. Electrical resistivity tomography (ERT) is potentially well-suited for imaging fracture zones in fractured rock as electrical current

flow is primarily electrolytic via the secondary porosity associated with the fractures, i.e. the electrical current flow paths are (to first order) the same as the fluid flow paths (assuming surface conduction is small).

While the advantages of 3D versus 2D ERT are well recognized (Chambers et al., 2002; Wilkinson et al., 2006), 2D cross borehole surveys in fractured rock have previously been performed because of 1) the lower cost and ease of acquiring 2D panel compared to 3D measurements 2) a 3D array of boreholes is often unavailable and 3) 2D numerical modeling of ERT data is less computationally demanding. With the advent of 3D codes and greater computational power, analyzing 3D ERT datasets and parameterizing finer features (e.g. boreholes) has become possible and shown to be beneficial. For example, Doetsch et al. (2010) performed 3D cross-borehole ERT measurements in a gravel aquifer overlain with a fine-silt and clay aquitard, demonstrating that explicitly incorporating boreholes in the parameterization reduced inversion artifacts otherwise caused by the presence of a conductive borehole.

Sharp electrical conductivity contrasts at discrete fractures and boreholes require care in ERT inversion. As many solutions will fit data equally well, the most popular methodology for ERT imaging is to resolve the least amount of structure in a geologically meaningful model (deGroot-Hedlin & Constable, 1990), commonly referred to as smoothness constrained inversion. Clearly, this approach is unlikely to produce the most meaningful geological mftable ofodel for fractured rock. Consequently, the hydrogeological information obtained from previous cross borehole ERT studies using smoothness regularization was limited (Slater et al., 1996; Slater et al., 1997). More recent cross-borehole ERT studies have proposed ‘regularization disconnect’ solutions to

this problem when large electrical conductivity contrasts are expected across sharp spatial boundaries. One of the earliest examples employed a smoothing disconnect boundary in the regularization to represent the design specifications of an engineered structure where the location of the boundary was precisely known (Slater & Binley, 2006). More recently, Coscia et al., (2011) removed smoothness constraints along a well-defined clay layer boundary.

Improved ERT imaging of fractured rock might be expected when the sharp conductivity contrast between the rock matrix and boreholes is correctly modeled. Boreholes can be positioned quite accurately in the model space if a borehole deviation log is recorded. Some previous field ERT cross-borehole studies assume boreholes to be vertical due to a lack of information (Slater et al., 1996; Slater et al., 1997; Johnson et al., 2012). However, electrode mis-location can lead to systematic errors in the inversion that cannot be captured through standard reciprocity or stacking checks that are commonly used to characterize data errors (Oldenborger et al., 2005; Wilkinson et al. 2008). For example, Coscia et al., (2011) compared inversions where known borehole deviations were included and not included in the inversion. They found that a resistive layer known to be continuous at the study site appeared discontinuous when borehole deviations were not considered in the inverse modeling.

Further improvement in ERT imaging of the conductivity structure within discrete fracture zones might also be expected if the locations of fractures within the imaged volume could be accurately defined from borehole logging data, such that fracture zones could be appropriately discretized and smoothness constraints removed across fracture boundaries. The applicability of this approach would strongly depend on how accurately

fracture zone boundaries between boreholes could be interpolated. Synthetic studies have recently shown how mis-location of disconnect boundaries in smoothness-constrained inversions can lead to a misinterpretation of ERT data (Robinson et al., 2013).

Several studies have recognized the benefit of combining regularization disconnects with prior information on the electrical conductivity structure at known locations into the inversion modeling. Orlando (2013) used results from a damped-least squares minimization combined with smoothness inversion to constrain conductivities within a tomb. Johnson et al. (2012) applied conductivity constraints through semivariogram models and a near-borehole electrical conductivity structure generated from a smoothness-constrained ERT inversion. Robinson et al. (2013) demonstrated synthetic cases where the inclusion of regularization disconnects in addition to borehole conductivity constraints dramatically improved the imaging of simulated discrete bedding-plane like fractures. Bazin & Pfaffhuber (2013) acknowledged the benefits of imposing conductivity constraints below a bedrock boundary, but favored using only regularization disconnects at this boundary due to the potential unreliability of borehole resistivity data.

Here, we build on the synthetic studies of Robinson et al. (2013) that focused on methods to improve ERT characterization of fractured rock by evaluating the general effects of localized de-regularization and constraints on the inversion surrounding boreholes and assumed fracture locations. We evaluate the information content of field ERT data acquired at a limestone quarry in the United Kingdom (UK) where a dominant bedding plane controls the local hydrogeology and groundwater quality. The datasets, collected in the mid-1990s, consist of static and time-lapse cross borehole ERT data

(Slater et al., 1996; Slater et al., 1997), borehole televiewer (BHTV) borehole logs and hydraulic conductivity data from focused packer testing (Brown & Slater, 1999). The dataset was acquired in 2D panels that were never modeled in 3D due to the lack of 3D ERT codes at the time of the study. We first compare static and time-lapse 3D ERT inversions against results obtained from 2.5D imaging. We then demonstrate the benefits of removing smoothness constraints at borehole boundaries in field data while incorporating borehole conductivity information (e.g. from borehole fluid specific conductance logs) as prior information. Using borehole data to define a fracture plane, the effects of removing smoothness constraints at fracture boundaries are discussed. The origins of borehole artifacts in the inversions of field data are then investigated through synthetic modeling. ERT conductivity recovery limitations in fractured rock are also investigated using synthetic examples that include borehole conductivity constraints, along with removal of smoothness constraints at assumed fracture locations.

ELECTRICAL RESISTIVITY TOMOGRAPHY (ERT)

Electrical resistivity (ρ) or its inverse electrical conductivity (σ), is a physical property of the subsurface which is a measure of how strongly a material opposes the flow of an electric current. Sequences of direct current (DC) electrical resistance measurements can be modeled to determine the subsurface electric potential distribution arising from current injection into a heterogeneous conductivity distribution.

Inversion of ERT data is inherently underdetermined (i.e. non-unique), such that the inverse problem is typically formulated as a regularized optimization problem where model constraints are imposed to limit the number of possible solutions. The objective function optimizes the tradeoff between the weighted data misfit and model constraints

(Binley & Kemna, 2005; Sasaki, 1994). Minimization of the objective function leads to a linear system of equations (e.g. Backus & Gilbert, 1968; Binley & Kemna, 2005),

$$(\boldsymbol{J_k^T W_d^T W_d J_k} + \propto \boldsymbol{W_m^T W_m})\Delta \boldsymbol{m_k} = \boldsymbol{J_k^T W_d^T W_d}[\boldsymbol{d} - f(\boldsymbol{m_k})] - \propto \boldsymbol{W_m^T W_m}(\boldsymbol{m_k} - \boldsymbol{m_{ref}}), \quad (4.1)$$

The L-2 norm is commonly used, although other norm measures can be implemented (Farquharson, 2008). A regularization parameter ($\propto$) optimizes the trade-off between model misfit and data misfit. A data weighting matrix ($\boldsymbol{W_d}$) equal to the reciprocal of the individual standard deviations is defined by a data error model discussed later. The model-weighting matrix ($\boldsymbol{W_m}$) contains the model constraints and is also known as the regularization matrix.

At each iteration *k* the model update vector $\Delta \boldsymbol{m_k}$ can be solved e.g. by a conjugate gradient least squares algorithm (Günther et al., 2006; Zhang, 1995). After the first iteration, the reference model, $\boldsymbol{m_{ref}}$, is assigned the value from $\boldsymbol{m_{k-1}}$ or an already-specified expected conductivity value. $\boldsymbol{J_k}$ is the Jacobian matrix at iteration *k*, where each member $J_{ij} = \partial f_i(m_k)/\partial m_j$ for model $\boldsymbol{m_k}$. The normalized χ^2 misfit error is used as the convergence criteria which is given by

$$\chi^2 = \frac{1}{n-1}\sum_{i=1}^{n}\frac{(d_{obs,i} - f_i(m))^2}{SD_i^2}, \quad (4.2)$$

where n is the number of observations and SD_i is the standard deviation for measurement i. Assuming measurement errors are correctly quantified, independent and normally distributed the appropriate χ^2 value at convergence is unity in the absence of numerical modeling errors.

Time-lapse ERT datasets can be collected to monitor or delineate conductivity changes due to hydrological processes such as the introduction of a contaminant/tracer, salt-water intrusion, and/or porosity changes. One approach to evaluating time-lapse ERT (Labrecque and Yang, 2001) involves inversion of a background dataset; the data difference from the background dataset is inverted which is in the form:

$$\Delta \boldsymbol{D} = \left(\boldsymbol{d_{obs}} - \boldsymbol{d^0_{obs}}\right) - [\boldsymbol{f}(\boldsymbol{m_i}) - \boldsymbol{f}(\boldsymbol{m^0})], \quad (4.3)$$

where $\boldsymbol{d_{obs}}$ is the observed data, $\boldsymbol{d^0_{obs}}$ is the observed background data, $f(\boldsymbol{m_i})$ is the data simulated from the current iteration i for the time-lapse model, and $f(\boldsymbol{m^0})$ is the data derived from the background model. Model parameters are regularized to the background conductivities, $\boldsymbol{m^0}$, thus modeled changes in conductivity ($\Delta \boldsymbol{D}$) are relative to the background time. The minimization of the modified objective function takes the form,

$$(\boldsymbol{J_k^T W_d^T W_d J_k} + \propto \mathbf{W_m^T W_m})\Delta \boldsymbol{m_k} = \boldsymbol{J_k^T W_d^T W_d} \Delta \boldsymbol{D} - \propto \boldsymbol{W_m^T W_m}(\boldsymbol{m_k} - \boldsymbol{m^0}), \quad (4.4)$$

and the same normalized χ^2 misfit error is used as defined above.

REGULARIZATION DISCONNECTS AND CONDUCTIVITY CONSTRAINTS

Model constraints in the regularization matrix $\boldsymbol{W_m}$ usually employ nearest neighbor smoothing as described in deGroot-Hedlin & Constable (1990). Specifically, a similarity constraint equation is included between adjacent elements in the formulation of $\boldsymbol{W_m}$ (Figure 4.1a), as shown between elements 1 and 2; and relative weighting between elements can be adjusted as shown between elements 1 and 7 (Figure 4.1a). Since more than one model can be fit to ERT data (Backus & Gilbert, 1968; Binley & Kemna, 2005), regularization constraints have been modified to better agree with available field information. Smoothness constraints between different regions in the discretization can

be relaxed or 'disconnected'(Figure 4.1b) by removing a constraint equation between elements in the formulation of $\boldsymbol{W_m}$, hence de-regularizing a region. For example, in Figure 4.1a, a constraint equation is omitted between elements 2 and 3. Such a regularization disconnect (RD) enables the inversion to place a sharp conductivity contrast across a boundary, if supported by the data, without penalty. Note that an RD does not constrain a parameter to a specific conductivity value. If the conductivity is known within particular elements in the model space (e.g. from a borehole conductivity probe), the conductivity within these elements can be constrained to this value, and relative weighting can also be adjusted (Figure 4.1a), as shown in the last three constraint equations. We refer the reader to Robinson et al., (2013) for a more details regarding regularization disconnects.

In fractured rock, RDs are conceptually appropriate at boreholes edges and also possibly at the edges of discrete fracture boundaries, assuming the locations of both are accurately known (J. Robinson, Johnson, et al., 2013). While several field studies examine the merit of using RDs from supporting data (Bazin & Pfaffhuber, 2013; Doetsch et al., 2012; Orlando, 2013; Wallin et al., 2013), none have focused on the opportunities for improving fractured rock imaging. More significantly, these studies have not explored the potential pitfalls when such RDs, whose boundaries may not be precisely known, are misplaced. For this reason, we explore the effect of uncertainties associated with localized de-regularization and evaluate the potential consequences of mis-location.

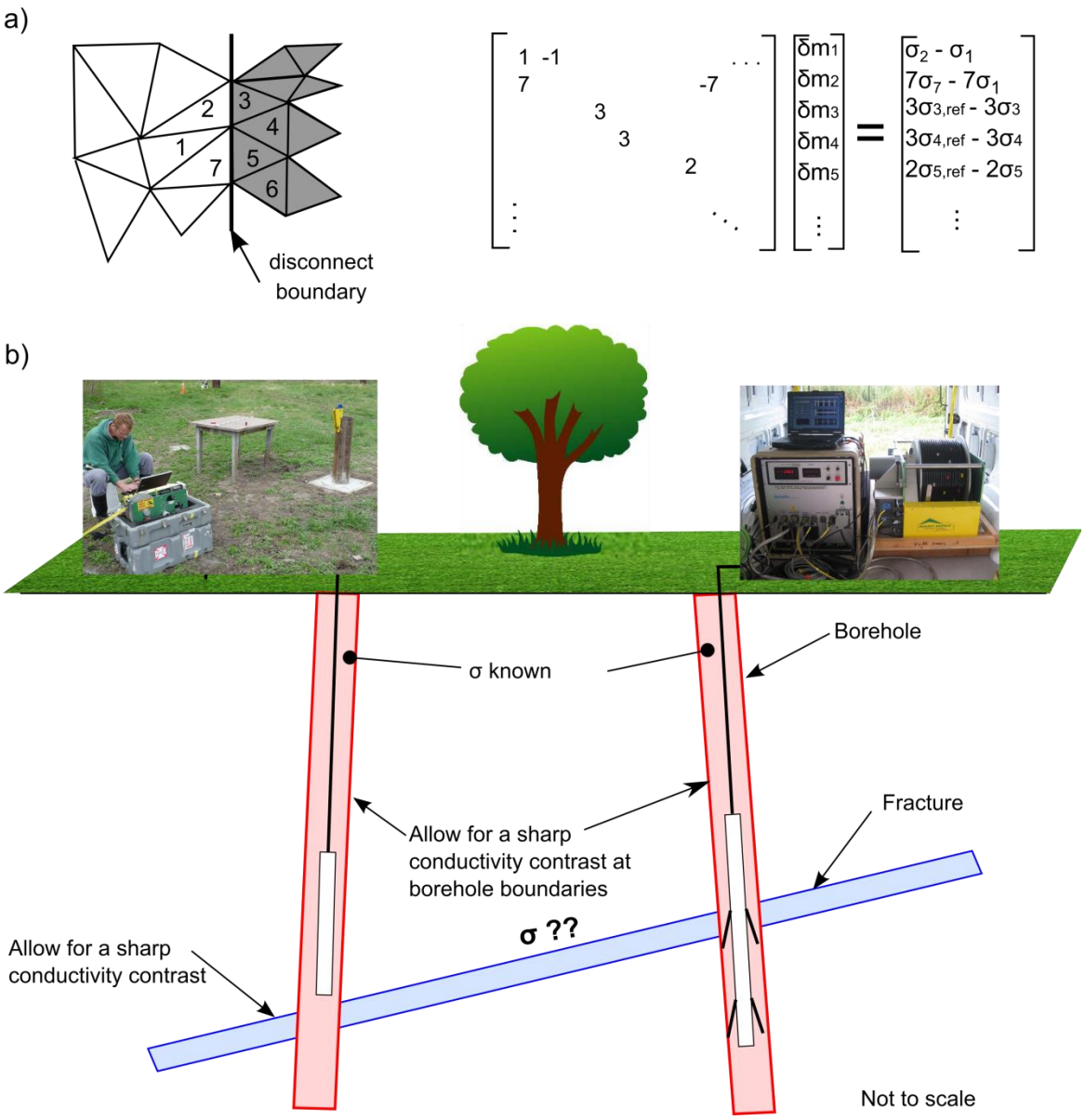

Figure 4.1: a) Conceptual mesh and associated formulation of regularization matrix W_m for smoothness constraints, localized de-regularization (i.e. a RD) and conductivity constraints (after Robinson et al, 2013) b) Definition of model constraints defined from borehole logging data and a continuity assumption for a fracture intersecting multiple boreholes.

SITE DESCRIPTION AND ORIGINAL 2D ERT MEASUREMENTS

The study site for this investigation is Middlebarrow quarry, a Carboniferous limestone quarry located in northwestern England (Figure 4.2). The site was operational in the

1990's when ERT (Slater et al., 1996; Slater et al., 1997) and hydrogeological (Brown & Slater, 1999) data were collected. The motivation for this study was to acquire better information on the continuity of a dominant fracture zone interval (bedding plane feature) known to exert a strong control on the local and regional hydrogeology of the site. The study was mandated as the quarry operators were applying for permission to excavate to approximately 6 m below the potentiometric surface and proposing to maintain quarry conditions by continually pumping the excavated region. Concerns were expressed regarding the effect of this long-term pumping on the local hydrogeology. The quarry is only 3 km from the coastline, and a UK Site of Special Scientific Interest (SSSI), designated based on its unique ecology, is only 1 km away from the quarry. The main concerns were related to the potential for water table drawdown at the SSSI and the invasion of saline water, possibly encouraged by the enhanced connectivity between the quarry and coastal locations resulting from continuity of the bedding plane feature between the quarry and the coast.

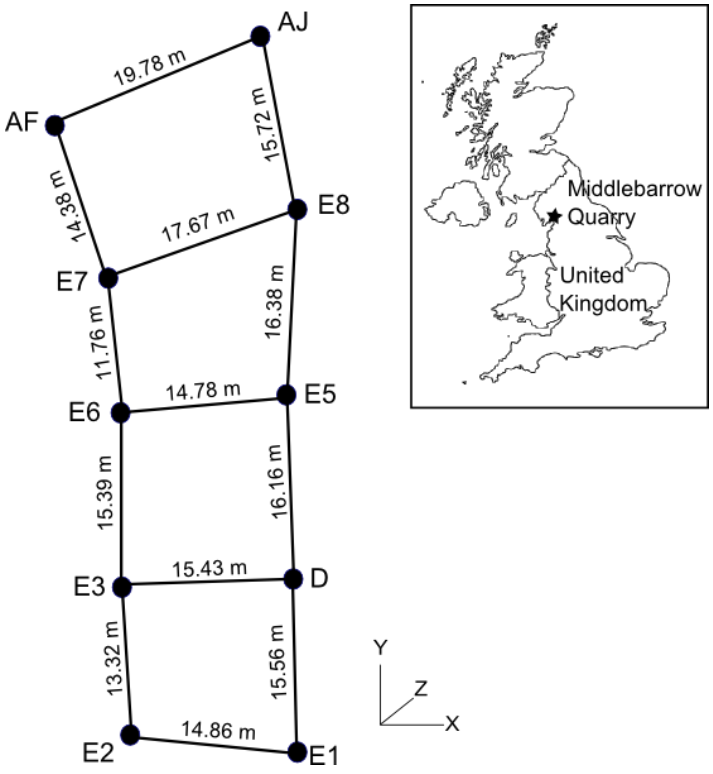

Figure 4.2: Strike panel with inset of study area (modified from

Data acquisition focused on 2D panels collected on a grid of nineteen 10 cm (4-inch) boreholes drilled at the site. Borehole deviations were not recorded. Figure 4.2 shows a subset of these boreholes known as the strike panel as they follow the strike of the bedding plane feature dipping at 12º toward the east. Each borehole was drilled as an uncased hole to an approximate depth of 25 m below the quarry floor. BHTV observations were made in each hole to identify the depth at which bedding plane feature(s) intersected the boreholes. Fracture apertures recorded with BHTV ranged between 5 and 10 cm. Double-packer tests were performed whereby a 1.7 m section was sealed down-hole to isolate successive sections of the borehole. The transmissivities of fractures were determined from the Barker (1981) equation for radial flow in a fissure conditioned on Rorabaugh (1953) and Barker (1981) correction techniques for turbulent

flow as shown in Table 4.1 (Brown & Slater, 1999). Horizontal and vertical hydraulic conductivities for the matrix were estimated as $1.1x10^{-7}$ m/s and $2.0x10^{-8}$ m/s, respectively (Brown & Slater, 1999), compared to an average fracture transmissivity of 0.07 m^2/s, illustrating the strong control of the fractures on groundwater flow.

Table 4.1: Transmissivities from focused packer testing*

Borehole	T (m^2/s)
E3 (@15.2 m)	0.075 ± 10%
E3 (@17.5 m)	0.080 ± 10%
E5	0.017 ± 6%
E6	0.045 ± 7%
E7	0.089 ± 8%
E8	0.093 ± 8%

*from Brown and Slater (1999); using Rorabaugh (1953) turbulent flow correction

ERT data were acquired with a single channel multi-electrode ERT system (Geopulse, originally produced by Campus Geophysics, UK). Each borehole contained 20 electrodes spaced 1 m apart; 740 independent measurements per panel were collected. Partial collapse of boreholes E1, E2 and E3 (Figure 4.2) limited the top electrode depths of these ERT arrays to 6.5 m, 3.72 m, and 6.5 m, respectively, below land surface. All other borehole top electrodes were 8.5 m below land surface. ERT arrays were kept level during the surveys such that boreholes E1, E2 andE3 controlled the installation depths of the arrays within these boreholes. A cross-hole electrode configuration was used, whereby current electrode pairs (AB) straddled boreholes as did potential electrode pairs (MN). A full set of 740 forward and reciprocal measurements (defined by swapping current and potential dipoles) was acquired on each panel (LaBrecque et al., 1996). A total of 13 panels (9,620 measurements) were initially acquired to characterize the site (Figure 4.2). Eleven panels (8,140 measurements) were then repeated during a pumping test experiment, devised to examine the likely effect of drawdown on the local hydrology

and ecology. This test provided an opportunity to perform a time-lapse analysis of the changes in conductivity within the fracture zones caused by the invasion of more electrically conductive fluid associated with saline intrusion that resulted from pumping. A borehole conductivity probe located in a nearby borehole to the ERT boreholes was continuously logged during the ERT surveys. Average groundwater conductivity equal to 0.3 S/m was measured during the background ERT measurements; a threefold increase in average conductivity to 1.2 S/m resulted from the pumping test performed on the trial excavation.

METHODS

2.5D ERT INVERSION

A relatively coarse finite element mesh (FEM) discretization was used in the original 2.5D inversion of the 2D panel datasets (Slater et al., 1996; Slater et al., 1997) with just two mesh elements between each electrode. We re-inverted the original static and time-lapse panel datasets for the survey between boreholes E3 and E6 (Figure 4.2), selected because of the high conductivity contrast that matched well with the location of the bedding plane observed in BHTV data. Our new 2.5D inversion of the 2D datasets utilizes the original smoothness regularization between model parameters but differs from the original study in two ways: 1) a finer discretization was used whereby the spacing between vertical and horizontal quadrilateral mesh nodes was decreased by a half (i.e. four mesh elements between each electrode), resulting in mesh elements with a dimension of 0.26 m by 0.25 m in a central region (referred to later as the foreground region) extending 2 m beyond the boreholes; 2) a data error model based on Koestel et al, (2008) (described below) was used to better characterize data errors.

3D ERT INVERSION

An unstructured tetrahedral mesh generator, TetGen (Si, 2006) was used to discretize the region of the Earth represented by the strike panel into a 3D FEM. This mesh generator allows the creation of bounded regions to incorporate small scale features such as boreholes and fracture planes. To ensure a high quality mesh with no small, thin shaped elements, the maximum radius to edge ratio of the elements was set to 1.3. The discretization included 10 boreholes (Figure 4.3) assumed to be vertical, although deviations are likely. Each well contained 20 electrode locations. Larger mesh elements were used with increasing distance away from the borehole cluster outside of the perimeter. The model space expected to have the largest current densities is referred to here as the foreground region and was defined in the mesh by a perimeter extending 5 m beyond the center-borehole coordinates and to a depth of 40 m (refer to Figure 4.3). This discretization resulted in 679,306 tetrahedral elements.

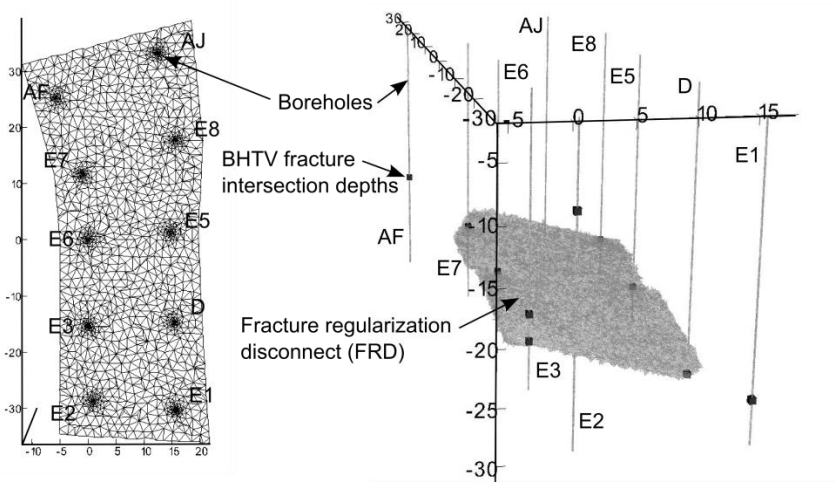

Figure 4.3: a) Plan view of mesh and b) discretization showing only boreholes and discretized fracture plane interpolated from BHTV fracture intersection depths. To reduce computation time, inversions that do not include the FRD use a mesh without the discretized fracture plane.

Bedding plane intersection depths identified in BHTV data were used to define planes that represent a continuous fracture in the discretization between and surrounding borehole locations (Figure 4.3b). This continuous fracture was used to define boundaries in the mesh where smoothness constraints are relaxed, referred to here as a fracture regularization disconnect (FRD). Specifically, the FRD region is a finely discretized volume in the model space representative of the assumed spatial location of a fracture. Fracture intersection depths aligned between boreholes E3, D, E5, E6, E7 and E8 and a continuous plane was defined here (Figure 4.3). Allowing for some ambiguity of the fracture locations in between the boreholes, fracture apertures were modeled as approximately 0.50 m or 1.0 m wide whereas actual fracture apertures are approximately 5-10 cm based on BHTV images. The maximum volume of each element within the FRD was set to 0.001 m^3. This discretization required 1,224,739 tetrahedral elements. Given the continuity assumption in creating the FRD (planar surfaces extrapolated from known bedding plane locations in boreholes), the potential clearly existed to mislocate this feature; the consequences of this important issue will be addressed later on.

To better represent the data standard deviations in the inversion modeling, a global error model similar to Koestel et al. (2008) was computed. The combined background (characterization) dataset (without reciprocals) for 13 panels contained 4,810 measurements. Measurements with a reciprocal error less than 5% (4,657 measurements) were sorted by the absolute value of the resistance measurements and separated into twelve bins with an equal number of measurements. The resistances and reciprocal errors were then averaged for each group and the best line fit was found by using a power law fit to these twelve data points of the form:

$$RE_{bin} = aR_{N/R}^{b}, \quad (4.5)$$

where RE_{bin} (Ω) is the binned averaged resistance error of the resistance measurement, $R_{N/R}$ (Ω) is the averaged reciprocal measurement for each bin, and *a* and *b* are fitting parameters. For the 13 panels, *a*=0.131 and *b*=0.48 with a linear correlation coefficient (R^2) = 0.93 (Figure 4.4a).

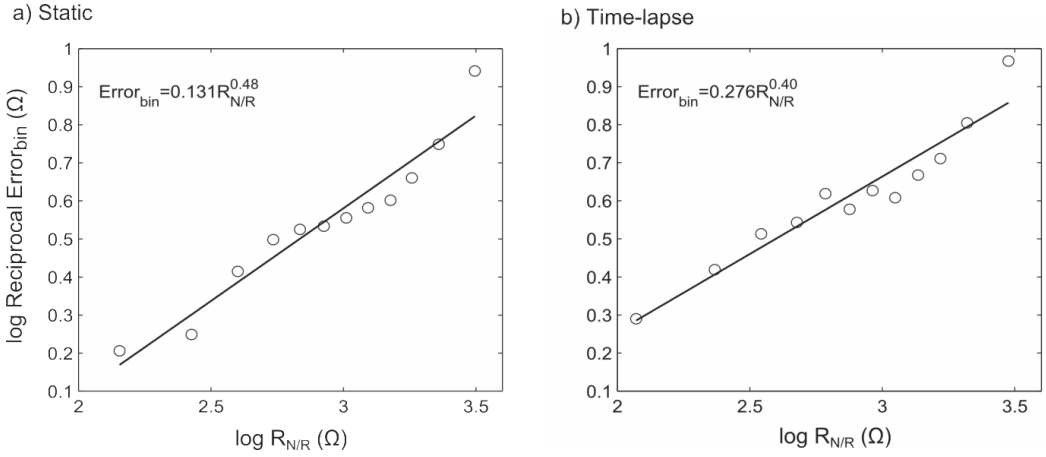

Figure 4. 4: Resistance measurement reciprocal error models for field data: a) static/characterization error model for 13 ERT panels b) time-lapse error model for 22 ERT panels.

These fitting parameters were used in Equation (4.5) to calculate individual standard deviations for each measurement. Data errors were very low, thus we found numerical modeling errors contributed substantially to the ability of the inversion to fit the data to χ^2=1. To maintain the relative weighting between the data points, a scale factor of 15 was applied to standard deviations calculated from Equation (4.5) (Koestel et al., 2008), which includes a maximum forward modeling error of 4.5%. Background and time-lapse datasets for 11 ERT panels were next combined (resulting in 22 background and time-lapse panels) and the error model re-examined. The total number of measurements without reciprocals for the 11 ERT panels was 8,140. After filtering reciprocals with less

than a 5% difference, the total number of measurements was 7,440. Data errors were described by the fitting parameters a=0.276 and b=0.40 (R^2=0.92) (Figure 4.4b). The same scaling factor of 15 was used to adjust the data standard deviations.

The 3D inversions were performed using a modified version of the parallel code described by Johnson et al., (2010). This code permits RDs to be applied along completely disconnected FEM region boundaries. Borehole RDs (BRDs) and FRDs were used in the inversion modeling. While BRDs and FRDs are modeled in the same fashion, we consider it important to distinguish between these features. First, the location of the boreholes is well known, and removal of smoothness constraints across this boundary is justified. This confidence in the locality of the boreholes also facilitates incorporation of other borehole data, such as constraints on the electrical conductivity of the fluids from a specific conductance log, into the inversion. There is much greater uncertainty in assuming the location of a fracture zone to place an FRD between wells, even with the best available borehole logging data.

The FEM with the fracture discretization was only used where an FRD was applied (this is justified later through synthetic modeling). Within a FEM region, the inversion code allows specified tetrahedral elements to be constrained against a known conductivity, referred to here as a conductivity constraint. The average groundwater conductivity (0.3 S/m) was used as a conductivity constraint within the boreholes although we acknowledge the uncertainty in this assumption given borehole fluids were likely to be partially mixed as a result of the placement of the electrode arrays. The data were fit to a minimum χ^2 value of 1. As with RDs, conductivity constraints imposed on mesh elements do not fix parameter conductivity, but constrain against this value. The

resulting model must still be fit to the data for convergence. Figure 4.5 summarizes the different regularization strategies performed in this work.

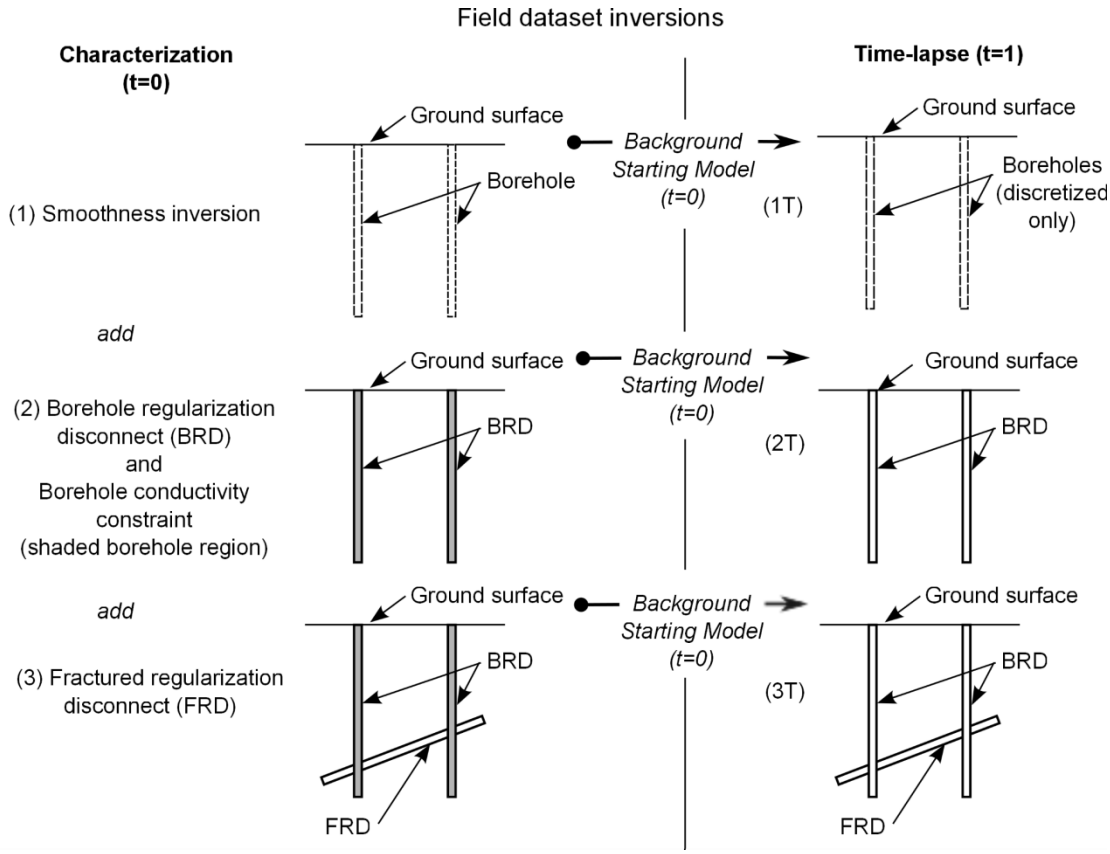

Figure 4.5: Summary schematic of regularization constraints used in field data inversions (1) – (3) performed in this study where a 'T' suffix represents a time-lapse inversion with a starting model equal to the inversion with the same prefix number.

The time-lapse inversions of changes in conductivity were performed using a modified version of the difference inversion method of Labrecque and Yang (2001) (Equations (4.3) and (4.4)). The modification is that the Jacobian matrix is updated at each Gauss-Newton iteration to ensure it is consistent with the conductivity distribution predicted at each iteration. The background dataset in the time-lapse modeling is slightly different than the characterization dataset (i.e. 11 panels instead of 13 panels). Two-dimensional ERT time-lapse data were unavailable between boreholes E1-E2 and E2-E3. So that the background and time-lapse models have the same normalized χ^2 misfit error, the χ^2 for the

time-lapse inversion was set to converge at the background χ^2 value (i.e. usually slightly less than 1).

3D Inversions performed

Field Data

The combined 2D-panel ERT datasets were inverted in 3D to compare against results from 2.5D inversions and to examine the benefits of incorporating borehole specific conductance data and borehole locations on the characterization of fractures. *A priori* information was added in the form of RDs and conductivity constraints (Figure 4.5). To begin, a regularized smoothness inversion (1) was performed. A BRD was then placed along borehole boundaries and borehole conductivity constraints were added (2). Mesh elements representing boreholes were constrained to a value of 0.3 S/m, as justified above. In well-resolved regions, inversion results should be largely independent of the homogeneous starting model. Thus, different starting models were chosen and the models compared. The original study found background conductivities near $10^{-4.5}$ S/m and borehole fluid conductivities near 0.3 ($10^{-0.52}$) S/m; a starting model in the middle of these values, or 0.003 ($10^{-2.5}$) S/m was chosen as was a starting model closer to background conductivities, or 0.0003 ($10^{-3.5}$) S/m. The regularization constraints from (1) were used to solve for a background starting model for the time-lapse inversion (1T). Similarly, the regularization and borehole constraints applied in (2) were used to solve for a background starting model employed in the time-lapse inversion (2T). Borehole conductivity constraints were not used in the time-lapse inversion as the objective was to find model convergence on the data difference.

Next, FRDs were incorporated into the modeling, first in the static inversion (3). Using (3) as a background reference model, a time-lapse inversion (3T) was then performed (refer to Figure 4.5). As in inversions (1) and (2), two different starting models, 0.003 ($10^{-2.5}$) S/m and 0.0003 ($10^{-3.5}$) S/m were used to investigate sensitivity to the starting model. Note that the fracture zones are completely disconnected from the boreholes, so that the data alone must fit a high conductivity feature within the FRD; this avoids smearing of the borehole conductivity that may occur when smoothness constraints are permitted along the boreholes.

Synthetic Data

Synthetic models were designed to investigate inversion errors originating from mis-located boreholes. With this synthetic test, we ask the question, 'how do borehole effects distort ERT images when they are not appropriately discretized and/or constrained'? Table 4.2 summarizes the synthetic trials used to examine borehole effects. The configuration shown in Figure 4.2 was again used and the measurement sequence was the same as for the field datasets. The true model was assigned a background conductivity of 0.001 S/m whilst boreholes conductivities were set equal to 0.1 S/m. The true model contains a finely discretized region representative of a fracture plane with mesh element conductivities equal to that of the boreholes (i.e. 0.1 S/m). The measurement error model shown in Figure 4.4a was used to simulate measurement noise for the synthetic data. All synthetic inversions used a starting homogeneous model equal to 0.01 S/m. S1 is a smoothness inversion. In S2, RDs were placed at borehole locations along with borehole conductivity constraints. In order to investigate borehole mis-locations, borehole locations in S3 were offset by 1 m inside the borehole perimeter (refer to

Figures 4.2 and 4.3a). We acknowledge that borehole deviations can in some cases have magnitudes greater than 1 m. We chose to offset boreholes by this relatively small magnitude to illustrate the effects even where deviations are small.

Table 4.2: Synthetic Inversions: Borehole Effects

	True Model	Inversion (no fracture in discretization) Starting homogeneous model = 0.01 S/m		
		Borehole RD	Borehole Conductivity Constraint = 0.1 S/m	Offset boreholes by 1 m
S1	Host Rock = 10^{-3} S/m Boreholes = 10-1 S/m Fracture = 10-1 S/m			
S2		•	•	
S3		•	•	•

Synthetic trials were also used to further understand the effects of localized de-regularization and constraints on the ERT inversion in simulated fractured rock environments (Table 4.3). The objective was to examine changes in the resolved model due to the presence of a RD for 1) no modeled fracture, 2) a resistive fracture and 3) a conductive fracture using the same configuration (Figure 4.2) and field measurement sequence. In S4, the true model was

Table 4.3: Synthetic Inversions: Fracture regularization disconnects (FRD)

	True Model	Inversion regularization constraints		
		Borehole RD	FRD	Borehole Conductivity Constraint
S4a	Homogeneous = 10^{-1} S/m	•		0.1 S/m
S4b		•	•	0.1 S/m
S5	Host Rock = 10^{-1} S/m Boreholes = 10^{-3} S/m Fracture = 10^{-3} S/m	•	•	0.001 S/m
S6a*	Host Rock = 10^{-3} S/m	•	•	0.1 S/m
S6b*	Host Rock = 10^{-4} S/m	•	•	0.1 S/m
S6c*	Host Rock = 10^{-5} S/m	•	•	0.1 S/m

* Boreholes and fracture conductivity = 10^{-1} S/m

homogeneous (0.1 S/m), but the inversion mesh was discretized to include a finely

discretized region representative of a fracture. In S4a, smoothness constraints were enforced across the finely discretized region while in S4b, a RD was applied across this region. In S5, the boreholes and fracture were modeled as 2 orders of magnitude more resistive than the host rock; a FRD was included in the inversion. In S6, the boreholes and fracture were more conductive than the host rock in the true model. In S6a, S6b and S6c, the conductivity contrast between the host rock and the fractures/boreholes varied by 2, 3 and 4 orders of magnitude respectively. The starting homogeneous conductivity varied for each conductivity contrast and was chosen to be mid-way between borehole/fracture and background values.

To determine the effect of using the field data noise model, S4 inversions were run by adding both 2% random Gaussian noise and noise simulated from the measurement error model (Figure 4.4a). Inversions S5 and S6 included the addition of measurement noise simulated from the measurement error model (Figure 4.4a).

RESULTS

Field data

Panel images between boreholes E3-E6 are shown in Figure 4.6 where Figure 4.6a represents the 2.5D inversion of 2D panel data and Figure 4.6b is a 2D section of the 3D inversion described for (2) above (refer to Figure 4.5). This panel was chosen because images for this panel in Slater et al., (1997) and Slater et al., (1996) contained well-defined conductivity contrasts in both characterization and time-lapse images. We chose to compare the re-inverted data to (2) (Figure 4.5) to highlight the benefit of regularization constraints used here and detailed below. Figure 4.6a and 4.6b show a conductive region connecting the two boreholes. In Figure 4.6c and 4.6d a change in

conductivity occurs at approximately the same location, coinciding with the BHTV fracture intersection depths. However, the static image from 2.5D inversion (Figure 4.6a) contains borehole artifacts while the 3D inversion (Figure 4.6b) contains fewer artifacts surrounding the boreholes. The depth to the top electrodes in boreholes E3 and E6 was 6.5 m below land surface. Therefore, near-surface inversion artifacts in Figure 4.6a could be associated with the 2.5D approximation of the 3D borehole or poorly resolved regions of the model space. Figures 4.6c and 4.6d show 2.5D and 3D time-lapse inversion results displayed as a conductivity change from the background time. Conductivity changes within the host rock and boreholes are more focused in the 3D image (Figure 4.6d) than from the 2.5D inversion (Figure 4.6c). The 2.5D inversions (Figure 4.6c) contains several muted artifacts near borehole E6 at depths of 0 and 20 m while the 3D inversion shows conductivity changes contained within the borehole boundaries.

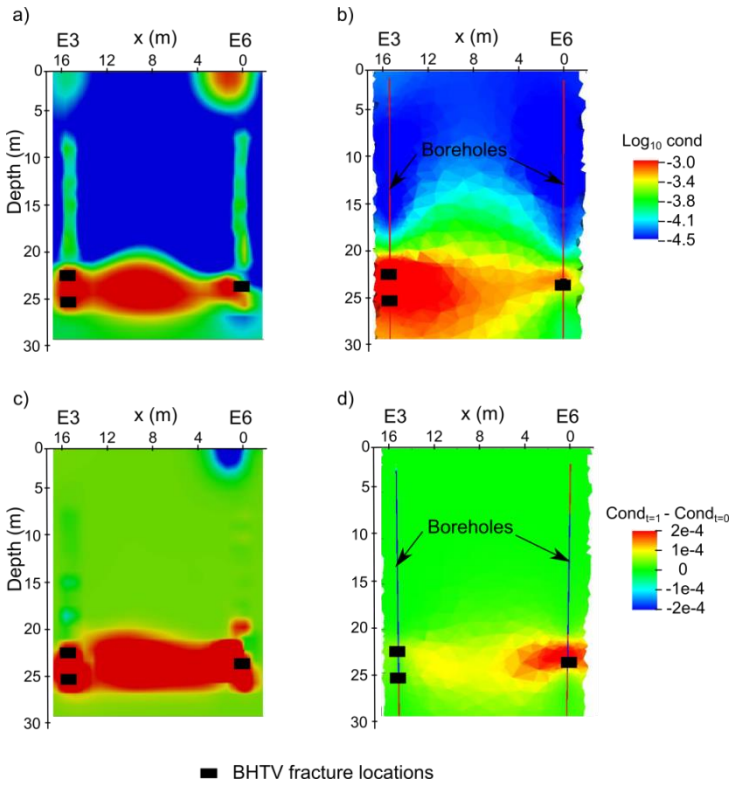

Figure 4.6: 2.5D inversion of 2D data of static a) and time-lapse c) inversions compared to 3D static b) and time-lapse d) inversions from (2) and (2T) described in Figure 4.5.

The 3D conductivity iso-contour plots for (1), (1T), (2) and (2T) are plotted in Figure 4.7. Figures 4.7a, 4.7c, 4.7e and 4.7g used a starting model equal to 0.003 S/m; Figures 4.7b, 4.7d, 4.7f and 4.7h used a starting model equal to 0.0003 S/m. Inversion images with the two starting models are shown to compare with results below. The smoothness inversion (1) (Figures 4.7a and 4.7b) delineates a high conductivity near E3 in the direction of E6. Many of the boreholes (i.e. E1, E2, E3, E6 and E7 visible in Figure 4.7) have a high conductivity halo. With the addition of borehole RDs and borehole conductivity constraints (2) (Figures 4.7c and 4.7d), these high conductivity halos are reduced; however low conductivity artifacts now surround several boreholes (visible are E2, E3 and E6) and matrix conductivities appear lower than in Figures 4.7a and 4.7b.

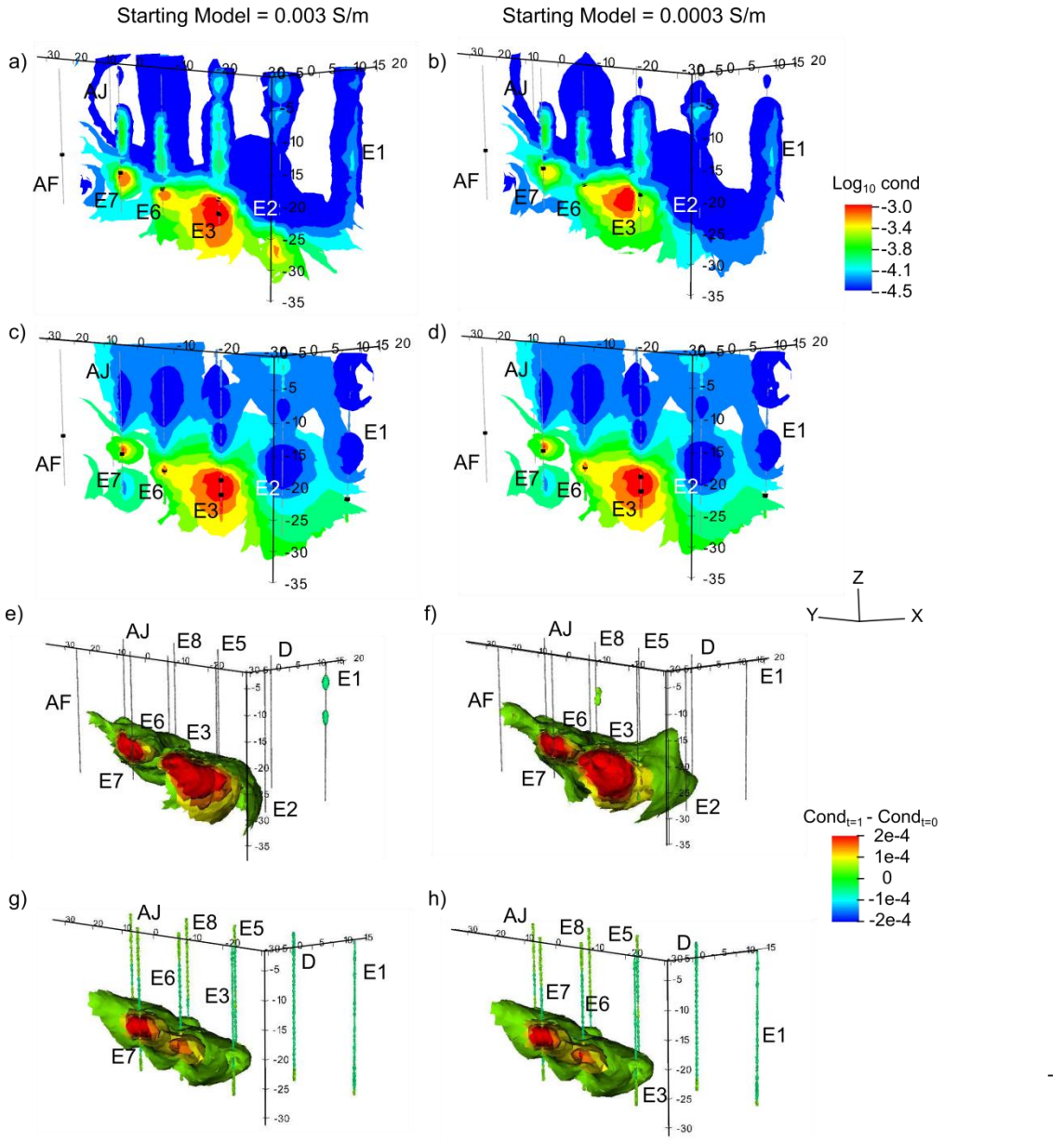

Figure 4.7: 3D iso-contour side view of static/characterization (a-d) and time-lapse (f-h) inversions for homogeneous starting models of 0.003 S/m (a, c, e and g) and 0.0003 S/m (b, d, f, h) . In a) and b): smoothness inversion images (1). In c) and d): borehole RDs and borehole conductivity constraints (2). BHTV intersection depths are shown as black boxes in a-d. In e) and f): time-lapse images using a smoothness-constrained background inversion (1T); discretized boreholes are shown for reference only. In g) and h): time-lapse images where borehole RDs and borehole conductivity constraints are used in the background model (2T). The smallest contour shown in time-lapse inversions in (e-h) is 5e10-5 S/m.

In the time-lapse inversion (1T), the largest changes in conductivity are focused near boreholes E3, E6, E7 and E8 (Figures 4.7e and 4.7f) with the change extending both laterally and vertically, which is physically unrealistic assuming that the primary porosity of the rock matrix is insignificant in contributing to fluid flow. In the time-lapse inversion (2T), the largest change in conductivity surrounds E7, extending to E3, E6, E8 and appears more focused laterally (Figures 4.7g and 4.7h). The higher transmissivities in Table 1 for boreholes E3, E5, E6, E7 and E8 coincide with locations of higher conductivities in Figures 4.7g and 4.7h. Regardless of the value of the homogeneous starting model, the conductivity distributions in Figure 4.7 are consistent, both in lateral and vertical spatial range and structure.

The addition of a FRD in (3) (Figures 4.8a and 4.8b) visually suggests much improved delineation of a high conductivity feature; however this inverted conductivity distribution depends on the starting model, suggesting either low model sensitivity to the data or non-uniqueness of the recovered model in this region. Time-lapse inversion images for 3T (Figures 4.8c and 4.8d) also show a dependence on the starting model. Figure 4.9 is a boxplot of logarithmic conductivities within the FRD with the starting model conductivity shown along the x-axis and within the plot as a green line. The median for each inverted conductivity distribution within the FRD region is indicated by the center box horizontal line and the inter-quartile range (i.e. the first and third quartiles) are shown at the edges of the box. The solid line extension represents 1.5 times the inter-quartile range; any values beyond this range are plotted as individual points and represent outliers. The boxplot reveals poor recovery of the true fracture conductivity; median FRD conductivities do not deviate by even half an order of magnitude from the starting

models when starting models are varied over two orders of magnitude from 0.003 ($10^{-2.5}$) S/m to 0.00003 ($10^{-4.5}$) S/m.

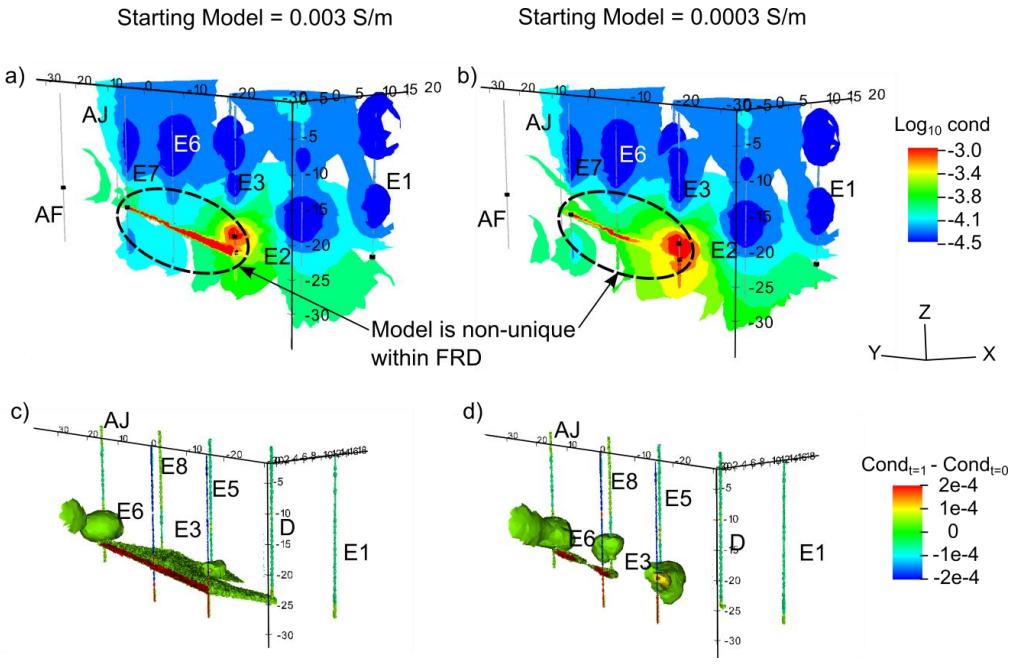

Figure 4.8: Adding a FRD in the static (a-b) (3) and time-lapse (c-d) (3T) inversions focuses the contrast and change in conductivity but is dependent on the homogenous starting model (0.003 S/m in a and c; 0.0003 S/m in b and d). BHTV intersection depths are shown as black boxes in a) and b). The smallest contour shown in c) and d) is 5e10-5 S/m.

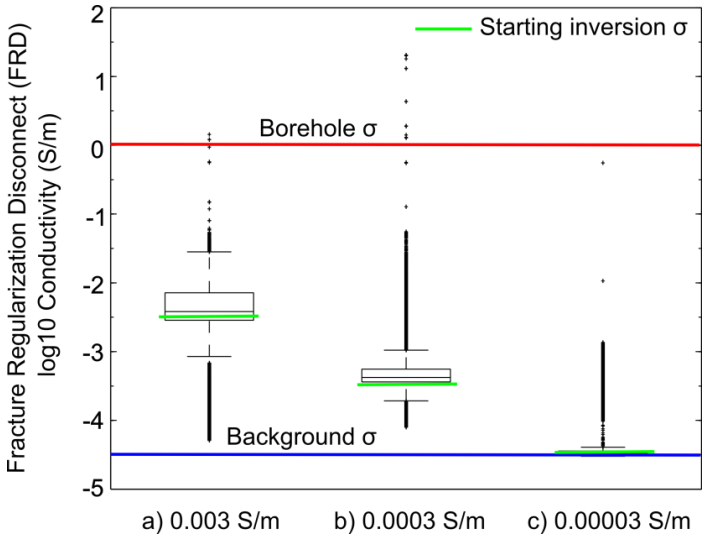

Figure 4.9: Logarithmic FRD conductivity distribution for field data inversion (5) with different homogeneous starting models: a) 0.003 S/m (Log10=-2.5) b) 0.0003 S/m (Log10=-3.5) and c) 0.00003 S/m (Log10=-4.5). In all three models, the median FRD conductivity is near the starting model value with the range of conductivities decreasing as the starting model is further from the actual borehole conductivity.

Synthetic Data

The results from S1 – S3 (refer to Table 2) are displayed in Figure 4.10. Borehole artifacts are evident surrounding borehole locations in the smoothness inversion (Figure 4.10b). When borehole RDs are applied along borehole boundaries and a borehole conductivity constraint is applied, borehole artifacts are reduced (Figure 4.10c) and matrix conductivities match better with the true model (Figure 4.10a). Offsetting actual borehole locations by 1 m (S3) results in the return of borehole artifacts (Figure 4.10d) which mimics the borehole effects seen in the field dataset (Figures 4.7c and 4.7d). Thus, we find that the answer to the question posed by our synthetic test is that boreholes which are not appropriately discretized and constrained cause a low conductivity halo effect. This emphasizes the importance of accurate location of electrodes in boreholes (Oldenborger et al., 2005).

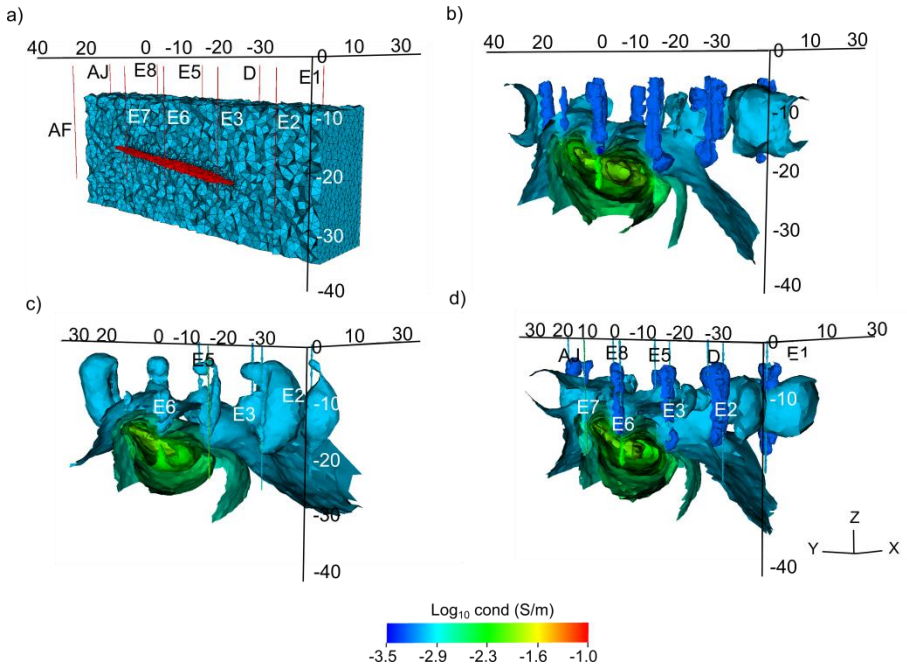

Figure 4.10: Synthetic simulations which show borehole artifacts can be greatly reduced with correct modeling of borehole locations and using borehole conductivity data as a constraint in the inversion; a) Conductivity model is shown sliced at x=5 m with mesh discretization and fracture location. b) Smoothness inversion (S1) shows the introduction of borehole artifacts c) Adding borehole conductivity data and removing smoothness constraints along borehole boundaries (S2) significantly reduces borehole artifacts d) Offsetting the boreholes by 1 m (S3) re-introduces the borehole artifacts. For better viewing, light shadowing of isocontours is displayed.

The inversion correctly resolves the conductivity within a finely discretized region in the case of a homogeneous synthetic model for a smoothness inversion (S4a, Figure 4.11a and 4.11b), although with the 2% random Gaussian noise (Figure 4.11a) the inversion resolves closer to the true model conductivity than when using the field data noise model (Figure 4.11b). However, when a RD is applied along the finely discretized region (S4b), the inversion solves for lower conductivities within this region than the true value when using both data error models (Figures 4.11c and 4.11d). The 2% noise model (Figure 4.11c) resolves the finely discretized region closer to the true (homogeneous) model value than the field data error model (Figure 4.11d). The median FRD conductivity is closer to the starting model than the true conductivity (Figures 4.11c and 4.11d).

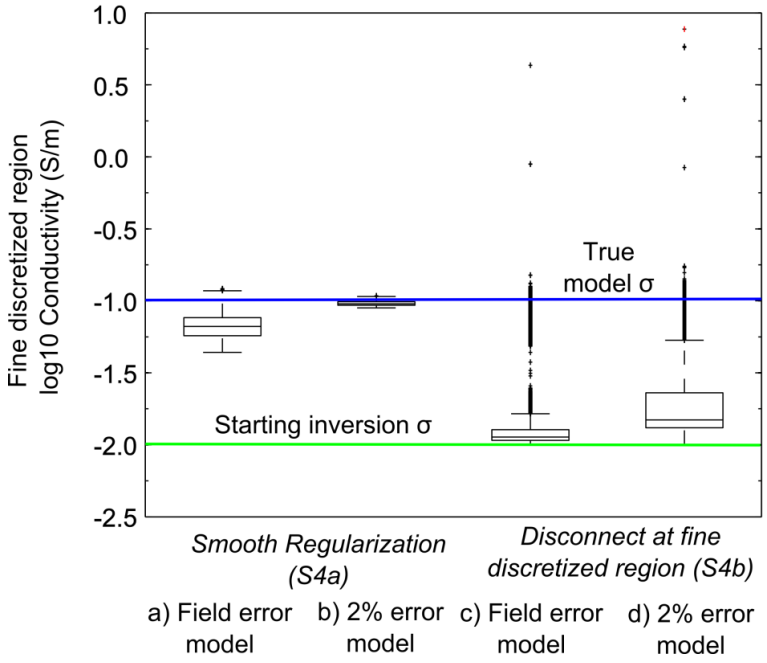

Figure 4.11: Boxplot conductivity distributions within a finely discretized region for synthetic inversions S4a, S4b for a homogeneous model. Smooth regularization for S4a is shown where a) has a field data error model and b) has a 2% data error model to weight the data in the inversion. A regularization disconnect is applied at the finely discretized region for S4b where c) has a field error model and d) has a 2% data error model to weight the data in the inversion. In all cases the boreholes are constrained against the actual borehole conductivity.

When the true model contains resistive boreholes and fractures (S5), the inversion (Figure 4.12a) resolves the conductivities within the FRD as over one order of magnitude higher than actual values and is close to the starting model value. Figure 4.12a suggests that the inversion cannot accurately resolve fractures for a resistive FRD (i.e. which would be the case for an air-filled fracture zone).

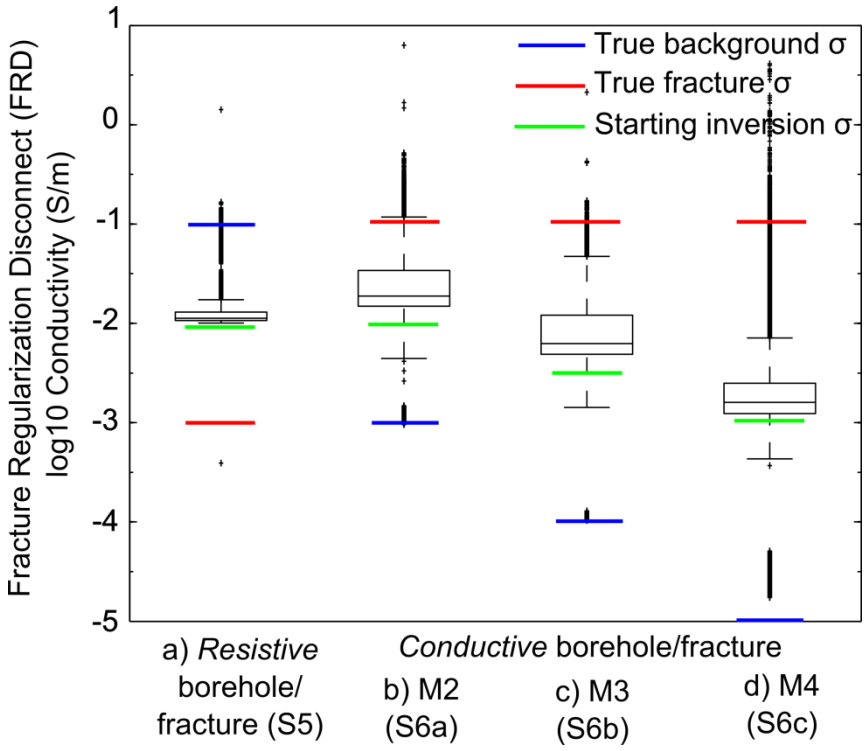

Figure 4.12: Boxplot conductivity distributions within FRD for synthetic inversions S5, S6a, S6b and S6c. In a) boreholes and fractures are more resistive than the host rock. In b-d conductive boreholes and fractures have an order of magnitude contrast with the host rock of 2, 3 and 4, respectively. Starting models were chosen to be in between the background and fracture/borehole conductivities. In all cases the boreholes are constrained against the actual borehole conductivity.

Results for S6a, S6b and S6c (refer to Table 4.3) show the inversion (Figure 4.12b, 4.12c and 4.12d) resolves conductivities higher than the starting model, with individual outlier points trending toward the fracture conductivity. The recovery of true fracture conductivities worsens as the contrast between the fracture and host rock increases i.e. from 2 orders of magnitude (M2) to 4 orders of magnitude (M4).

DISCUSSION

We have demonstrated how a 3D ERT inversion constrained by borehole logging information has potential for improving characterization and monitoring of fractured rock systems. Imaging in 3D and applying appropriate constraints is clearly a necessary step to advance the usage of ERT in fractured rock to better account for strong effect of

boreholes, and to model fracture zones. However, we show how de-regularization of discrete zones can result in spurious electrical structures. The 3D modeling performed here permits incorporation of boreholes in the model, defined by a boundary between the borehole and rock, and a constraint on the borehole conductivities. By adding 1) regularization constraints in the form of borehole RDs and 2) borehole conductivity constraints, in a 3D inversion, we find better spatial resolution of boreholes and fracture bedding plane features when compared to an original study based on 2.5D smoothness inversion of individual panels of data (Figure 4.6 and 4.7).

Within the 3D inversion, we find that the BRDs are necessary for convergence in the inversion when using a hard borehole conductivity constraint (not shown for brevity), however this may be specific to this environment with a large conductivity contrast of 4 orders between the boreholes and host rock. Here we find the 3D inversion gives a more complete view of the interconnectivity of this fractured rock system as shown by iso-contour images although we acknowledge there are additional complexities regarding this direct comparison, such as the discretization and regularization applied. However, the 3D inversion generally suggests that if limitations precluded the collection of true 3D datasets, a 3D inversion of multiple 2D datasets provides a more informative spatial interpretation relative to 2.5D inversion of independent panels.

Accurate location of boreholes (i.e. electrodes) is important in resistivity imaging of fractured rock. We showed synthetically that, borehole artifacts are reduced when including borehole conductivity constraints and borehole RDs. However, artifacts are reintroduced when borehole deviations are inaccurate; field inversions where deviations are not accounted for exhibit the same behavior as was shown synthetically. More

studies would need to be conducted to determine the effect of borehole deviations on a) a more complex fracture network b) a lower matrix/fracture conductivity contrast. However it is clear that correct location of electrodes in boreholes is important for accurately modeling ERT data in fractured rock settings.

Relaxing smoothness regularization constraints is a requirement if fractured rock settings are to be more correctly represented in inverse model parameterizations. The application of regularization constraints at discrete bedding plane-like features defined from borehole logging data was largely unsuccessful for this dataset and constraints implemented, even without consideration of the potential for misplacement of the FRD. Adding a FRD (Figure 4.8) provides a regularization constraint that is geologically more representative of a discrete fracture. However, we showed that the FRD does not provide enough information to resolve the fracture by varying the homogenous starting model by a factor of 10 and examining the conductivities within the FRD. Robinson et al., (2013) performed synthetic studies that showed that misplacement of an FRD can result in anomalous conductivities within the FRD region. Our findings from the inversion of this field dataset (and supporting synthetics) further demonstrate that adding RDs can produce severe inversion artifacts. While it is often tempting (and increasingly practiced) to constrain ERT inversion with RDs defined from other available field data, uncertainty in the location of the FRD should be carefully examined in terms of regularization artifacts in the resulting images.

Given the model non-uniqueness within the FRD region for this field dataset, it was important to evaluate under what conditions the conductivity distribution of a localized fracture zone could be resolved. Clearly, the model non-uniqueness combined with the

inclusion of a RD for a homogeneous model (Figure 4.11c and 4.11d) introduces inversion artifacts within the finely discretized RD region. The inclusion of the finely discretized region is not the controlling variable here, since when smoothness constraints are enforced between this region and the background values, the conductivity distribution within the finely discretized region is close to the true model value (Figures 4.11a and 4.11b). We also find that, due to the model non-uniqueness, misplacing an FRD (not shown for brevity) results in an image where a feature within the FRD has a sharp conductivity contrast with the host rock, thereby adding another layer of complexity in implementing FRDs.

The noise models applied to synthetic measurement data were shown to affect how well the inversion can resolve a homogeneous earth model in inversions with smoothness constraints and regularization disconnects. Correct noise estimates have been shown to be essential in ERT modeling (LaBrecque et al., 1996); however, we have shown that the structure of the noise model can directly impact the ability of the inversion to correctly resolve conductivities (Figure 4.11). It is important to characterize the measurement noise as well as possible, however it would be naïve to accept that any data and numerical error model completely captures combined errors that can limit the inverse model from reaching a solution.

We found that the ability to resolve the conductivity distribution within a discrete fracture is largely controlled by the resistivity contrast between the fractures and host rock. The fracture conductivities resolved in the FRD are closest to the true model when there is a conductive borehole/fracture; however the resolving capability of fracture conductivity in this case depends on the conductivity contrast between the host rock and the (conductive)

fracture. When the borehole/fracture and background conductivity differ by 2 orders of magnitude, fracture conductivities are resolved well. Coincidentally, this is the same contrast used for the synthetic study in Robinson et al., (2013). As the contrast increases, median conductivities within the FRD decrease below the actual fracture conductivities, although a large number of individual conductivities within the FRD trend in the direction of the true fracture value. The FRD is not sufficient to constrain the inversion to resolve the conductivities within this region uniquely.

While the synthetic results show a conductive bedding plane feature can be delineated, our field study reveals that a fracture continuity assumption implemented in the form of a linear interpolation of fracture intersection depths from borehole logs may not sufficiently characterize fractures. The limestone fractured rock system investigated here contained a well-connected bedding plane feature with a large conductivity contrast. Given the potential pitfalls of using a FRD in this apparently ideal case, the approach is likely to be of limited value in more complicated systems given similar constraints. While the FRD was shown not to provide enough information to the inversion to uniquely resolve fractures, further studies should focus on the benefit of adding additional conductivity inequality constraints to fracture and surrounding host rock regions, for example, to force the condition that the fracture is more conductive than the host rock.

Finally, this study merged 2D ERT datasets. It may be possible to extract additional information with a more fully comprehensive 3D ERT dataset (as shown in Wilkinson et al., 2006). Future planned studies could use fully 3D datasets to better characterize bedding plane features in fractured rock and monitor conductivity changes in these

bedding planes due to the injection of tracers and amendments designed to encourage biodegradation of contaminants.

CONCLUSIONS

Improvements in 3D ERT modeling of fractured rock results when accurately parameterizing small scale conductive boreholes and incorporating borehole regularization constraints based on regularization disconnects and known borehole conductivity from borehole logs. However, using borehole regularization constraints and borehole conductivity constraints with incorrect borehole locations can result in inversion artifacts. Applying regularization constraints on an assumed fracture location proved challenging as a result of the uncertainties in the field data and the non-uniqueness of the model within the fracture region. The ability of the inversion to resolve conductivities within a finely discretized region is influenced by the removal of smoothness constraints along this boundary, and the relatively small volume occupied by the region thus, de-regularization of localized features can result in artificial electrical conductivity features. Future field studies should use fully 3D measurement surveys while considering modeling and regularization alternatives in hopes of providing better resolution of fractures.

ACKNOWLEDGEMENTS

Funding for this project was provided by the U. S. Department of Defense (DOD) under the Environmental Security Technology Certification Program ER 201118 (L. Slater, PI). Inverse computations were performed on the Pacific Northwest National Laboratory Institutional Computing System (http://pic.pnnl.gov). We are grateful to Andrew Binley (Lancaster University) for providing the original Middlebarrow dataset and field notes for

re-evaluation of this work and for providing R2 for 2D re-inversion of this dataset. This manuscript was improved considerably thanks to detailed comments received from three anonymous reviewers.

CHAPTER 5: Imaging transport pathways in fractured rock using 3D time-lapse electrical resistivity tomography[3]

ABSTRACT

Major challenges exist in delineating bedrock fracture zones which result in abrupt changes in geological and hydrogeological properties over small distances. Borehole observations alone may not be sufficient to fully capture heterogeneity in these systems. Geophysical techniques offer the potential to image properties and processes in between these locations. We used three-dimensional (3D) cross borehole electrical resistivity tomography (ERT) in a unique experimental configuration designed to capture high-resolution flow and transport processes in a fractured mudstone contaminated by chlorinated solvents, primarily trichloroethylene (TCE). Conductive (sodium bromide) and resistive (deionized water) injections were monitored. Prototype electrode arrays with isolation packers and fluid sampling ports were designed to enable pulsed tracer injections to occur during simultaneous acquisition of ERT measurements. Fracture zone locations and hydraulic pathways inferred from drawdown data obtained from pumping tests on isolated intervals were compared with electrical conductivity distributions from ERT measurements. Background ERT images showed alternating conductive and resistive zones, consistent with alternating laminated and massive mudstone units at the site. Tracer evolution and migration was clearly revealed in time-lapse ERT images and supported by in situ borehole vertical apparent conductivity profiles collected during the

[3] This chapter was submitted January 12, 2015 as: Robinson, J., Slater, L., Johnson, T., Shapiro, A., Tiedeman, C., Ntlargiannis, D., Johnson, C., Day-Lewis, F., Lacombe, P., Imbrigiota, T., Lane, J., Imaging transport pathways in fractured rock using 3D time-lapse electrical resistivity tomography, *Groundwater*

`

pulsed tracer test. While water samples provided important local information at the extraction borehole, ERT delineated tracer migration over spatial scales capturing the primary hydrogeological heterogeneity controlling flow and transport. The fate of these tracer injections at this scale could not have been quantified using borehole logging and/or borehole sampling methods alone.

INTRODUCTION

There is an increasing need to characterize the hydraulic properties of fractured rock sites for purposes such as oil and gas development, geothermal reservoir efficiency/optimization, and to facilitate remediation of a growing number of contaminated sites worldwide. The dominant flow pathways in fractured rock are usually controlled by joints, fractures, shear zones, faults and other discontinuities such as vugs. These environments are often poorly understood hydrogeologically due to the complex interrelationships between stress, temperature, roughness and fracture geometry that affect hydraulic conductivity (Singhal & Gupta, 1999), in addition to flow paths that have hydraulic properties varying over orders of magnitude (Shapiro, 2010). Characterization of fractured rock aquifers is usually based on interpolation of sparse data points obtained from observations acquired in one or more boreholes. This approach often does not capture the hydraulic complexity of such environments, particularly over the spatial scales between boreholes that integrate the primary heterogeneity in the hydraulic properties controlling flow and transport. At contaminated fractured rock sites where remediation is attempted through amendment injections (Bradley et al., 2012; Sorenson, 2000), the spatial extent and migration of the amendments are likely to be poorly resolved from a limited number of discrete borehole observations (Benson & Yuhr,

1993). Fusing borehole data with geophysical imaging methods (Li & Oldenburg, 2000; Lines et al., 1988) that can provide information beyond borehole walls might result in a more effective characterization of the flow and transport characteristics of fractured rock.

Electrical resistivity tomography (ERT) is a candidate technique to achieve this goal as, (1) electrical current pathways closely mimic hydraulic pathways (a valid approximation when ionic current flow is the dominant mode of conduction), and (2) the imaged volume and resolution can be adjusted through survey design. ERT permits the imaging of temporal changes in electrical conductivity for a volume of fractured rock mass bounded by boreholes. Compared to point measurements collected at discrete locations within boreholes, ERT can provide information at a spatial scale that can more readily capture the heterogeneity that controls flow and transport in fractured rock. Furthermore, whereas drawing fluid samples from boreholes for analysis can disturb the natural flow regime, ERT requires no further alteration to the natural system once electrodes are installed. This may be especially important when trying to understand ambient flow in fractured rock where the complex fracture connectivity may inhibit the placement of the most effective pore fluid monitoring locations (Shapiro, 2010).

To explain mass transport in fractured rock, hydrogeologic models have been proposed which consider advective-dispersive transport in the mobile domain (the fractures, also denoted the secondary porosity) and mass transfer into and out of the immobile domain (the matrix, or primary porosity) (e.g. Dentz & Berkowitz, 2003). While conventional sampling methods rely on drawing samples that only provide information on the concentration properties for the mobile domain, ERT is sensitive to bulk electrical conductivity that depends on the chemical composition of the pore fluids

in both the immobile and mobile domains. Several recent studies have shown that rate-limited mass transfer between mobile and immobile porosity has an observable geoelectrical signature (Briggs et al., 2014; Briggs et al., 2013; Day-Lewis & Singha, 2008; Singha et al., 2007). In fractured rock where tracer studies tend to have rapid breakthrough followed by extended tailing (Becker & Shapiro, 2000), long-term ERT monitoring therefore might provide insights into concentration changes over time within both the immobile and mobile domains due to matrix diffusion and heterogeneity.

There have been relatively few ERT studies in fractured rock and the hydrogeological information extracted has been limited for a number of reasons, including, (1) the until-recent lack of 3D data acquisition and processing techniques which can capture the complex electrical resistivity expected in fractured rock, (2) the use of conceptually inappropriate constraints on the model structure which often results in smooth resistivity distributions (deGroot-Hedlin & Constable, 1990) unrepresentative of fractured rock systems, and (3) distances between boreholes that were sub-optimal for an ERT study designed to provide information at the spatial scales capturing the primary heterogeneity controlling flow and transport. Surface ERT studies have been used to delineate subsurface conductivity changes in fractured rock to infer flow paths (Nimmer et al., 2007; Robert et al., 2012) but the resolution is inherently limited when only surface electrodes are utilized. Slater et al., (1997) used a natural tracer to better image (relative to static ERT studies) discrete fractures in an early two-dimensional (2D) cross borehole ERT study. Day-Lewis et al. (2004) showed the value of time-lapse cross borehole radar monitoring of tracer injections to construct and calibrate flow and transport models, but

ERT has clear advantages over radar for automation and 3D imaging. More recent studies on the application of ERT in fractured rock are lacking.

Scalable, parallel ERT algorithms are now available that allow 3D inversion of very large datasets with finely discretized unstructured meshes containing millions of elements using distributed memory supercomputers (Johnson et al., 2010; see also https://e4d.pnnl.gov). Such discretizations are necessary to correctly model the effects of boreholes (Doetsch et al., 2010), being a particularly important consideration in fractured rock where the contrast between the electrically conductive borehole and the rock matrix can be very large. Scalable algorithms permit fine discretization in regions, such as fractures, that exert a strong influence on electrical conductivity, groundwater flow and solute transport. New algorithms also allow for sharp conductivity boundaries. Robinson et al., (2013) suggest that allowing for sharp contrasts in conductivity at borehole locations and fracture zone locations inferred from borehole logs may aid in the derivation of hydrogeologically plausible resistivity models when applying ERT in fractured rock. Accurate modeling of borehole deviations is also important in order to eliminate systematic errors in the inversion that can occur if boreholes are simply assumed to be vertical (Oldenborger et al., 2005; Wilkinson et al., 2008).

The need for packers to hydraulically isolate intervals of a borehole for hydraulic testing and to remove the effect of flow and storage in the borehole is well recognized in hydrogeological studies (Becker & Shapiro, 2000; Berkowitz, 2002; Brown & Slater, 1999; Tiedeman et al., 2010). In ERT, a fluid-filled borehole similarly introduces a highly electrically conductive pathway (assuming the rock is relatively resistive) for current to channel between two injection electrodes (Binley & Kemna, 2005; Coscia et

al., 2011; Doetsch et al., 2010; Sugimoto, 1999), thereby reducing current penetration into the surrounding rock (Robinson et al., 2013). A few ERT studies have explored the use of packers (Labrecque & Yang, 2001) or rubber disks (Coscia et al., 2011) in down-hole arrays in an attempt to isolate electrodes and thereby limit the borehole current-channeling effect. However, these studies did not evaluate the effectiveness and/or merit of such packers in the imaging.

This study was designed to demonstrate the value of ERT imaging of fractured rock beyond the vicinity of boreholes using a unique survey design with a dense array of dedicated boreholes. Focusing on data acquisition and processing strategies relevant in fractured rock, we demonstrate extraction of spatiotemporal hydrogeological information that could not be reliably inferred using standard methods alone. ERT has potential to provide 3D time-lapse volumes of electrical conductivity, which can be interpreted as a proxy for concentration of a conductive tracer. Using information from preliminary tracer tests involving limited water sampling alone, we performed a pulsed-injection tracer test that successfully captures conductivity changes describing the flow and transport characteristics of the system. We also introduce a novel electrode array design which simultaneously enables fracture zones to be targeted with a tracer injection, limits current channeling along boreholes during ERT data acquisition and allows for water sampling from surrounding boreholes. These advances allow us to map field-scale tracer migration in 3D at a resolution heretofore intractable.

BACKGROUND

Electrical Resistivity

Electrical resistivity (ρ) or its inverse electrical conductivity (σ) is a physical property of the subsurface that measures how strongly a material opposes the flow of an electric current. A current (I) is injected into the earth via transmitting electrodes and a potential difference (ΔV) is measured across two receiving electrodes. Large sequences of electrical measurements are collected to sample the subsurface volume of interest at the desired spatial scale. Apparent resistivity (Ωm) or its inverse, apparent conductivity (S/m), can be calculated from the raw data based on the resistance measured (i.e. V/I), the geometry of the electrodes and an assumption of material homogeneity. In vertical borehole profiling, these measurements can be used to estimate vertical conductivity variations along boreholes with minimal data processing. In contrast, cross-borehole ERT resistivity measurements must be inverted to solve for conductivity distributions in 3D space.

The strengths and weaknesses of traditional electrical resistivity configurations (i.e. Wenner, Schlumberger, dipole-dipole) for acquiring ERT data are well documented (e.g. Furman et al., 2003; Binley & Kemna, 2005). The choice of measurement sequence in regards to information content in the resulting images is critical for any ERT study. Large survey times required to collect comprehensive 3D datasets are usually impractical, especially when attempting to capture transient processes such as tracer movement in fractured rock where ERT images are temporally smeared due to the finite data acquisition time, thereby emphasizing the need for shorter survey times. For N electrodes, a total of $N(N-1)(N-2)(N-3)/8$ four-point electrode configurations exist.

Given the enormous number of possible configurations, selection and collection of a subset of the possible measurements is necessary. Stummer et al.,(2004) proposed a methodology to create an optimized measurement sequence whereby measurements are added to an initial base dataset provided there is an improvement in image resolution. The computational demand involved is extensive and thus other researchers have optimized and/or modified this approach on 2D surveys alone (Loke et al., 2010; Wilkinson, et al., 2006).

Data errors are necessary to weight the relative importance of the individual data points on the inverse solution and appropriate characterization of ERT data errors should limit the artifacts in inversion images (Binley & Kemna, 2005). By differencing reciprocal measurements, whereby the transmitting and receiving electrodes are reversed, field data quality can be accessed and quantified as a reciprocal error (Slater et al., 2000). Where data quality is high (i.e. data errors are less than or within the range of numerical solution accuracy), numerical errors can dominate the ability of the inversion to converge to a solution. Thus, both data quality and numerical solution accuracy must be considered (e.g. Mwakanyamale et al. 2012) when assigning data errors in the inversion.

Inversion of ERT data is inherently non-unique such that a regularized inverse problem is typically formulated. The objective function involves minimization of two terms: (1) the weighted data misfit between predicted and actual resistance measurements and (2) a measure of model complexity (i.e. structure) whereby model constraints can be imposed. The tradeoff between the two terms is controlled by a regularization coefficient. Typically, smoothness constraints are imposed in the model structure between adjacent model parameters. However, this may not provide a good

representation of fractured rock, which is a heterogeneous system where sharp conductivity contrasts exist (e.g. between boreholes, fractured zones and unfractured rock). Recently developed codes allow for sharp conductivity contrasts between discretized regions and conductivity constraints to be applied where external data are available (Johnson et al., 2010). Robinson et al., (2013) used these code advances to demonstrate improved recovery of fracture zones in a synthetic study.

Time-lapse ERT datasets can be used to monitor conductivity changes resulting from natural hydrological processes (Henderson et al., 2010; Johnson et al., 2012; Meyerhoff et al., 2014; Robinson et al., 2012; Slater et al., 1997; Wallin et al., 2013), the injection of tracers (Perri et al., 2012; Slater et al., 2002) and/or the progress of amendments used for remediation purposes (Daily & Ramirez, 1995; Johnson et al., 2014; Oldenborger et al., 2007). Independent data inversions can be subtracted to highlight where changes in conductivity are occurring. However it can be beneficial to include initial model structure from a background model into time-lapse inversions. Subsequent datasets can then be inverted relative to the background model based on data differences (Daily et al., 2004; Labrecque & Yang, 2001). Other approaches include using an inverted background model as a starting or reference model for subsequent datasets (Miller et al., 2008; Oldenborger et al., 2007) or 4D (i.e. including time) regularization (Kim et al., 2009).

Electrical conductivity structure estimated using ERT can be constrained to favor inverse solutions that are consistent with hard data available at specific locations. Such hard data can be obtained from geophysical logs, which are routinely used in many environmental investigations to determine fracture intersection depths, static and transient

hydraulic flows surrounding these fractures, and fluid specific conductance (Keys, 1990). These logs provide fine-scale information to constrain conductivities close to the boreholes and thereby improve the hydrogeological significance of ERT images (Coscia et al., 2011; Johnson et al., 2012).

Site description

The study site for this ERT experiment is the former Naval Air Warfare Center (NAWC), located in West Trenton, NJ (USA) (Figure 5.1), which was used as a facility to test jet engines from 1955-1998. This site is representative of hundreds of contaminated sites in the eastern United States and thus the lessons learned here are potentially applicable to other fractured sedimentary sites. The fractured bedrock aquifer at the site was extensively contaminated with the chlorinated solvent trichloroethylene (TCE) during operations and presently fractures and the rock matrix are contaminated with TCE and its biotic degradation products cis-dichloroethylene (cDCE) and vinyl chloride (VC). Fill, weathered silt, and silty-clay saprolite are underlain by moderately-dipping alternating massive and laminated mudstone units which contain highly fractured black carbon-rich units (Figure 5.1c) (Lacombe & Burton, 2010; Tiedeman et al., 2010). This study focuses on the unweathered mudstone units where dominant flow pathways identified from hydraulic testing described below are through (1) a series of cross-cutting faults and (2) discrete fracture zones associated with the carbon rich intervals (Figure 1c) (Lacombe & Burton, 2010; Ellefsen et al., 2012).

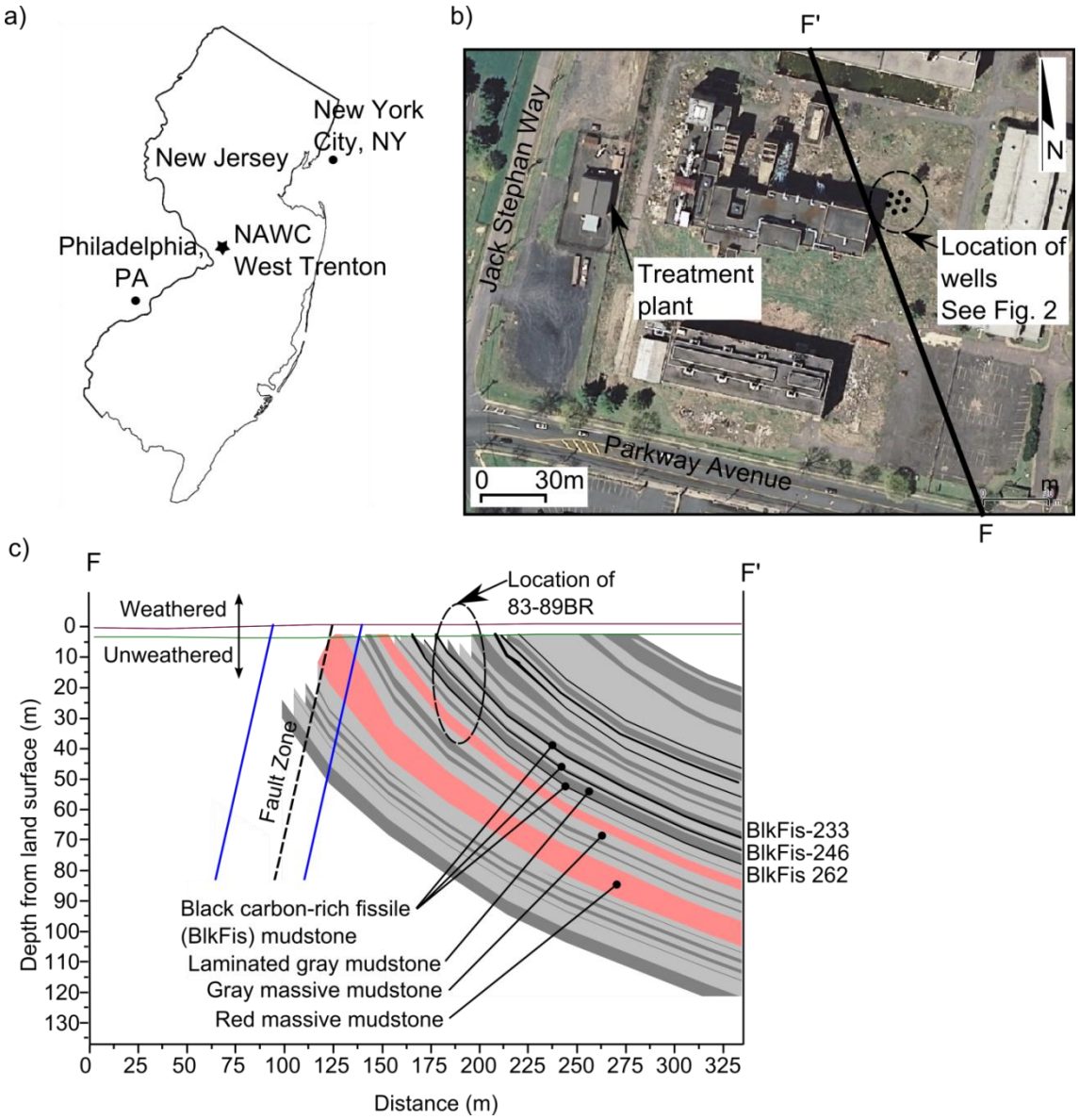

Figure 5.1: The Naval Air Warfare Center (NAWC) showing a) Location map b) Site plan c) Geologic section

A water treatment plant was constructed in the mid-1990s to facilitate pump and treat operations aimed at limiting offsite migration of contaminants (Goode et al., 2007). Analysis of treatment plant influent and groundwater pumped from the recovery boreholes shows that monthly removal amounts of TCE, cDCE and VC have stabilized since 2006 (Lacombe, 2011). Tracer tests conducted in three boreholes at the site exhibited rapid breakthrough, long tails, and large dilution of the injected tracer (Lewis-

Brown et al., 2005). Recent work by Goode et al., (2014) suggests that much of the contaminant mass is within the primary porosity (in aqueous phase or sorbed to the mudstones) and that back-diffusion (Parker et al., 1994) may cause elevated concentrations of contaminants for many years. Geophysical imaging of tracer tests may therefore provide valuable information on the fate of any amendment treatment and the controls of hydraulically transmissive pathways and fracture connectivity.

METHODS

Borehole drilling

Seven boreholes were closely spaced at NAWC in a unique survey design aimed at fully assessing the information content of ERT for imaging tracers and amendments in fractured rock at a scale appropriate for capturing tracer evolution beyond the borehole. The seven holes were drilled at 5 m intervals in a circular pattern with one hole in the center (83BR) and 6 holes along the circumference 84BR to 89BR (Figure 5.2). Construction of each hole consisted of drilling a 10-inch (25 cm) diameter borehole from land surface to approximately 15 m. This segment of the borehole passed though progressively less weathered bedrock. A 6-inch (15 cm) diameter PVC casing was installed in the 10-inch (25 cm) hole and the annular space was sealed with cement. Below this casing, each borehole was cored to penetrate three known highly fractured carbon units. Rock core samples

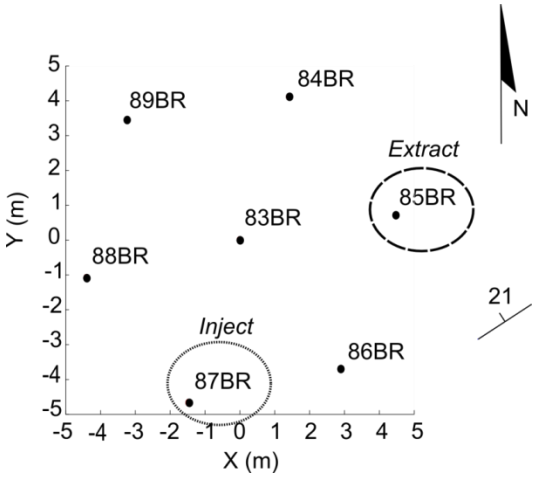

Figure 5.2: Well schematic used for the preliminary tracer experiments and ERT tracer test monitoring. Injection (87BR) and extraction (85BR) wells used for the ERT tracer test are highlighted. Strike and dip of the mudstone sequence (Figure 5.1c) also shown.

were collected and preserved, and the boreholes were left uncased for geophysical surveys, hydraulic and tracer testing, and ERT imaging. The uncased 4-inch (10 cm) boreholes range from 17-22.5 m in length. Depth to bottom of borehole below land surface ranges from 32-36.5 m.

Geophysical logs and supporting hydrogeological measurements

Numerous geophysical logs were collected on all seven boreholes including gamma-ray, optical televiewer (OTV), acoustical televiewer (ATV), caliper, ambient and stressed heat-pulse flow meter (HPFM), normal resistivity, fluid resistivity, temperature and borehole deviation. For brevity, only caliper logs and ATV logs are shown in Figure 5.3 as they effectively locate where fracture zones intersect the boreholes. Fracture zones can be identified as darker colored areas in ATV logs. In most cases, these darker colored areas correspond to enlarged diameters in the caliper logs. The HPFM recorded minimal vertical ambient flow; flow into and out of fracture zones only occurred in the upper half of the boreholes.

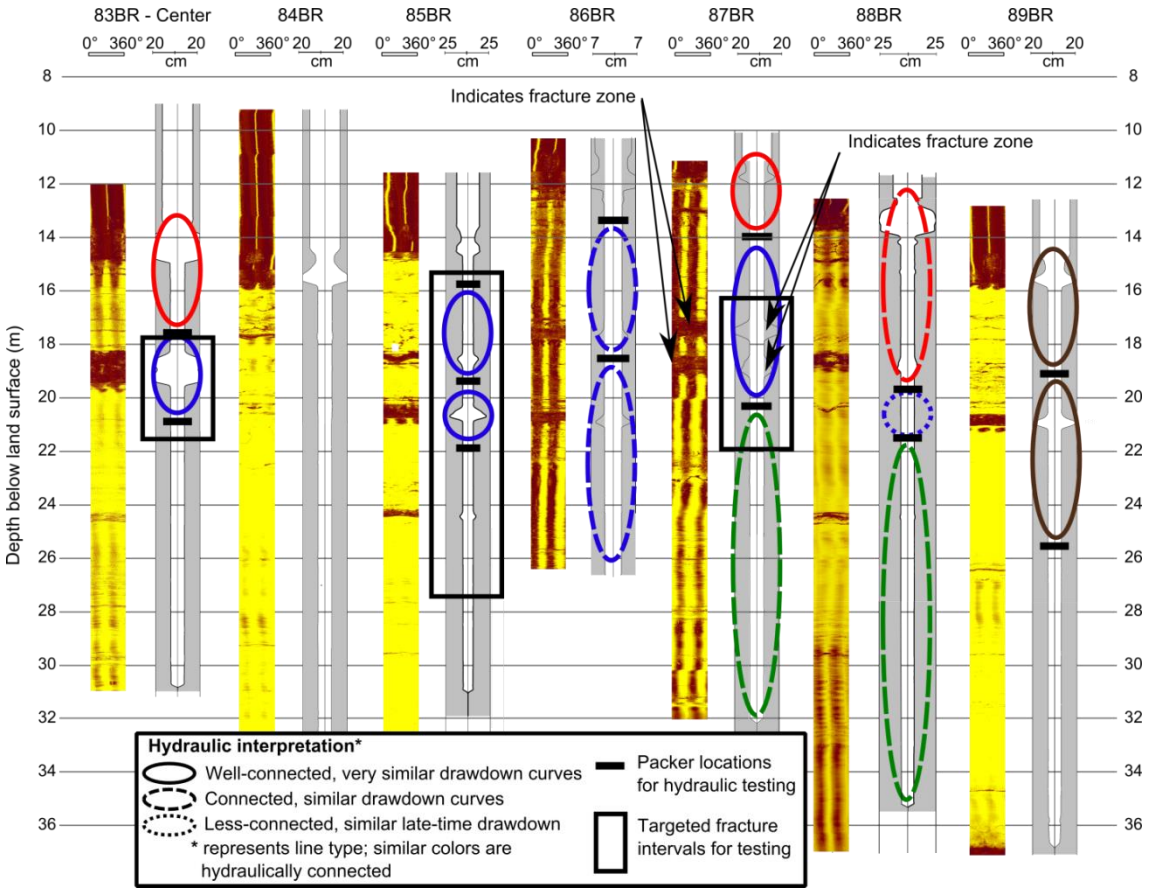

Figure 5.3: Hydraulic interpretation from drawdown data alongside caliper and ATV logs. Similarly colored ovals represent hydraulically connected packer-isolated borehole intervals. Packer placement for hydraulic testing is shown. There were no packers in 84BR, and only very small open-hole drawdown was detected during any aquifer testing.

Several one-hour cross-borehole hydraulic tests were conducted in the seven boreholes to determine hydraulic connections between boreholes for discrete intervals bounded by packers. Packers were located within each borehole (Figure 5.3) to isolate fracture zones using the geophysical logs (ATV, OTV, caliper, HPFM) as a guide. Custom-designed low-pressure packers (Figure 5.4a) were constructed and utilized in these aquifer tests and also in the electrode arrays described below. Figure 5.3 shows the hydraulic connections inferred from the drawdown data. Isolated borehole intervals with similar colors represent hydraulically connected intervals, while the line type

qualitatively denotes the degree of connectivity inferred from the drawdowns observed in response to pumping. Intervals between 83BR, 85BR and 87BR (solid blue circles) exhibited strong connectivity (Figure 5.3). The inferred high-permeability fracture zone between these three boreholes was selected as the focus of the tracer testing, delineated as the targeted fracture intervals for testing.

Electrode Arrays

Seven electrode arrays were custom-built for this site which, in addition to ERT imaging, allow for isolation of borehole intervals with low-pressure packers. In each borehole, one isolated interval was accessible from land surface via 0.5-inch (1.3 cm) diameter tubing. Tracer solutions were injected into and water samples were collected from this isolated interval. Three air supply lines to top, middle, and bottom packers provided flexibility to conduct tracer tests to target multiple fractures where necessary. For example, deflation of the middle packers in 85BR (Figure 5.4b) allowed both fractures within separate solid blue circles (Figure 5.3) to be targeted. The placement of 30 packers was determined from the geophysical logs and hydraulic testing (described above) such that fracture intervals were isolated from one another and discrete fracture zones could be targeted for tracer injection.

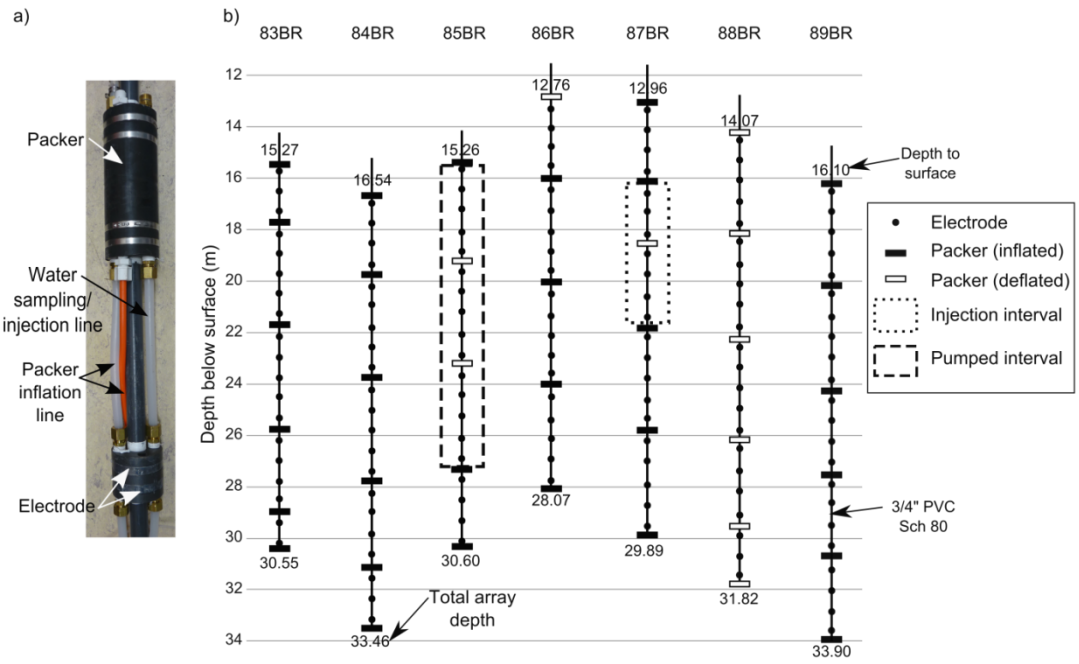

Figure 5.4: a) Low pressure packer in-line with electrode b) electrode array schematics within each borehole showing packer locations during ERT measurements and electrode locations.

Electrodes were spaced 0.8 m apart, representing a compromise between open-hole lengths and desired ERT image resolution. A total of 143 electrodes were used in this study, each constructed from two, 1" lead strips (Figure 5.4a). Both electrodes and packers were threaded onto a ¾" schedule 80 PVC pipe. Borehole 88BR had no packers inflated due to a sharp obstruction at the top of the open interval which punctured the packers upon installation (repeated attempts were made with the same result in each case). Table 1 and Figure 5.4 provide additional information on electrode array dimensions, depths and details.

Table 5.1: Electrode array details (per borehole)

Borehole Label	No. Electrodes	No. Packers Inflated	Length of ERT imaging (m)
83BR	19	6	15.28
84BR	21	6	16.92
85BR	19	3	15.34
86BR	19	4	15.40
87BR	21	5	16.93
88BR	22	0	17.75
89BR	22	6	17.85

Preliminary tracer tests

Several preliminary tracer tests were conducted in boreholes 83BR - 89BR prior to the ERT monitoring to better understand the hydraulics within the system and to help define the ERT survey configuration, including the time needed to acquire each ERT dataset. First, an experiment was conducted in open boreholes 83BR – 89BR in which a solution with an elevated concentration of deuterium oxide was continuously injected into 83BR. Boreholes 84BR-89BR were sampled and analyzed for concentrations of deuterium. The results of this experiment showed a response to the deuterium injection in boreholes 85BR and 87BR. The deuterium concentration in 84BR, 86BR, 88BR, and 89BR fluctuated around the ambient deuterium concentration in the groundwater. These results were qualitatively consistent with cross-hole hydraulic tests (Figure 5.3). The interpretation of this experiment was complicated by the fact that it was conducted in open boreholes such that (1) the density of the tracer solution may have had an impact on tracer migration pathways and (2) the dilution of the tracer was more prevalent without packed-off intervals. However, it was estimated that with an injection rate of 0.1 L/min the tracer first-arrival travel time between 83BR and 85BR was approximately 60 minutes; between 83BR and 87BR, the travel time was approximately 120 minutes.

Next, tracer tests using sodium bromide solutions were conducted within borehole pairs 83BR-85BR and 83BR-87BR. These involved a continuous injection of a conductive tracer in 83BR followed by a flush of native groundwater to disperse the tracer. These results showed rapid tracer migration, large tracer dilution, and extended breakthrough tailings that were interpreted to be due to the small volume of the preferential fracture zone and possible dead end fractures. Time-lapse ERT measurements collected while these injections took place were unsuccessful in imaging the tracer due in large part to (1) temporal smearing of measurements, and (2) a low conductivity contrast between the tracer fluid and the mudstone fractured rock due to dilution. However, lessons learned from this test were critical in the design of the successful ERT data acquisition and tracer composition for subsequent injection experiments described below.

ERT Data Acquisition

A modified Compare-R method (Paul B. Wilkinson et al., 2006b) was used to construct a cross borehole (i.e. current electrode pairs straddled between boreholes and potential electrode pairs straddled between boreholes) measurement sequence used in this study. Such sequences are expected to help to minimize current channeling along the boreholes. Nearest neighbor type configurations were then appended to this sequence similar to the survey used in Robinson, et al., (2013). Vertical Wenner (n=1) borehole profile configurations were also appended to the dataset and collected throughout the ERT tracer test (described below) to capture vertical variations in conductivity along each borehole profile over a shorter time frame than required for the 3D survey. The entire dataset contained 5,487 complete (i.e. for a total of 10,974 normal and reciprocal)

measurements and was acquired in approximately 20 minutes. The sequence constructed here and inverted ERT images from a quasi-3D sequence (7,045 complete measurements) and rotating dipole sequence (13,351 complete measurements) have visually similar overall conductivity structure while more contrasts in between borehole locations are emphasized in the optimized survey (Supplemental Figure 5.1).

Reciprocal ERT measurements were only collected before and after tracer tests (described below) in order to minimize the survey time during tracer tests and capture time-lapse changes. Acquired data were generally of high quality with only 4% of measurements filtered from all datasets. Outliers were defined as measurements that exceeded instrument specific limits (i.e. voltage and/or current) or measurements where background survey reciprocal errors exceeded 10%. Reciprocal errors for the remaining 5,263 measurements were very low. A data error model (after Koestel et al., 2008) found relative and absolute errors of 0.0035 and 0.0014 Ω, respectively.

A modified version of the parallel open source 3D ERT code, E4D, described in Johnson et al.,(2010) was used here for ERT modeling. Documentation describing the use and function of E4D are available at https://e4d.pnnl.gov. The following constraints were used for this study (1) sharp conductivity contrasts at borehole boundaries, and (2) maximum/minimum borehole and formation conductivity constraints based on geophysical logging information (3) a blocky inversion constraint in the region in between the boreholes and (4) anisotropic constraints based on the strike and dip of the formation. Sharp boundaries at inferred fracture locations were not employed due to the potential for image artifacts caused by the regularization as a result of geological complexity at NAWC as demonstrated in synthetic studies (Robinson et al., 2013).

Given the small data errors estimated from reciprocal measurements, the accuracy of the forward simulator was assumed to be the limiting factor in determining the appropriate level of data fit at convergence of the inverse solution. A relative data error of 0.05 percent was used based on the maximum expected numerical modeling error determined from forward simulations. However, an absolute minimum data error of 0.01 Ω was defined so that standard deviations of measurements with small resistances were not unrealistically small, thereby dominating the inversion. An unstructured tetrahedral mesh (659,035 tetrahedral elements) was used to discretize the model space. This finite element mesh explicitly incorporated the seven boreholes in true dimension with borehole deviations provided by geophysical logging data. For time-lapse ERT inverse modeling a background image was constructed based on inversion of a dataset collected before the injections occurred. For each subsequent time step, temporal changes in conductivity from the previous inverse solution were constrained to vary smoothly in space using transient regularization constraints between the current and previous solution.

While current channeling along boreholes has been previously acknowledged (Binley & Kemna, 2005; Coscia et al., 2011; Doetsch et al., 2010; Sugimoto, 1999), the benefit of using packers in cross-borehole ERT measurements has, with a few exceptions (Coscia et al., 2011; Labrecque & Yang, 2001), received little attention. To better understand if the packers affect resistance magnitudes, ERT measurements were first collected with packers inflated and deflated (encouraging current channeling) within individual boreholes. A dipole-dipole type measurement sequence, where the spacing between the current (i.e. transmitting) electrodes is equal to the spacing between the potential (i.e. receiving) electrodes, was used for this test as placing both current

electrodes in the same borehole enhances current channeling along the borehole (i.e. as opposed to cross borehole measurements). Boreholes 83BR, 84BR and 89BR each contain more packers than any of the other seven boreholes (Table 5.1, Figure 5.4), so these were chosen to illustrate the differences in resistances between measurements when the packers were inflated versus those when packers were deflated. To reveal the effect of differences of these datasets on the inverted models, a difference inversion was performed for 83BR, whereby data obtained with packers deflated were used to invert a background model. Relative changes from this background model were then determined using 83BR data when packers were inflated.

ERT Tracer Tests

Background ERT datasets (including reciprocal configurations) and water samples from 87BR were first collected before any disturbance to the system resulting from the ERT tracer test. The tracer test involved two separate fluid injections, in which a conductive tracer injection was subsequently followed by a resistive tracer injection. Based on the results of the preliminary tracer tests described above, the ERT tracer was injected in successive pulses using a peristaltic pump, where a pumped injection at 87BR occurred for five minutes and then the pump was shut off. ERT imaging occurred only when the injection pump was off, to limit temporal smearing over the 20 minute acquisition time. After the entire tracer volume was injected into 87BR, withdrawal from the extraction borehole, 85BR, occurred in the same fashion i.e., in five minute pulses, with the pump again turned off between each pulse. Water samples were collected during the pulsed extraction from 85BR. ERT imaging again only occurred when the extraction pump was off. To subsequently remove tracer mass from the system, the

extraction borehole (85BR) was pumped for a minimum of 16 hours. During this period, water samples were collected every 10 minutes for one hour, then hourly afterwards. Figure 5.5 presents a flowchart of the tracer experiment steps with step numbers denoted in square brackets [ ]. Table 5.2 contains the specific ERT tracer test details for each part of this experiment.

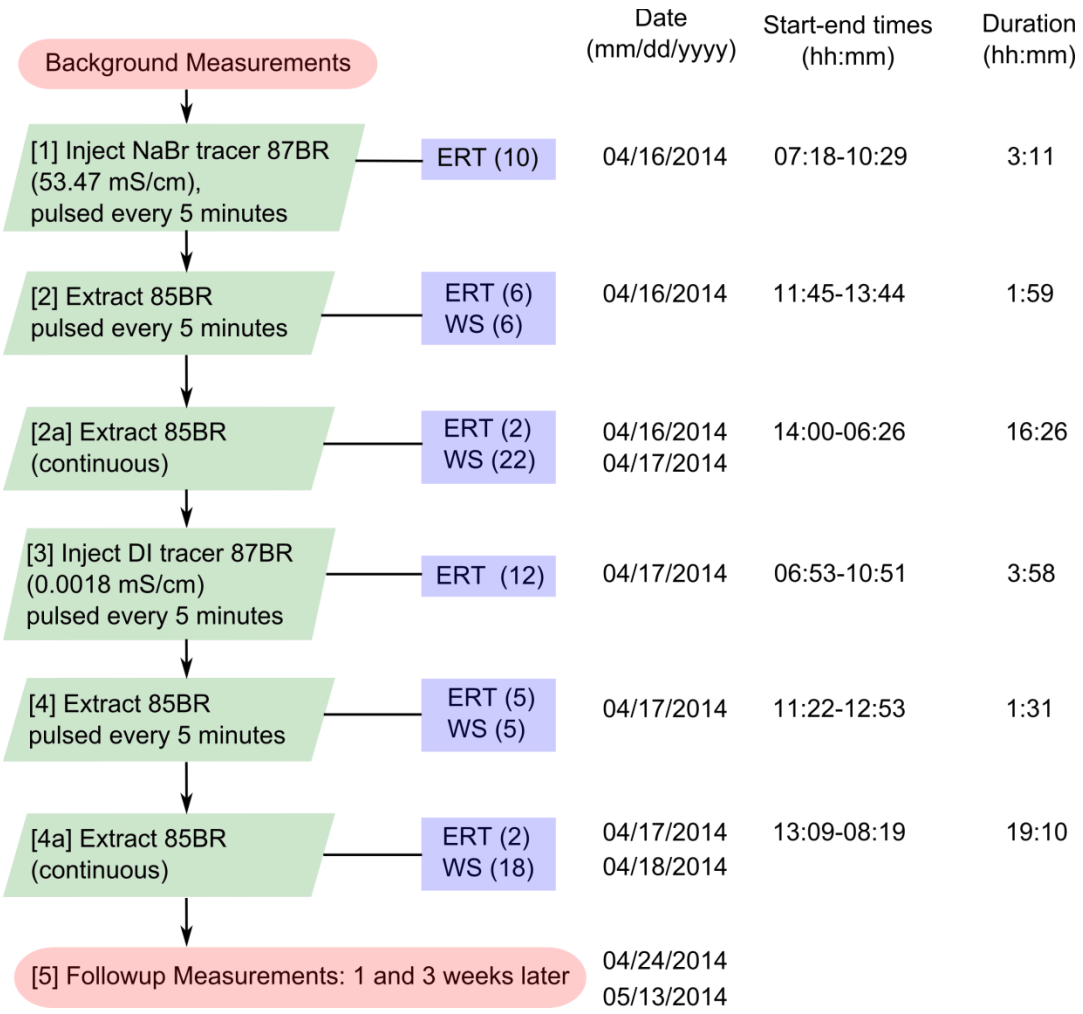

Figure 5.5: Flow chart of tracer test where numbers of ERT data acquisitions and water samples (WS) are indicated in parentheses ( ).

Native groundwater (22 L) was pumped from 87BR and used as the background medium for the conductive tracer injection (step [1] in Figure 5.5). Based on the high dilution effect observed during the preliminary tracer tests, a conductivity contrast of 89

was used between the native groundwater (0.60 mS/cm) and tracer solution (53.47 mS/cm). Samples of the injected tracer solution analyzed with ion chromatography (IC) had an average bromide concentration of 40.6 g/L. In addition to ERT datasets collected during the nine pulsed conductive injections in (step [1] in Figure 5.5), another ERT dataset was collected under static conditions shortly after the entire conductive volume was injected. This was followed by pulsed extraction with acquisition of five ERT data sets (step [2] in Figure 5.5). Finally, extended extraction (step [2a] in Figure 5.5) occurred for 16.5 hours.

Deionized water (DIW) was subsequently used as a resistive tracer and pulse-injected into 87BR for twelve intervals (step [3] in Figure 5.5). The fluid specific conductance for the DI water injected was $1.8x10^{-3}$ mS/cm, being 333 times more resistive than background concentrations; the true contrast was presumably higher due to the presence of residual tracer from the conductive injection. Five pulsed extractions occurred at 85BR after the resistive injection (step [4] in Figure 5.5). This was followed by 19.17 hours of extraction (step [4a] in Figure 5.5).

Table 5.2: ERT Tracer test details

Description	# pulsed injections	Approximate injection volume (L)	# water samples*	Approximate extraction volume (L)
[1] Conductive Injection	9	22	-	-
[2] Conductive Extraction	-	-	6	14
[2a] Extended Extraction	-	-	22	473
[3] Resistive Injection	12	34	-	-
[4] Resistive Extraction	-	-	5	8
[4a] Extended Extraction	-	-	25	674

* For [2] and [4], the # water samples = # pulsed extractions

Further ERT measurements (step [5] in Figure 5.5) were collected one and three weeks after tracer injection. One week after the tracer test, water was extracted from

85BR for four hours to facilitate further removal of tracer mass and to monitor bromide concentrations. Water samples were collected every five minutes for the first half hour, then hourly. ERT measurements were collected before and after the extraction. At three weeks post-tracer test, only ERT measurements were collected under no pumping conditions.

RESULTS

Effects of packers on current channeling

Assessment of raw ERT measurements suggests that the packers significantly limit current flow along the boreholes (Figure 5.6). The data collected within 88BR (no packers used) are highly repeatable (Figure 5.6b), with no repeated measurement having a difference greater than 0.1 Ω. The average percent change for all measurements in this test is 0.3 percent. In contrast, the data differences in 83BR, 84BR and 89BR when packers are inflated relative to uninflated show much larger changes for numerous measurements (Figure 5.6a). The average percent changes across all measurements in these boreholes due to inflation of the packers are 3.3, 7.7 and 5.6 percent, respectively. Figure 5.7a represents the conductivity structure for 83BR data with packers deflated. The inverted conductivity structure for 83BR data with packers inflated looks almost identical, and is thus not shown for brevity. The difference inversion image (Figure 5.7b) shows maximum conductivity changes of only 1% between packer locations in the vicinity of fracture zones (i.e. there are no changes below 28 m).

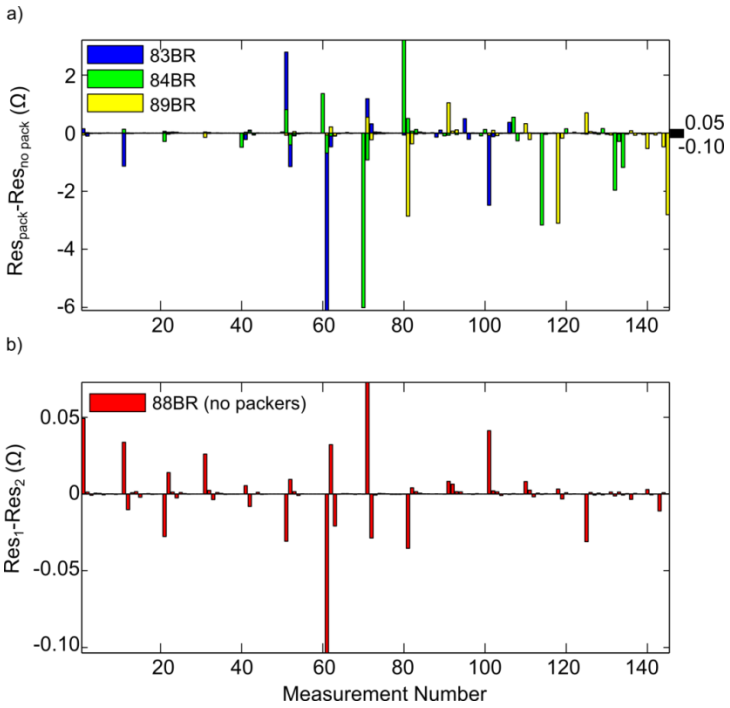

Figure 5.6: a) Measurements collected with packers inflated (Respack) and deflated (Resno pack) within single boreholes (83BR, 84BR and 89BR) demonstrate the effect of packers limiting current flow along the borehole. b) For comparative purposes, the difference between two consecutive datasets (Res1 and Res2) where packers were deflated in both cases is shown for 88BR. Note the difference in y-axis scales where the scale of b) is denoted on the right side y-axis a).

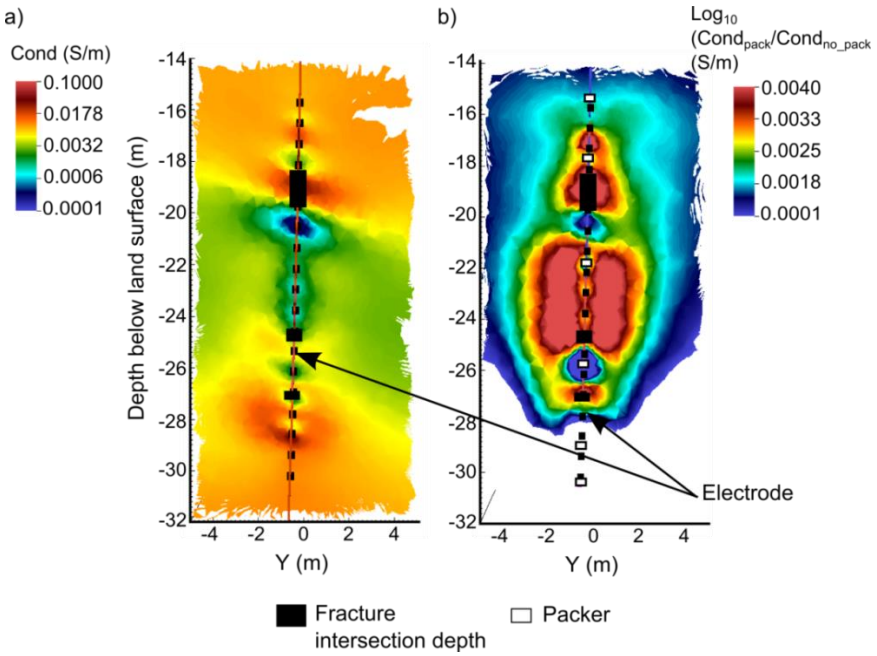

Figure 5.7: a) Inverted ERT image for 83BR single borehole data collected with packers deflated, and b) difference inversion showing relative changes in conductivity from packer data using a) as a background model.

Static resistivity images

The background ERT image is shown as a cross-section slice along 87-83-85BR to highlight structure along these planes of primary interest with regard to the tracer test (Figure 5.8). Electrically conductive zones align well with the fracture zone intersection depths and the orientation of the conductive and resistive zones generally align well with the strike and dip of the formation. The image reveals a subsurface structure of alternating conductive and resistive layers similar to the geological layering shown in Figure 5.5.1c. The OTV logs for 85BR and 87BR are shown alongside the inversion results where massive (M) and laminated (L) units have been annotated. Generally, lighter units correlate with less conductive massive units while darker units correlate with more conductive laminated units. However, where fracture intersection depths are closely spaced between a massive unit (e.g. (M*) in Figure 5.8), the data does not contain enough information to resolve the fractures that are closely spaced. An electrically

conductive pathway is shown between borehole pairs 87BR and 83BR and borehole pairs 83BR and 85BR; these pathways are within the targeted fracture zone interval for testing (Figures 3 and 8).

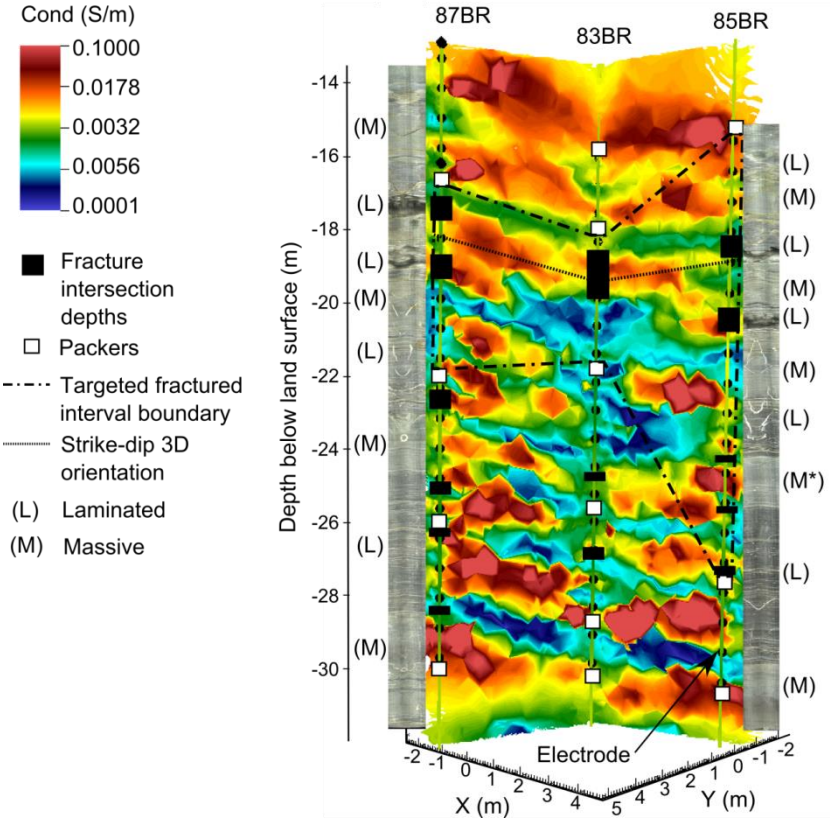

Figure 5.8: Electrical resistivity image for slice 85-83-87 with fracture intersection depths, packers and strike/dip of formation noted, showing alternating conductive and resistive layering partly resulting from the alternating laminated and massive mudstones at the site. The optical televiewer (OTV) log for 85BR and 87BR is shown for comparison. In order to present an unobstructed view of 83BR, 85BR (tracer extraction well) and 87BR (tracer injection well), 86BR is not shown.

Vertical apparent conductivity profiles

Relative changes in borehole apparent conductivities profiles for 83BR, 85BR and 87BR (the only boreholes showing significant changes) before and during the four stages of the tracer test are shown in Figure 5.9a, with 86BR shown for comparison. Figure 5.9a only shows a subset of the datasets collected at the end of step [1] through step [4a]

(Figure 5.5) within the ERT tracer test. The largest conductivity changes occur within 87BR and 83BR during the conductive injection. The effect of the resistive injection is seen in 87BR, with small to insignificant changes occurring in 83BR and 85BR. Extractions from 85BR appear to decrease conductivities in all boreholes (except 86BR).

Each point in Figure 5.9b represents an average of the largest apparent conductivity changes within isolated intervals of interest denoted by dashed boxes in Figure 5.9a as a function of time and experimental stage. The injection borehole (87BR) shows increases and decreases in apparent conductivity that coincide with conductive and resistive injections at 87BR and extractions at 85BR. The extraction borehole (85BR) shows no significant change in conductivity during the conductive injection, followed by an unexpected decrease before extraction occurs. Relative vertical apparent conductivities appear to decrease in 85BR and stay almost level. Borehole 83BR responds to the conductive injection at 87BR with an increasing conductivity, subsequently decreasing rapidly when the extraction pump is turned on at 85BR. There is a substantially larger relative change in conductivity in 83BR than in 87BR during the conductive fluid injection (Figure 5.9). Residual from preliminary field tracer tests (involving injection of a conductive tracer fluid) may account for this overall higher relative change. The resistive injection (step [3] in Figure 5.5) appears to have little effect on the relative vertical apparent conductivity changes in 83BR (Figure 5.9b).

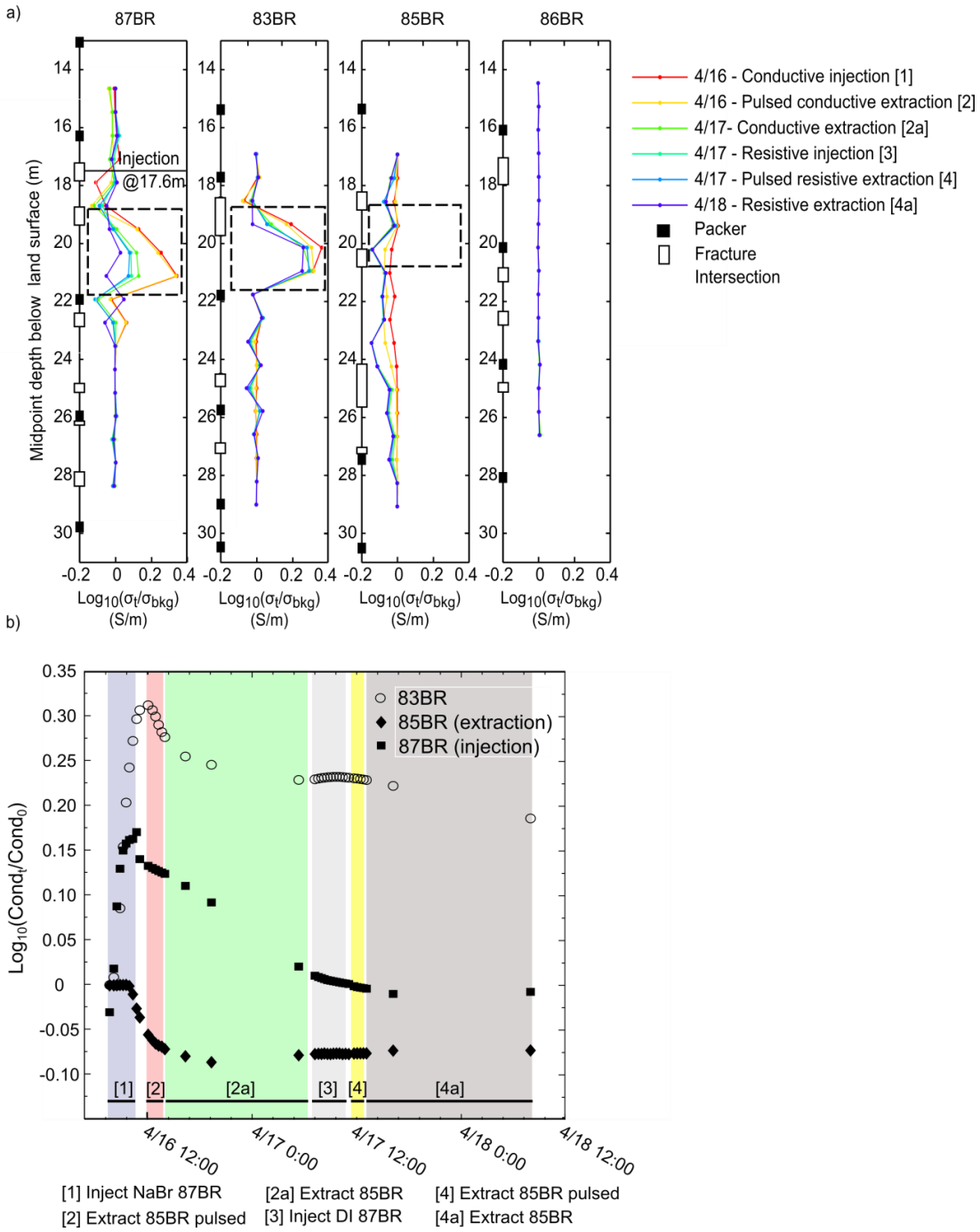

Figure 5.9: a) A subset of vertical apparent conductivity depth profiles for wells showing the largest conductivity changes: 87BR, 83BR, 85BR before and during the four-part tracer test. The response for 86BR is shown for comparison. b) Averaged relative changes in vertical apparent resistivities in 87BR (injection well) and surrounding wells 83BR, and 85BR (extraction well) within dashed intervals shown in a). Shaded regions correspond to the time boundaries for individual tracer test components.

Water sample data

Bromide and fluid specific conductance data from 85BR (only acquired during the extraction phases of the tracer test) are shown in Figure 5.10. Bromide concentrations and fluid specific conductance data generally mimic one another. The sharp decrease in bromide concentration and fluid specific conductance during the pulsed extraction from 85BR following the conductive injection is counterintuitive, indicative of an influx of resistive fluid into 85BR. However, concentrations increase as expected during the continuous extraction phase (step [2a]). Following the DI water injection (step [3] in Figure 5.5), initial bromide concentrations were low, possibly indicating an influx of low resistivity, DI water. However, this was followed by an increase in bromide and specific conductance.

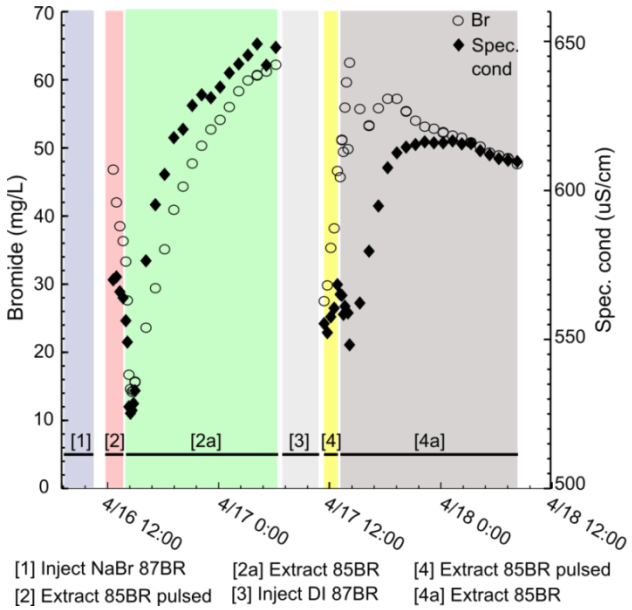

Figure 5.10: Fluid specific conductance and bromide concentrations for samples from 85BR

Time lapse 3D ERT imaging

Meaningful interpretation of time-lapse ERT imaging requires identification of conductivity changes in the images that can reliably be assigned to variations in subsurface conductivity structure (i.e. due to tracer injection in this case). In order to address this critical issue, a synthetic study was performed whereby forward models were generated from the baseline and final conductive injection inversions. Noise was added

to these datasets based on the error model used for the field datasets (described above) and a time-lapse inversion was performed. It was found that random inversion artifacts inconsistent with the migration of the tracer began to appear in the images when the minimum isocontour (of log10 conductivity relative to the background conductivity) was less than 0.035 S m^{-1}/S m^{-1}. Therefore, we assumed the ERT inversion detection capability to be equal to 0.035 S m^{-1}/S m^{-1}, representing a change in conductivity equal to 8.4%. All plots therefore show a minimum isocontour equal to this value.

A plan view (same orientation as Figure 5.2) of the migration of the conductive injection (step [1] in Figure 5.5) determined from the 3D ERT tracer study is shown in Figure 5.11A as relative changes from the background conductivity. The largest changes in spatial extent appear after the 3rd injection (Figure 5.11A-a) and persist until after the final (9th) injection (Figure 5.11A-h) and illuminate the migration of a conductive plume from 87BR to 83BR and in the direction of 88BR. Migration of the tracer to 85BR is not implied in these images. The evolution of the vertical extent of the conductive injection is shown in Figure 5.11B for the same time steps as in Figure 5.11A. The changes in conductivity are confined to the targeted fracture zone interval. The conductive plume appears just below the 2nd fracture zone in 87BR (at about 19 m below land surface (b.l.s.) as shown in Figure 5.3) and appears to enter 83BR at the bottom of the top fracture zone (at about 19.5 m b.l.s.).

Figure 5.12a through 12d show time-lapse images from datasets collected on the same day as the tracer injection tests beginning with the last conductive injection (Figure 5.12a is the same as Figure 5.11B-h). Figures 12b-c show conductivity changes after the first and last deionized water injections, respectively. Figure 5.12d is for data acquired

after 4 hours of extraction pumping from 85BR following the deionized water injection. Note that the resistive injection has little effect on the images shown in Figures 12b-d.

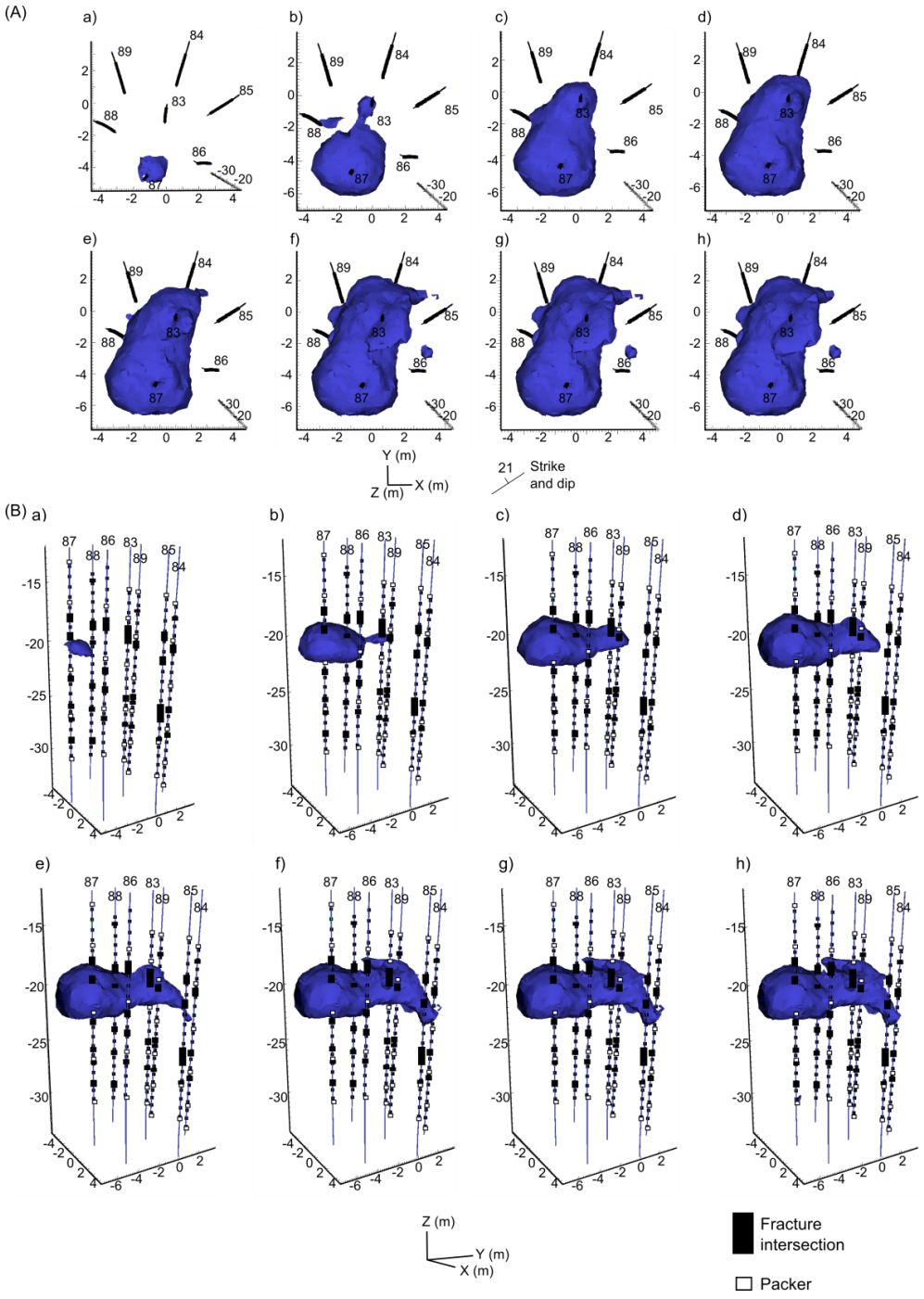

Figure 5.11: Time-lapse ERT image of relative change in electrical conductivity (condt = conductivity at time slice 't', cond0 = conductivity of background) during tracer injection showing (I) Plan view (II) elevation view. Images a-g represent the 2nd to 10th (last) injections. The 7th injection has been omitted due to minor conductivity changes from the previous injection The isocontour shown is equal to 0.035 which represents log10(Condt/Cond0).

Following the completion of the tracer test, extraction from 85BR for 20 hours has a dramatic effect on the relative change in conductivity with changes focused around 83BR. (Figure 5.12e) There is a decrease in the conductive plume surrounding 83BR one week following the tracer test (Figure 5.12f); after four hours of extraction from 85BR (Figure 5.12g), the plume is no longer visible. However, note that a decreased conductivity contrast between the tracer and the native groundwater due to fluid movement will limit ERT detection. Three weeks after the tracer injections, a conductive plume persists around 83BR in the ERT image (Figure 5.12h), possibly suggesting back-diffusion of conductive tracer (i.e. from this tracer injection or previous injections) from the matrix into the mobile domain.

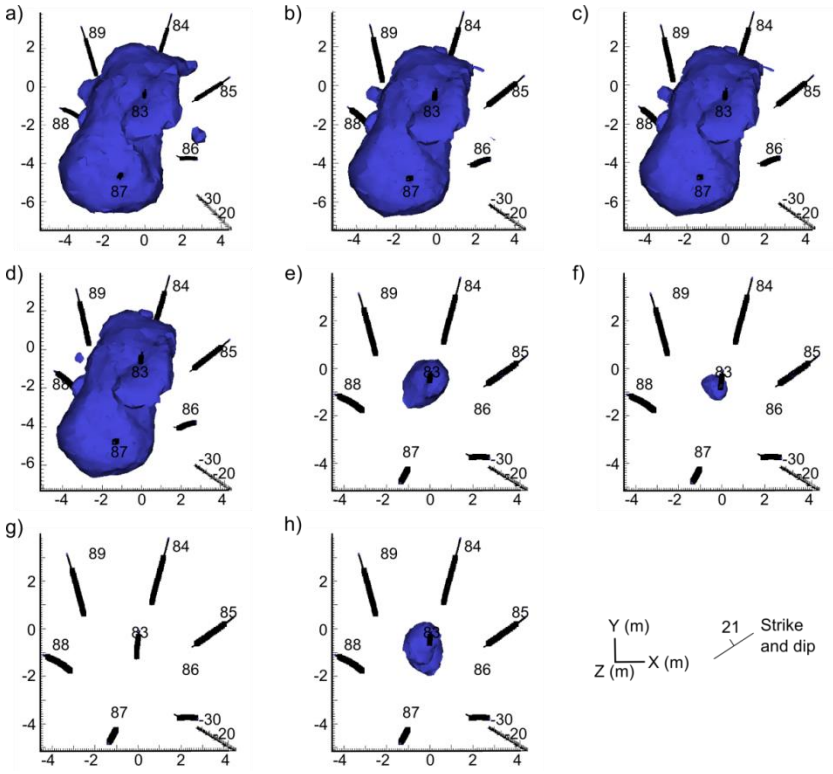

Figure 5.12: Time-lapse ERT images of relative change in electrical conductivity (Condt = conductivity at time slice 't', Cond0 = conductivity of background) following the conductive tracer injection: a) 30 minutes after the final conductive injection before extraction at 85BR (also shown in Figure 11h); b) 1st deionized water injection; c) last deionized water injection; d) 4 hours after 85BR extraction following deionized water injection; e) 20 hours after 85BR extraction following deionized water injection; e) One week following completion of tracer test f) One week following completion of tracer test after 4 hours of extraction from 85BR; f) Three weeks following the tracer test. The isocontour shown is equal to 0.035 which represents log10(Condt/Cond0).

DISCUSSION

To our knowledge, this study is the first example of the application of 3D cross-hole ERT for monitoring tracers injected into fractured rock systems whereby inter-borehole distances and electrode spacing were optimized such that the primary heterogeneity controlling tracer transport was captured. This required access to seven boreholes exclusively dedicated to the ERT study and in relatively close proximity to permit the desired resolution over the target image volume (approximately 1000 m^3). Preliminary tracer tests played a critical role in ensuring successful ERT imaging of the

tracer migration by constraining conductivity contrasts and tracer injection design (pulsed injection) required to reduce tracer fluid velocities and dilution rates (i.e. to limit ERT temporal smearing).

Background ERT images matched well with geology observed in boreholes, exhibiting alternating electrical conductivities consistent with the interlayered massive and laminated units and oriented consistent with the known strike and dip of the formation. The highest conductivity zones were located near fracture zone intersection depths. Due to the resolution limitations of the data, conductive fracture zones in the mudstone are most likely narrower than the images depict in Figure 5.8. Without making tenuous assumptions regarding the location of fracture zone boundaries within the bedrock beyond the boreholes, this is a difficult problem to overcome (Robinson et al., 2013).

The time-lapse ERT measurements provide valuable information at a plot scale appropriate for capturing migration pathways under a pulsed-tracer injection test. The 3D spatial extent of the tracer migration highlights flow and transport within a heterogeneous fractured rock system. The major flow pathways observed, particularly for the conductive injection, are likely in part due to the higher-density of the bromide tracer causing down-dip migration (Figure 5.2). Available geologic data and the hydraulic connections inferred from the drawdown data (Figure 5.3) are consistent with the migration pathways imaged in Figures 8, 9, 11 and 12. The 3D extent of the tracer could not have been resolved using standard borehole geophysical methods or hydraulic testing alone. For example, while the ERT images generally show tracer migration pathways that are down-dip in the direction of strike (Figures 11 and 12), more complexity is

revealed, particularly surrounding 88BR. The images indicate that a convoluted tracer transport pathway extending close to 88BR exists between 83BR and 87BR. This is consistent with results of the preliminary deuterium oxide tracer study whereby longer travel times were found between borehole pairs 83-87BR compared to borehole pairs 83-85BR. Characterizing fractured rock with ERT clearly enhances understanding of tracer transport pathways relative to point measurements from boreholes alone; such information could help to determine if target regions are reached during remediation treatments based on delivery of amendments to contaminated regions of the subsurface.

ERT imaging has limitations even at the relatively high resolution used in this study. Fluid specific conductance and bromide analysis of water samples from 85BR during the conductive and resistive extraction phases (Figure 5) reveal that conductive tracer did reach 85BR (Figure 5.10) during the continuous extraction from this borehole although this could not be resolved in the ERT images, which show changes greater than the threshold value of 8.4%. Fluid specific conductance readings during and following the resistive injection possibly reveal the presence of the resistive tracer, although this was not resolvable in the ERT images. Given the results of the hydraulic tests (Figure 5.3), tracer migration to the extraction borehole was anticipated and expected, consistent with the specific conductance and bromide analyses. ERT resolution is limited by multiple factors, including (1) the conductivity contrast between the tracer fluid and the pore fluid in the immobile and mobile domains, (2) the possibility of narrow fracture zones important for tracer transport that are smaller than the image resolution and (3) the numerical errors in the ERT modeling which exceed the actual data errors indicated by reciprocal measurements in this case. While large conductivity contrasts between the

native groundwater and the tracer fluids were used (factors of 89 and ~333), dilution of the tracer caused by the subsequent extraction, combined with the relatively low conductivity contrast between the host rock and the fracture zones probably limited the magnitude of the conductivity contrast to be less than the minimum required for ERT detection with the survey design used here. Furthermore, the ERT data may be relatively insensitive conductivity changes within a thin fracture zone extending towards 85BR, thereby rendering the inversion unable to resolve tracer migration within the fracture.

Inflated packers were presumed to help reduce current flow along the boreholes affecting resistance magnitudes where both current injection electrodes are within the same borehole. Measureable differences in the data well above the differences observed in 88BR with no packers led to higher conductivities within the formation near fracture zones (Figure 5.6b). However, the effects of employing the packers at this site on the inverted images were small with less than a 1% change in inverted conductivity. Synthetic tests by Robinson et al., (2013) are consistent with this finding. At NAWC, the contrast between the host rock and borehole fluid varied by only a factor of 10. The use of packers to limit current flow in more resistive environments (i.e. granitic rock) will likely result in more pronounced effects on the measurements. Additionally, the effectiveness of packers was limited by the fact that it was impractical to have more than 6 packers per borehole; additional packers would presumably result in greater reductions in current flow along the borehole. Finally, the measurements used here to test the influence of packers explored where current channeling would be more prevalent. Current injections during the tracer test were across boreholes, so the influence of packers would conceivably be even less pronounced than observed in these tests.

Vertical conductivity profiles provided information at high temporal resolution on changes in conductivity local to the boreholes. Specific conductance probes installed in an array along each borehole could provide finer-scale information than vertical apparent conductivities profiles. However, vertical apparent conductivity profiles have the advantage of sensing the fluid in the rock mass adjacent to the borehole in addition to just the fluid in the borehole itself. Furthermore, installation of conductivity probes along with the electrode array/packer assembly would be more challenging and expensive than the packer ERT array designed here. The 1D vertical profiles provided sufficient information at the borehole locations to (1) support the 3D ERT time-lapse results and (2) further confirm connectivity between the boreholes. Electrode arrays left in-place allowed 3D images of tracer transport to be captured while near-simultaneously acquiring 1D vertical conductivity changes local to each borehole, providing a proxy estimate of the information content that would be provided by a dense array of specific conductance probes installed in each borehole.

CONCLUSIONS

Tracer transport in a fractured rock system was imaged with high resolution ERT at a spatial scale consistent with variations in the primary heterogeneity controlling flow and transport at a site contaminated with TCE. This work demonstrated the resolution capabilities and limitations of ERT in a fractured rock setting. Preliminary tracer tests were critical for constraining the final design of the ERT tracer test by defining approximate travel times and conductivity contrasts necessary for successful imaging. The electrode array design, which integrated packers to isolate borehole intervals, permitted tracer fluids to be injected and water samples to be collected from targeted

fracture zones. The approach demonstrated here could be extended to other settings for effectively monitoring the fate of amendment injections into fractured rock aquifers beyond the borehole walls.

ACKNOWLEDGEMENTS

Funding for this project was provided by the U. S. Department of Defense (DOD) under the Environmental Security Technology Certification Program ER 201118 (L. Slater, PI). Inverse computations were performed on the Pacific Northwest National Laboratory Institutional Computing System (http://pic.pnnl.gov). We thank Daniel Goode for his contributions to this project. We are grateful for the field and lab support provided by Sundeep Sharma, Jeff Heenan, Jay Nolan and USGS summer interns Alex Fiore, Carla Valdes and Chris Leach. Additional support for this work came from the U.S. Geological Survey Toxic Substances Hydrology Program. Any use of trade, firm, or product names is for descriptive purposes only and does not imply endorsement by the U.S. Government.

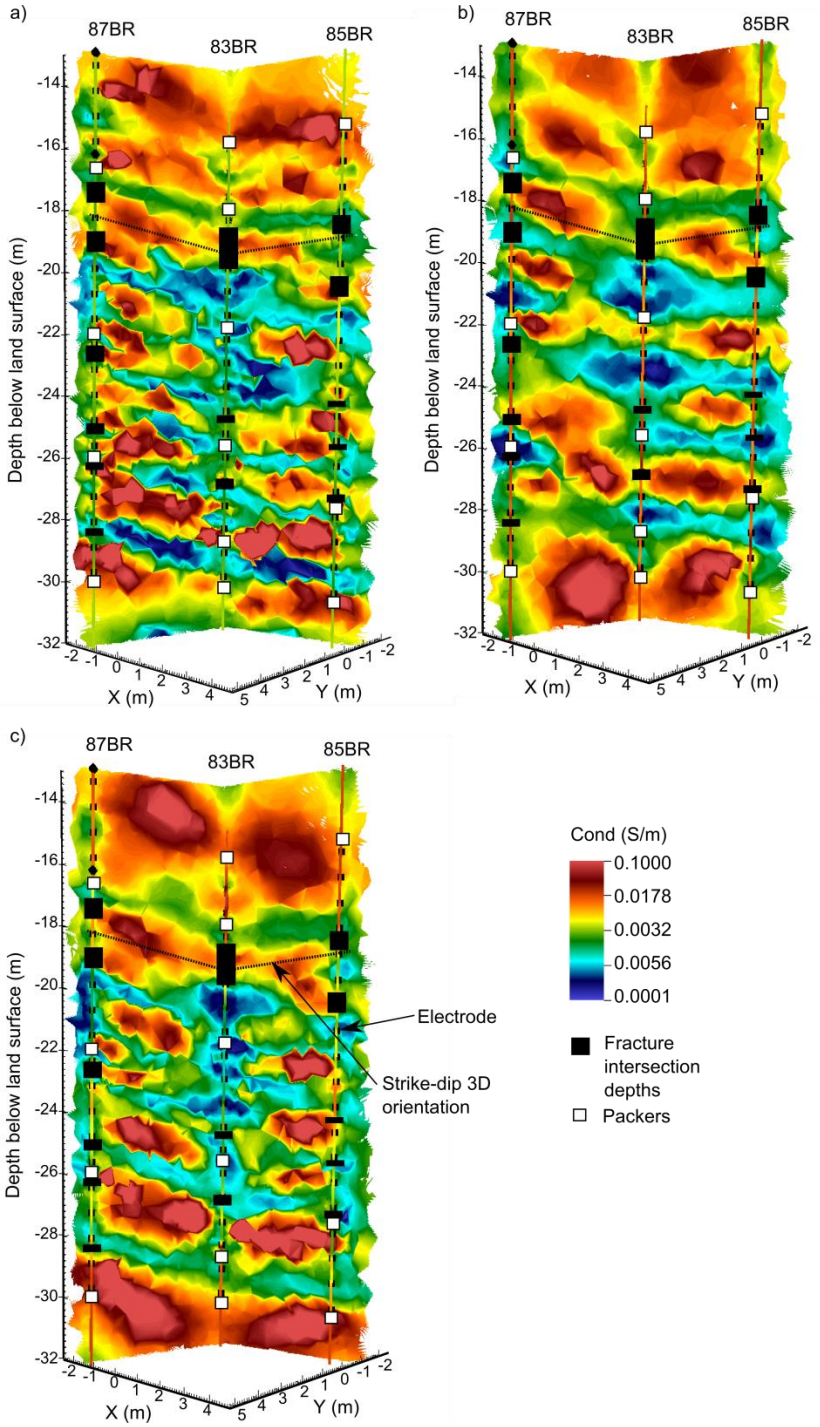

Supplemental Figure 1: Inverted characterization images where measurement sequences are a) 3D optimized cross borehole survey combined with dipole-dipole sequence (5,263 measurements) b) 3D rotating dipole sequence (13,351 measurements) an d c) quasi-3D sequence of 2D panels (7,045 measurements).

Chapter 6: Conclusions and recommendations for future work

6.1 Primary scientific findings and significance

Using novel modeling techniques and instrumentation, ERT can provide spatiotemporal information unavailable from other standard methods. Clearly, the information obtained from standard borehole methods needs additional approaches to understand the complex flow and transport processes occurring in fractured media. While employing ERT in fractured rock is not new, this dissertation critically examines ways in which applying appropriate model constraints in a deterministic approach can yield additional hydrogeological information when compared to standard ERT inversion modeling approaches.

ERT instrumentation exists to collect datasets with hundreds of electrodes consisting of thousands of measurements. Access to newly available parallelized codes and computers with a large number of processors allowed for efficient processing in 3D. The benefits of this are very apparent in this research: the spatial distribution of 3D static and time-lapse ERT changes yielded a spatially more extensive and complete view of subsurface structures and conductivity images than achievable with 2D inverse methods.

The first research topic revealed the viability of using ERT data to model fractures and conductive boreholes in a mudstone environment. The results were encouraging: by allowing a sharp contrast between the host rock and assumed fracture locations and boreholes, the inversion artifacts were very limited. Also encouraging was the fact that in this synthetic study there was only one order of magnitude difference in conductivity between the host rock and the fracture zones/boreholes (i.e. the ERT data was capable of picking up these low contrasts). Misplacement of the assumed fracture

location did present challenges, although these were identifiable in this first phase of the research.

Working with the Middlebarrow Quarry field data (Chapter 3) proved more challenging than working with the synthetic datasets. Applying borehole conductivity constraints and regularization disconnects along borehole boundaries improved the interpretation. Inversion artifacts from non-vertical boreholes and likely misplacement of a fracture plane were apparent when the starting conductivity model was modified. It became evident during this study that de-regularizing (i.e. removing smoothness constraints) localized features could result in false electrical signatures. De-regularizing of localized features provides a powerful tool for analyzing ERT datasets, however unless there is some degree of confidence in the location, (i.e. as would be the case with boreholes, particularly with a deviation log) this should be avoided as misinterpretation is likely. This is an important finding given the fact that other researchers are using regularization disconnects without documenting the negative consequences.

The third research topic was the most comprehensive and involved task in this dissertation: ERT electrode arrays were built and installed; surface packer inflation lines were constructed; preliminary tracer tests were performed which were critical to the final successful test design. Throughout this phase the ERT modeling code, E4D was evolving into an open-source code and new, novel model regularization constraints could be applied to the datasets. The results were a spatial distribution of tracer migration surrounding seven boreholes revealing flow and transport characteristics within the fracture zone, a significant achievement given the complexity of the fracture network.

The results from the work presented here demonstrates the capability of ERT to spatially delineate static and transient processes in fractured rock that can aid geoscience professionals in the development of natural resources and the delivery of amendment injections at contaminated sites. This thesis presents a first step in further development of ERT monitoring in fractured rock environments with a goal to provide flow and transport models at these complex sites.

6.2 Challenges and recommendations for future work

A major challenge remains regarding modeling ERT in fractured rock: conductive features representing fractures were resolved in the inversions as having much larger apertures than actually exist. The research in this thesis demonstrates that assuming fracture locations and removing smoothness constraints at this boundary could resolve this issue. However, assuming these locations is tenuous given the convoluted and highly heterogeneous nature of fracture networks. Work still needs to be done to extract more information from these datasets. One suggestion is to provide finer discretization in the host rock in regions surrounding injection locations or high conductivity contrasts. A finer discretization using blocky model constraints may narrow the contrasting region (i.e. the fractures). Iterative mesh refinements based on regions of interest from previous inversions may also focus changes within the fractured rock. When working with time-lapse datasets, it may be beneficial to work only with changes in the data that are over a chosen percentage change threshold value (i.e. above the noise within the dataset). This may focus the changes to more localized regions for further consideration.

The next step in interpreting ERT data in fractured rock is using changes in conductivity as a proxy for concentrations changes of either a contaminant or tracer fluid within the fractures. This is a difficult task to achieve without further refining the regions of contrast (i.e. with an iterative or finer mesh) and understanding the dilution rates and processing affecting these rates occurring within the system.

Another promising next step would be to combine ERT spatial delineation of tracer/amendment transport with hydrogeological models. Combining these models could go a long way towards defining preferential flow paths, dead end pore spaces and allowing hydrogeologists to constrain their models in a physically meaningful way.

The prototype electrode arrays designed and constructed had limitations based on the exterior diameter openings within the electrodes and packers for the fluid and air lines (Figure 5.4a). Based on the number and size of the openings, a weakness was present in the electrode/packer block if too much pressure was applied by adding/adjusting fittings or securing the interior pipe. This weakness was even more evident where we were forced to use brass fittings due to space restrictions and sizing of fittings (Figure 5.4a). The inflatable material used for the packer was a motorcycle tire inner tube and more puncture resistant material is necessary to limit tears. Finally, most connections used low cost compression fittings to limit the expense. Higher quality fittings (e.g. yor-lok) would be beneficial to ensure a tight seal but overall, the number of fittings should be reduced which could be achieved with a modified electrode/packer block.

Finally, the field study at NAWC is a mudstone fractured rock, which likely contains a significant amount of fine material contributing to a polarization response. Although not advisable for time-lapse studies due to longer data collection,

characterization of the host rock in this setting would most likely benefit from information from an induced polarization (IP) survey.

This work brings ERT into an environment where studies are lacking and paves the way for future researchers to continue in other underexplored environments. Ultimately, the modeling work presented here focused on how to extract additional meaningful information from ERT datasets, with careful consideration of the experimental setup and design. This is the goal of any ERT study and will serve as an idea basis for my future endeavors and hopefully other researchers as well.

References

A. Binley, & A. Kemna. (2005). DC Resistivity and Induced Polarization Methods. In Y. Rubin & S. . Hubbard (Eds.), *Hydrogeophysics* (v50 ed., pp. 129–156).

Backus, G., & Gilbert, F. (1968). The Resolving Power of Gross Earth Data. *Geophysical Journal International*, *16*(2), 169–205. doi:10.1111/j.1365-246X.1968.tb00216.x

Barker, J. A. (1981). A formula for estimating fissure transmis- sivities from steady-state injection-test data. *Journal of Hydrology*, *52*, 337–346.

Bazin, S., & Pfaffhuber, a. a. (2013). Mapping of quick clay by electrical resistivity tomography under structural constraint. *Journal of Applied Geophysics*, *98*, 280–287. doi:10.1016/j.jappgeo.2013.09.002

Becker, M. W., & Shapiro, A. M. (2000). Tracer transport in fractured crystalline rock: Evidence of nondiffusive breakthrough tailing. *Water Resources Research*, *36*(7), 1677–1686. doi:10.1029/2000WR900080

Becker, M. W., & Tsoflias, G. P. (2010). Comparing flux-averaged and resident concentration in a fractured bedrock using ground penetrating radar. *Water Resources Research*, *46*(9), W09518 (1–12). doi:10.1029/2009WR008260

Benson, R. C., & Yuhr, L. (1993). Spatial sampling considerations and their applications to characterizing fractured rock and karst systems. *Environmental Geology*, *22*(4), 296–307. doi:10.1007/BF00767501

Berkowitz, B. (2002). Characterizing flow and transport in fractured geological media: A review. *Advances in Water Resources*, *25*(8-12), 861–884. doi:10.1016/S0309-1708(02)00042-8

Blome, M., Maurer, H., & Greenhalgh, S. (2011). Geoelectric experimental design — Efficient acquisition and exploitation of complete pole-bipole data sets. *Geophysics*, *76*(1), F15–F26. doi:10.1190/1.3511350

Blome, M., Maurer, H. R., & Schmidt, K. (2009). Advances in three-dimensional geoelectric forward solver techniques. *Geophysical Journal International*, *176*(3), 740–752. doi:10.1111/j.1365-246X.2008.04006.x

Bradley, P., Journey, C., Kirshtein, J., Voytek, M., Lacombe, P., Imbrigiotta, T. E., … Goode, D. J. (2012). Enhanced Dichloroethene Biodegration in Fractured Rock Under Biostimulated and Bioaugmented Conditions. *Remediation*, *Spring*, 21–32.

Briggs, M. A., Day-Lewis, F. D., Ong, J. B., Harvey, J. W., & Lane, J. W. (2014). Dual-domain mass-transfer parameters from electrical hysteresis: Theory and analytical

approach applied to laboratory, synthetic streambed, and groundwater experiments. *Water Resources Research*, *50*(10), 8281–8299. doi:doi:10.1002/2014WR015880

Briggs, M. a., Day-Lewis, F. D., Ong, J. B. T., Curtis, G. P., & Lane, J. W. (2013). Simultaneous estimation of local-scale and flow path-scale dual-domain mass transfer parameters using geoelectrical monitoring. *Water Resources Research*, *49*(9), 5615–5630. doi:10.1002/wrcr.20397

Brown, D., & Slater, L. D. (1999). Focused packer testing using geophysical tomography and CCTV in a fissured aquifer Electrical resistivity tomography (ERT) Research site, (1995), 173–183.

Chambers, R. Ogilvy, O. Kuras, J. C, J. (2002). 3D electrical imaging of known targets at a controlled environmental test site. *Environmental Geology*, *41*(6), 690–704. doi:10.1007/s00254-001-0452-4

Coscia, I., Greenhalgh, S. A., Linde, N., Doetsch, J., Marescot, L., Gu, T., … Green, A. G. (2011). 3D crosshole ERT for aquifer characterization and monitoring of infiltrating river water. *Geophysics*, *76*(2), G49–G59.

Daily, W., & Ramirez, A. (1995). Electrical resistance tomography during in-situ trichloroethylene remediation at the Savannah River Site. *Journal of Applied Geophysics*, *33*, 239–249.

Daily, W., Ramirez, A., Binley, A., & LaBrecque, D. (2004). Electrical resistance tomography. *The Leading Edge*, *2*, 438–442.

Day-Lewis, F. D., Lane, J. W., & Gorelick, S. M. (2004). Combined interpretation of radar, hydraulic, and tracer data from a fractured-rock aquifer near Mirror Lake, New Hampshire, USA. *Hydrogeology Journal*, *14*(1-2), 1–14. doi:10.1007/s10040-004-0372-y

Day-Lewis, F. D., Lane, J. W., Harris, J. M., & Gorelick, S. M. (2003). Time-lapse imaging of saline-tracer transport in fractured rock using difference-attenuation radar tomography. *Water Resources Research*, *39*(10), n/a–n/a. doi:10.1029/2002WR001722

Day-Lewis, F. D., & Singha, K. (2008). Geoelectrical inference of mass transfer parameters using temporal moments. *Water Resources Research*, *44*(5), n/a–n/a. doi:10.1029/2007WR006750

deGroot-Hedlin, C., & Constable, S. (1990). Occam's inversion to generate smooth, two- dimensional models from magnetotelluric data. *Geophysics*, *55*(12), 1613–1624. doi:10.1190/1.1442813

Dentz, M., & Berkowitz, B. (2003). Transport behavior of a passive solute in continuous time random walks and multirate mass transfer. *Water Resources Research*, *39*(5), n/a–n/a. doi:10.1029/2001WR001163

Doetsch, J. A., Coscia, I., Greenhalgh, S., Linde, N., Green, A., & Günther, T. (2010). The borehole-fluid effect in electrical resistivity imaging. *Geophysics*, *75*(4), F107–F114. doi:10.1190/1.3467824

Doetsch, J., Linde, N., Pessognelli, M., Green, A. G., & Günther, T. (2012). Constraining 3-D electrical resistance tomography with GPR reflection data for improved aquifer characterization. *Journal of Applied Geophysics*, *78*, 68–76. doi:10.1016/j.jappgeo.2011.04.008

Dorn, C., Linde, N., Le Borgne, T., Bour, O., & Klepikova, M. (2012). Inferring transport characteristics in a fractured rock aquifer by combining single-hole ground-penetrating radar reflection monitoring and tracer test data. *Water Resources Research*, *48*(11), n/a–n/a. doi:10.1029/2011WR011739

Farquharson, C. G. (2008). Constructing piecewise-constant models in multidimensional minimum-structure inversions. *Geophysics*, *73*(1), K1–K9.

Furman, A., Ferre, T. P. A., & Warrick, A. W. (2003). A Sensitivity Analysis of Electrical Resistivity Tomography Array Types Using. *Vadose Zone Journal*, *2*, 416–423.

Goode, D. J., Imbrigiotta, T. E., & Lacombe, P. J. (2014). High-resolution delineation of chlorinated volatile organic compounds in a dipping, fractured mudstone: Depth- and strata-dependent spatial variability from rock-core sampling. *Journal of Contaminant Hydrology*. doi:10.1016/j.jconhyd.2014.10.005

Goode, D. J., Tiedeman, C. R., Lacombe, P. J., Imbrigiotta, T. E., Shapiro, A. M., & Chapelle, F. H. (2007). Contamination in Fractured-Rock Aquifers—Research at the former Naval Air Warfare Center, West Trenton, New Jersey. *USGS Fact Sheet 2007-3074*, http://pubs.usgs. gov/fs/2007/3074/.

Günther, T., Rücker, C., & Spitzer, K. (2006). Three-dimensional modelling and inversion of dc resistivity data incorporating topography - II. Inversion. *Geophysical Journal International*, *166*(2), 506–517. doi:10.1111/j.1365-246X.2006.03011.x

Henderson, R. D., Day-Lewis, F. D., Harvey, C. F., Abarca, E., Karam, H. N., Liu, L., & Lane, J. . (2010). Marine Electrical Resistivity Imaging of Submarine Ground-Water Discharge: Sensitivity Analysis and Application in Waquoit Bay, Massachusetts. *Hydrogeology Journal*, *18*(1), 173–185.

Johnson, T. (2014). *E4D : A distributed memory parallel electrical geophysical modeling and inversion code User Guide - Version 1.0* (p. 134).

Johnson, T. C., Slater, L. D., Ntarlagiannis, D., Day-Lewis, F. D., & Elwaseif, M. (2012). Monitoring groundwater-surface water interaction using time-series and time-frequency analysis of transient three-dimensional electrical resistivity changes. *Water Resources Research*, *48*(7), n/a–n/a. doi:10.1029/2012WR011893

Johnson, T. C., Versteeg, R. J., Day-Lewis, F. D., Major, W., & Lane, J. W. (2014). Time-Lapse Electrical Geophysical Monitoring of Amendment-Based Biostimulation. *Ground Water*. doi:10.1111/gwat.12291

Johnson, T. C., Versteeg, R. J., Rockhold, M., Slater, L. D., Ntarlagiannis, D., Greenwood, W. J., & Zachara, J. (2012). Characterization of a contaminated wellfield using 3D electrical resistivity tomography implemented with geostatistical, discontinuous boundary, and known conductivity constraints. *Geophysics*, *77*(6), EN85–EN96. doi:10.1190/geo2012-0121.1

Johnson, T. C., Versteeg, R. J., Ward, A., Day-lewis, F. D., & Revil, A. (2010). Improved hydrogeophysical characterization and monitoring through parallel modeling and inversion of time-domain resistivity and induced-polarization data. *Geophysics*, *75*(4).

Keys, W. S. (1990). Borehole geophysics applied to ground-water investigations. *US Department of the Interior, US Geological Survey*.

Kim, J.-H., Yi, M.-J., Park, S.-G., & Kim, J. G. (2009). 4-D inversion of DC resistivity monitoring data acquired over a dynamically changing earth model. *Journal of Applied Geophysics*, *68*(4), 522–532. doi:10.1016/j.jappgeo.2009.03.002

Koestel, J., Kemna, A., Javaux, M., Binley, A., & Vereecken, H. (2008). Quantitative imaging of solute transport in an unsaturated and undisturbed soil monolith with 3-D ERT and TDR. *Water Resources Research*, *44*(12), n/a–n/a. doi:10.1029/2007WR006755

LaBrecque, D. J., Miletto, M., Daily, W., Ramirez, A., & Owen, E. (1996). The effects of noise on Occam's inversion of resistivity tomography data. *Geophysics*, *61*(2), 538–548. doi:10.1190/1.1443980

Labrecque, D. J., & Yang, X. (2001). Difference Inversion of ERT Data : a Fast Inversion Method for 3-D In Situ Monitoring. *Journal of Environmental and Engineering Geophysics*, *6*(2), 83–89.

Labrecque, D., & Yang, X. (2001). Difference Inversion of ERT Data : a Fast Inversion Method for 3-D In Situ Monitoring. *Journal of Environmental and Engineering Geophysics*, *6*(2), 83–89.

Lacombe, P. J. (2011). *Mass of Chlorinated Volatile Organic Compounds Removed by Pump-and-Treat , Naval Air Warfare Center , West Trenton , New Jersey , 1996-2010: USGS Scientific Investigations Report 2011-5003* (p. 48).

Lacombe, P. J., & Burton, W. C. (2010). Hydrogeologic Framework of Fractured Sedimentary Rock , Newark Basin , New Jersey, (2), 35–45. doi:10.1111/j1745

Last, B. J., & Kubik, K. (1983). Compact gravity inversion. *Geophysics*, *48*(6), 713–721. doi:10.1190/1.1441501

Lewis-Brown, B. J. C., Carleton, G. B., & Imbrigiotta, T. E. (2005). *Hydraulic and Solute-Transport Properties and Simulated Advective Transport of Contaminated Ground Water in a Fractured- Rock Aquifer at the Naval Air Warfare Center , West Trenton , New Jersey , 2003 Scientific Investigations Report 2005-5049* (p. 32).

Li, Y., & Oldenburg, D. W. (2000). Joint inversion of surface and three-component borehole magnetic data. *Geophysics*, *65*(2), 540–552. doi:10.1190/1.1444749

Lines, L. R., Schultz, A. K., & Treitel, S. (1988). Cooperative inversion of geophysical data. *Geophysics*, *53*(1), 8–20. doi:10.1190/1.1442403

Loke, M. H., Wilkinson, P. B., & Chambers, J. E. (2010). Fast computation of optimized electrode arrays for 2D resistivity surveys. *Computers & Geosciences*, *36*(11), 1414–1426. doi:10.1016/j.cageo.2010.03.016

Lowry, T., Allen, M. B., & Shive, P. N. (1989). Singularity removal: A refinement of resistivity modeling techniques. *Geophysics*, *54*(6), 766–774. doi:10.1190/1.1442704

Mack, T. J. (1993). Detection of Contaminant Plumes by Borehole Geophysical Logging. *Groundwater Monitoring and Remediation*, *13*(1), 107–114.

Meyerhoff, S. B., Maxwell, R. M., Revil, A., Martin, J. B., Karaoulis, M., & Graham, W. D. (2014). Characterization of groundwater and surface water mixing in a semiconfined karst aquifer using time-lapse electrical resistivity tomography. *Water Resources Research*, *50*, 2566–2585. doi:10.1002/2013WR013991.Received

Miller, C. R., Routh, P. S., Brosten, T. R., & McNamara, J. P. (2008). Application of time-lapse ERT imaging to watershed characterization. *Geophysics*, *73*(3), G7–G17. doi:10.1190/1.2907156

Mwakanyamale, K., Slater, L., Binley, A., & Ntarlagiannis, D. (2012). Lithologic imaging using complex conductivity: Lessons learned from the Hanford 300 Area. *Geophysics*, *77*(6), E397–E409. doi:10.1190/geo2011-0407.1

Neuman, S. P. (2005). Trends, prospects and challenges in quantifying flow and transport through fractured rocks. *Hydrogeology Journal*, *13*(1), 124–147. doi:10.1007/s10040-004-0397-2

Nimmer, R. E., Osiensky, J. L., Binley, A. M., Sprenke, K. F., & Williams, B. C. (2007). Electrical resistivity imaging of conductive plume dilution in fractured rock. *Hydrogeology Journal*, *15*(5), 877–890. doi:10.1007/s10040-007-0159-z

Oldenborger, G. a., Knoll, M. D., Routh, P. S., & LaBrecque, D. J. (2007). Time-lapse ERT monitoring of an injection/withdrawal experiment in a shallow unconfined aquifer. *Geophysics*, *72*(4), F177–F187. doi:10.1190/1.2734365

Oldenborger, G. a., Routh, P. S., & Knoll, M. D. (2005). Sensitivity of electrical resistivity tomography data to electrode position errors. *Geophysical Journal International*, *163*(1), 1–9. doi:10.1111/j.1365-246X.2005.02714.x

Orlando, L. (2013). GPR to constrain ERT data inversion in cavity searching: Theoretical and practical applications in archeology. *Journal of Applied Geophysics*, *89*, 35–47. doi:10.1016/j.jappgeo.2012.11.006

Parker, B. L., Gillham, R. W., & Cherry, J. A. (1994). Diffusive Disappearance of Immiscible-Phase Organic Liquids in Fractured Geologic Media. *Ground Water*, *32*(5), 805–820.

Pehme, P. E., Parker, B. L., Cherry, J. a., Molson, J. W., & Greenhouse, J. P. (2013). Enhanced detection of hydraulically active fractures by temperature profiling in lined heated bedrock boreholes. *Journal of Hydrology*, *484*, 1–15. doi:10.1016/j.jhydrol.2012.12.048

Perri, M. T., Cassiani, G., Gervasio, I., & Deiana, R. (2012). A saline tracer test monitored via both surface and cross-borehole electrical resistivity tomography: Comparison of time-lapse results. *Journal of Applied Geophysics*, *79*, 6–16. doi:10.1016/j.jappgeo.2011.12.011

Revil, A., & Skold, M. (2011). Salinity dependence of spectral induced polarization in sands and sandstones. *Geophysical Journal International*, *187*(2), 813–824. doi:10.1111/j.1365-246X.2011.05181.x

Robert, T., Caterina, D., Deceuster, J., Kaufmann, O., & Nguyen, F. (2012). Case History A salt tracer test monitored with surface ERT to detect preferential flow and transport paths in fractured / karstified limestones, *77*(2).

Robinson, J., Johnson, T., & Slater, L. (2013). Evaluation of known-boundary and resistivity constraints for improving cross-borehole DC electrical resistivity imaging of discrete fractures. *Geophysics*, *78*(3), D115–D127.

Robinson, J. L., Slater, L. D., & Schäfer, K. V. R. (2012). Evidence for spatial variability in hydraulic redistribution within an oak–pine forest from resistivity imaging. *Journal of Hydrology*, *430-431*, 69–79. doi:10.1016/j.jhydrol.2012.02.002

Robinson, J., Slater, L., Johnson, T., & Binley, A. (2013). Strategies for characterization of fractured rock using cross-borehole electrical tomography. *The Leading Edge*, 784–790.

Rorabaugh, M. J. (1953). Graphical and theoretical analysis of step-drawdown test of artesian well. *Proceedings of the American Society of Civil Engineers*, *79*(separate no. 362).

Rücker, C., Günther, T., & Spitzer, K. (2006). Three-dimensional modelling and inversion of dc resistivity data incorporating topography - I. Modelling. *Geophysical Journal International*, *166*(2), 495–505. doi:10.1111/j.1365-246X.2006.03010.x

Sasaki, Y. (1994). 3-D resistivity inversion using the finite-element method. *Geophysics*, *59*(11), 1839–1848.

Shapiro, A. M. (2010). The challenge of interpreting environmental tracer concentrations in fractured rock and carbonate aquifers. *Hydrogeology Journal*, *19*(1), 9–12. doi:10.1007/s10040-010-0678-x

Si, H. (2006). TetGen: A Quality Tetrahedral Mesh Generator and Three-Dimensional Delaunay Triangulator. Weierstrass Institute for Applied Analysis and Stochastics (WIAS), Berlin, Germany.

Singha, K., Day-Lewis, F. D., & Lane, J. W. (2007). Geoelectrical Evidence of Bicontinuum Transport in Groundwater. *Geophysical Research Letters*, *34*, L12401. doi:10.1029/2007GL030019.)

Singhal, B. B. S., & Gupta, R. . (1999). *Applied hydrogeology of fractured rocks* (p. 400). Kluwer Academi Publishers.

Slater, L., Binley, a, Versteeg, R., Cassiani, G., Birken, R., & Sandberg, S. (2002). A 3D ERT study of solute transport in a large experimental tank. *Journal of Applied Geophysics*, *49*(4), 211–229. doi:10.1016/S0926-9851(02)00124-6

Slater, L., Binley, a. ., Daily, W., & Johnson, R. (2000). Cross-hole electrical imaging of a controlled saline tracer injection. *Journal of Applied Geophysics*, *44*(2-3), 85–102. doi:10.1016/S0926-9851(00)00002-1

Slater, L., & Binley, A. (2006). Synthetic and field-based electrical imaging of a zerovalent iron barrier: Implications for monitoring long-term barrier performance. *Geophysics*, *71*(5), B129–B137. doi:10.1190/1.2235931

Slater, L., Binley, A., & Brown, D. (1997). Electrical Imaging of Fractures Using Ground-Water Salinity Change. *Ground Water*, *35*(3), 437–442.

Slater, L. D., Binley, A., & Brown, D. (1997). Electrical Imaging of Fractures Using Ground-Water Salinity Change. *Ground Water*, *35*(3), 436–442.

Slater, L. D., Brown, D., & Binley, A. (1996). Determination of hydraulically conductive pathways in fractured limestone using cross-borehole electrical resistivity tomography. *European Journal of Environmental and Engineering Geophysics*, *1*, 35–52.

Sorenson, K. S. (2000). Biodegradation of TCE Improved with Lactate Injection in Deep , Fractured Rock Enhanced In Situ Bioremediation Demonstrated in Fractured Bedrock. *Ground Water Currents*, *EPA 542-N*-(38).

Stummer, P., Maurer, H., & Green, A. G. (2004). Experimental design: Electrical resistivity data sets that provide optimum subsurface information. *Geophysics*, *69*(1), 120–139. doi:10.1190/1.1649381

Sugimoto, Y. (1999). electrical crosshole imaging. *The Leading Edge*, (December), 1425–1428.

Tiedeman, C. R., Lacombe, P. J., & Goode, D. J. (2010). Multiple well-shutdown tests and site-scale flow simulation in fractured rocks. *Ground Water*, *48*(3), 401–15. doi:10.1111/j.1745-6584.2009.00651.x

Ulrich, C., & Slater, L. (2004). Induced polarization measurements on unsaturated, unconsolidated sands. *Geophysics*, *69*(3), 762–771. doi:10.1190/1.1759462

Wallin, E. L., Johnson, T. C., Greenwood, W. J., & Zachara, J. M. (2013). Imaging high stage river-water intrusion into a contaminated aquifer along a major river corridor using 2-D time-lapse surface electrical resistivity tomography, *49*, 1–16. doi:10.1002/wrcr.20119

Wilkinson, P. B., Chambers, J. E., Lelliott, M., Wealthall, G. P., & Ogilvy, R. D. (2008). Extreme sensitivity of crosshole electrical resistivity tomography measurements to geometric errors. *Geophysical Journal International*, *173*(1), 49–62. doi:10.1111/j.1365-246X.2008.03725.x

Wilkinson, P. B., Chambers, J. E., Meldrum, P. I., Ogilvy, R. D., & Caunt, S. (2006). Optimization of Array Configurations and Panel Combinations for the Detection and Imaging of Abandoned Mineshafts using 3D Cross-Hole Electrical Resistivity Tomography. *Journal of Environmental & Engineering Geophysics*, *11*(3), 213–221. doi:10.2113/JEEG11.3.213

Wilkinson, P. B., Loke, M. H., Meldrum, P. I., Chambers, J. E., Kuras, O., Gunn, D. a., & Ogilvy, R. D. (2012). Practical aspects of applied optimized survey design for electrical resistivity tomography. *Geophysical Journal International*, *189*(1), 428–440. doi:10.1111/j.1365-246X.2012.05372.x

Wilkinson, P. B., Meldrum, P. I., Chambers, J. E., Kuras, O., & Ogilvy, R. D. (2006a). Improved strategies for the automatic selection of optimized sets of electrical resistivity tomography measurement configurations. *Geophysical Journal International*, *167*(3), 1119–1126. doi:10.1111/j.1365-246X.2006.03196.x

Wilkinson, P. B., Meldrum, P. I., Chambers, J. E., Kuras, O., & Ogilvy, R. D. (2006b). Improved strategies for the automatic selection of optimized sets of electrical resistivity tomography measurement configurations. *Geophysical Journal International*, *167*(3), 1119–1126. doi:10.1111/j.1365-246X.2006.03196.x

Zhang, J. (1995). 3-D resistivity forward modeling and inversion using conjugate gradients. *Geophysics*, *60*(5), 1313. doi:10.1190/1.1443868

Vita

1993	New Jersey Institute of Technology, Bachelors of Science, Civil Engineering
1994	Johns Hopkins University, Masters of Science in Engineering, Environmental Engineering
1994-1997	Consulting Engineer – Site design and hydraulics
1998-2001	Senior systems specialist designing procurement web applications
2007-2009	Part-time graduate student, Rutgers University, New Jersey
2009-2010	GK-12 Teaching Fellow, Rutgers University, New Jersey
2011	Masters of Science in Environmental Geology
2011-2014	Graduate Research Assistant, Rutgers University, New Jersey
2012	Peer-reviewed article: Robinson, J.L., Slater, L., Schafer, K. (2012). Evidence for spatial variability in hydraulic redistribution within an oak–pine forest from resistivity imaging. J. Hydrol., doi:10.1016/j.jhydrol.2012.02.002
2013	Peer-reviewed article: Robinson, J., Johnson, T., & Slater, L. (2013). Evaluation of known-boundary and resistivity constraints for improving cross-borehole DC electrical resistivity imaging of discrete fractures. Geophysics, 78(3), D115–D127.
2015	Peer-reviewed article: Robinson, J., Johnson, T., & Slater, L. (2015). Challenges and Opportunities for Fractured Rock Imaging Using 3D Cross Borehole Electrical Resistivity. Geophysics, 80(2), 1–13.